Intracavity Optical Parametric Oscillators Based on Orientation-Patterned Gallium Arsenide

By

Daniel John Kane

A thesis presented in fulfilment of the requirements for the degree of Doctor of Philosophy.

Institute of Photonics, Department of Physics, University of Strathclyde

2016

Declaration of authenticity and author's rights

This thesis is the result of the author's original research. It has been composed by the author and has not been previously submitted for examination which has led to the award of a degree.

The copyright of this thesis belongs to the author under the terms of the United Kingdom Copyright Acts as qualified by University of Strathclyde Regulation 3.50.

Due acknowledgement must always be made of the use of any material contained in, or derived from, this thesis.

Signed:  Date: 13/05/2016

Abstract

Intracavity Optical Parametric Oscillators (ICOPOS) have proven themselves as low primary pump threshold sources of broadly tunable mid-infrared coherent light – making them excellent single sources for spectroscopy applications. Periodically-poled lithium niobate (PPLN) is the current leading technology in this field due to its maturation. However, PPLN is limited in its applications due to its transmission spectrum – eventually running out at < 5 μm. With the applications-rich fingerprint region (6 μm to 12 μm) of increasing technological import, new crystals are being explored which will open this part of the spectrum for exploitation. The novel crystal orientation-patterned gallium arsenide is one such technology. With a transmission window of 2 μm to 12 μm, it can access all of the chemical fingerprint region – however its cut-on wavelength of 2 μm precludes the use of established 1μm pumping technologies, requiring less mature 2 μm sources are used.

The operation of a Tm^{3+}:YAP pumped pulsed OPO based on orientation patterned gallium arsenide was demonstrated. For 15 W of incident diode pump power up to 120 mW of useful idler (650 mW of total downconverted power) could be extracted at a repetition rate of 200 kHz. This corresponded to a downconversion efficiency of 60 %. The OPO could be tuned over the range 2.9-3.5 μm (0.6 μm) in the signal and 4.6-5.8 μm (1.2 μm) in the idler for 54 nm of tuning in the pump for a 56 μm period crystal. For a crystal of QPM grating period of 60.5μm the OPO could be tuned over the range 5.9-6.8 μm (0.9 μm) in idler & 2.7-3 μm (0.3 μm) in signal for 50 nm of tuning in the pump.

A GaSb based semiconductor disk laser (SDL) was also examined as a potential pump source. Intracavity powers exceeding 200W were achieved with good beam quality, suggesting good potential as an ICOPO pump source. However, loss related issues precluded the operation of ICOPO devices in the laser system.

Acknowledgements

First and foremost, I would like to thank everyone that I worked with during my time at the IoP and Fraunhofer-CAP for their various contributions (professional or not) in undertaking this Ph.D., and without whom this would not have been possible.

I would like to thank Dr. David Burns and Dr. John-Mark Hopkins for initially taking me on as a Ph.D. student and for making the first year of my Ph.D. so enjoyable – especially J-M for being such a good friend and counsellor down all the rest of the years as well. I would also like to thank Dr. David Stothard for taking me on as a Ph.D. by proxy during my time at F-CAP, his guidance and help in the lab is what ultimately made the undertaking of the body of work in this thesis possible, as well as my future career, for which I will always be grateful for. My last professional acknowledgement extends to Prof. Alan Kemp for picking up the pieces after David left and helping me to complete my Ph.D. effectively and on time. His skills in organising and his determination to fulfil his duties to the maximum of his abilities has both been of great benefit and inspiration to myself and will always serve as an example to me.

I would like to thank everyone at strathy judo club, Elisabeth Fraczek and Miguel Leitao for reminding me that a Ph.D. is supposed to be fun sometimes as well. Special thanks goes to Rolf Birch, Paul Hill and especially Peter Schlosser for getting dragged into my madcap dream to climb Ben Nevis before I left Scotland and for making it such a laugh along the way, despite the pain involved.

I would also personally like to thank Ewan Bennet and Sean Reilly for all of the banter along the way, the vicious games of 5-a-side as well as their companionship (with JM) on the religious pilgrimages to the Mecca of fried poultry that is Chunky Chicken – Team Chunky for life!

Finally I would like to thank my closest friends and family for everything through all the years, for which I can't thank them enough, as well as someone who once asked me very politely if they could sit at the table across from me…..

Table of Contents

Chapter 1
Introduction

1.1 Introduction

With the advent of the laser in 1960 with Theodor Maiman's construction of the first ruby laser [1] applications driven research initially focussed on visible and near-infrared devices due to the ready availability of laser materials and detectors in this region, e.g. ruby, Ti:Sapphire and Nd:YAG lasers, even though the mid-IR waveband may have been superior for a number of applications. Ti:sapphire and Nd:YAG in particular are still ubiquitous in today's field of laser technology. With the development of detectors capable of operating further into the infrared region of the spectrum [2] applications driven development in the mid-IR waveband became more practical, leading to an increase in research activity in this area to satisfy demand for laser sources able to meet applications in the mid-IR - an important waveband for spectroscopy [3], medicine [4] and industrial process monitoring and security applications [5].

With the first demonstration of frequency conversion by the generation of second harmonic radiation by Franken et al in 1961 [6] and the later demonstration of parametric downconversion by Giordmaine and Miller in 1965 [7], it became possible to reach wavelengths which could not be obtained by conventional means from established laser sources. This expanded the boundaries for applications driven laser development in both the ultraviolet as well as in the infrared. While early theoretical work and experimentation was performed in the field in the 1970 by Smith and Parker [8], it wasn't until the pioneering work of Colville, Ebrahimzadeh and Dunn in 1997 [9] that practical intracavity optical parametric oscillators were demonstrated. This allowed for low primary pump threshold OPO devices which were efficient for practical applications where only 100's of milliwatts of power were required [10]. Devices of this kind shall be the focus of this thesis, whose goal is the generation of radiation far into the mid-IR

waveband through intracavity frequency conversion in the novel nonlinear material orientation-patterned gallium arsenide (OP-GaAs).

In this chapter the concepts behind and the applications in the mid-IR waveband which motivate and drive the work in this thesis shall be discussed. Competing technologies and methods of infrared coherent radiation generation are presented and briefly discussed along with nonlinear frequency conversion methods. The current state of the art in available mid-infrared nonlinear crystals shall also be presented.

1.2 The Mid-infrared Waveband and the Chemical Fingerprint region

While there is no single agreed definition of what the mid-infrared region of the spectrum is, for example the international organisation for standardization (ISO) defines the mid-infrared waveband as being electromagnetic radiation emitted between 3 μm and 50 μm (ISO 20473:2007), for the purposes of this work it shall be considered to be the region between 2 μm and 12 μm. This band covers the important chemical fingerprint region of the spectrum, which lies between 6 μm and 12 μm. This region is so called due to the large number of distinct absorption bands in the region, caused by the absorption of radiation by chemical bonds into vibrational and bending modes. These provide a distinct sets of markers which are unique for many molecules allowing for their identification by absorption spectroscopy. As an illustration, a selection of absorption line position data obtained from the HITRAN 2012 database [11] for a number of significant chemical species between 2 μm and 12 μm is shown in figure 1.1 This plot was generated by the spectralcalc software created by GATS Inc., whose basic functionality is freely available online [12]. It can be seen from figure 1.1 that for almost all of the molecules there are a large number of densely packed line positions in the 6 μm to 12 μm region.

Figure 1.1 The line position data for a number of gas species obtained from the HITRAN 2012 database and plotted by the spectralcalc software. It can be seen that a wide array of molecules have many lines within this spectral region.

However, for practical free-space detection and identification of species by absorption spectroscopy, it is important to know what the water absorption in the atmosphere is for this wavelength region. Strong water absorption in this region would render any attempt to detect individual absorption lines meaningless as they would be obscured by the absorption of the water molecules.

The line intensity for water at atmospheric pressure at sea level is given in figure 1.2. From the figure it is possible to see that there is strong absorption in the 2.5 μm to 3 μm region of the spectrum as well as between 6 μm to 7 μm. However, there are several 'atmospheric windows' where water absorption is negligible between 2 μm and 12 μm. The window between 8 μm to 12 μm is of particular importance as this also lies within the chemical fingerprint region.

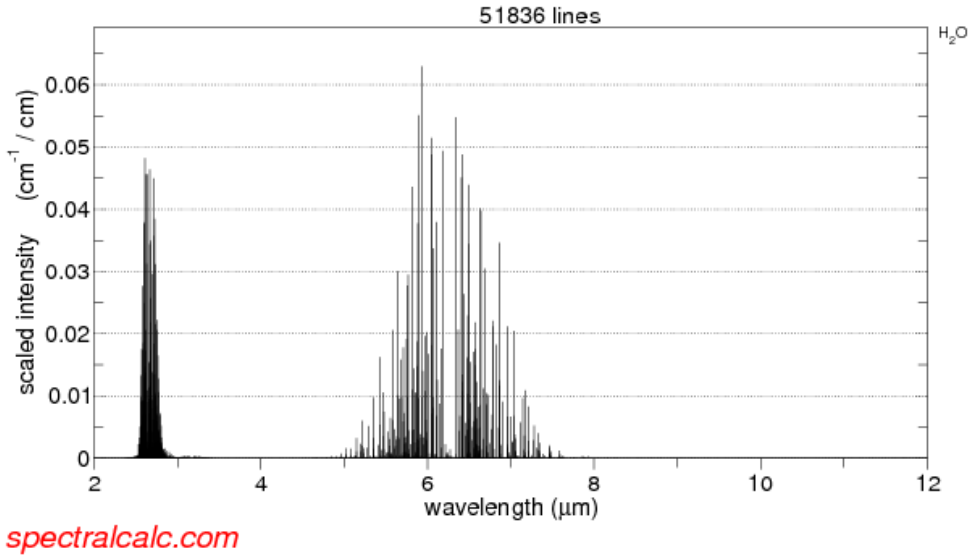

Figure 1.2 The line data intensity for water at atmospheric pressure at sea level between 2 μm and 12 μm obtained from the HITRAN 2012 database, plotted on a linear scale. There are two viable water windows between 3 μm and 5 μm and from 6 μm to 12 μm.

This makes this region of the spectrum ideal for the remote detection and identification of gas species in free-space, and as such research to construct spectroscopic devices which operate here is an important topic in laser engineering.

1.3 Mid-Infrared Laser Sources

With the large number of applications in the mid-IR waveband offered by the strong and unique absorption features of chemicals in this region, a number of laser sources have been developed to meet demand. In this section an overview of the competing technologies to the optical parametric oscillators discussed in this thesis shall be presented and their relative advantages and disadvantages

will be discussed. These include crystalline laser sources, fibre laser sources, semiconductor technologies and difference frequency generation techniques.

1.3.1 Crystalline Mid-Infrared Laser Sources

There exist a large number of crystalline laser sources capable of operating in the mid-IR region of the spectrum but they all fit in to three broad categories – transition metal^{2+} (TM^{2+}) ion doped lasers, colour centre lasers and rare-earth^{3+} doped lasers [13]. Each of these approaches has their own unique strengths and weaknesses which shall be discussed in the appropriate section, beginning with TM^{2+} doped lasers.

1.3.1.1 Transition Metal Doped Lasers

TM^{2+} ion lasers historically replaced dye jet lasers in the mid-IR region of the spectrum, offering improvements in both safety and performance. All TM^{2+} ions oscillate on the 3d-3d transitions in the mid-IR, which being the outermost electrons experience strong perturbations from the crystal field leading to strong broadening of their laser transitions. However they can be separated by which geometry of crystal site they occupy – either octahedral, like Ni^{2+} and Co^{2+} when doped into halides, or tetrahedral like Cr^{2+}, Fe^{2+}, Ni^{2+} and Co^{2+} doped into the chalcogenides. TM^{2+} ions in octahedral sites operate on parity forbidden transitions which lead to longer upper state lifetimes, leading to narrower linewidth emissions but lower oscillator strength, while those in tetrahedral sites tend to have shorter lifetimes, broader emisions and higher oscillator strength [13].

While the first tunable solid-state laser to ever be demonstrated was actually Ni^{2+} doped in MgF_2 [14], the need to cryogenically cool Ni^{2+} doped lasers to achieve efficient performance renders such laser sources unsuitable for many practical applications [13]. Co^{2+} based laser sources have fared a little better, due to the potential for room temperature operation, with Nd:$YALO_3$ pumped Co^{2+}:MgF_2

developing into practical, commercial laser systems, with a tuning range of 1750 nm to 2500 nm and pulse energies of up to 70 mJ at a 10 Hz repetition rate [15]. Fe^{2+} doped gain media also attracted some interest due to their deeper penetration into the mid-IR band, with continuous tuning being demonstrated between 3.77 μm to 5.05 μm. However their requirement to be pumped at wavelengths which are also quite far into the infrared, between 2.5 μm and 4.5 μm, and again aggressively cooled has hampered their development into practical, tunable mid-IR infrared sources [16].

Cr^{2+}-doped chalcogenide lasers, on the other hand, have attracted considerable research interest as tunable mid-IR lasers since their development in 1997 [17]. The excellent thermal and mechanical properties of the chalcogenides, with the exception of their high rate-of-change of refractive index with temperature, make them an excellent host material for laser ions [13, 17]. The most common chalcogenides used as hosts for chromium are Cr^{2+}:ZnS, Cr^{2+}:ZnSe, Cr^{2+}:ZnS_xSe_{1-x}, and Cr^{2+}:CdSe. Capable of emitting between 1880 nm and 3100 nm, a range which covers a broad section of the mid-IR, the broad emission bandwidth of these lasers has allowed them to be modelocked with pulse widths of less than 100fs [18-20]. The various crystals are pumped between 1.5 μm and 1.9 μm, where many established diode and solid-state laser pump sources can be found. Chromium-doped chalcogenide lasers have been rendered even more attractive for commercial applications with the establishment of mass producible semiconductor disk lasers (SDLs) in the 1.9 μm region, with successful demonstrations of SDL pumped Cr^{2+}:ZnSe which operated at an output power of 1.8 W and a slope efficiency of ~50 % [21, 22].

1.3.1.2 Colour Centre Lasers

Colour centre lasers provide an interesting alternative route towards producing laser action in the mid-IR from crystalline host materials. Colour centres (also called F-centres) all essentially consist of an electron trapped by defects in a dielectric crystal lattice structure, as shown in figure 1.3. While the basic F-centre is itself not capable of laser oscillation; more complex colour centres, such as

those consisting of an electron trapped by two anion vacancies, do oscillate allowing for laser operation. Colour centres have several properties which make them attractive for laser devices – they are often broadly tunable allowing for a large wavelength operating range from a single device, they have large emission cross sections and a very short upper-state lifetime which is excellent for amplitude stable, continuous wave operation [13, 23]. Colour centre lasers have been demonstrated which show tunability across the entire range from 0.9 μm all the way out to 5 μm [23-25]. However, colour centre lasers are yet to show promise for practical laser devices in the mid-infrared due to the need to cryogenically cool these systems with liquid nitrogen, which is not a viable method for out-of-the-lab applications [24].

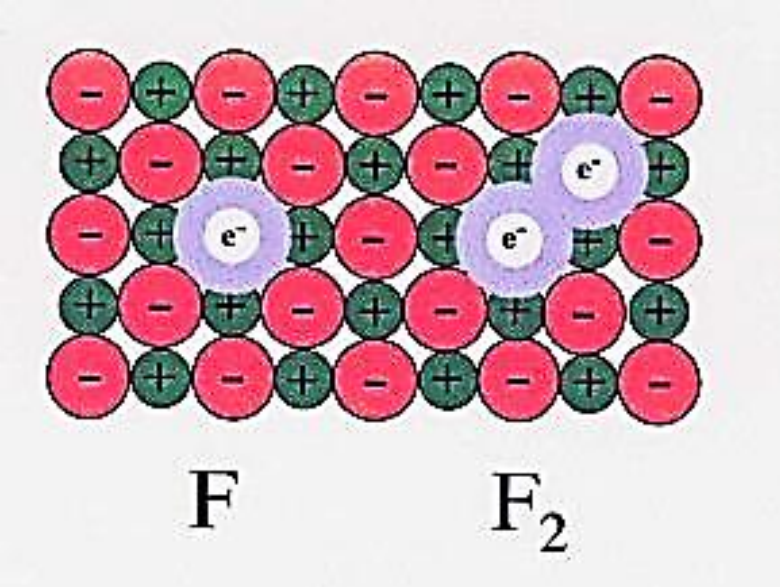

Figure 1.3 A diagram of various colour centres in a crystal lattice. In this diagram an F-centre, which consists of a single anion vacancy is shown, alongside an F_2 centre, which consists of two adjacent anion vacancies.

1.3.1.3 Rare-Earth Doped Lasers

Rare-earth ions make an excellent choice for use in lasers due to their ideal properties, indeed the most ubiquitous laser ion in the field of laser engineering, neodymium, is a 'rare-earth' ion. As lasing occurs in the 4f shell of the ion - which is internal to the ions electronic structure and therefore shielded from the effects of the crystal field by screening from the outer electrons - laser lines in these

materials are not influenced so strongly by their host lattice. While rare-earth gain media operate on a broad number of wavelengths, there are only two which are important to consider when it comes to tunable mid-infrared laser materials – thulium and holmium [26]. Gain media based on these materials shall be discussed further in this section, however it should also be noted that a more detailed and elaborate discussion on thulium is given in chapter 3, particularly with regards to its suitability as a pump laser for orientation-patterned gallium arsenide.

Thulium is perhaps the most well established mid-infrared solid-state laser material, with the first demonstration of a thulium device in 1973 by Weber et al. [27] and the later development of commercial laser diodes at appropriate pump wavelengths (~795 nm) allowing for efficient, practical devices to be realised [12, 28-31]. There are three commonly used Tm-doped laser crystals with emission in the mid-IR – Tm:YAP, Tm:YLF and Tm:YAG. Tm:YAG, however, emits a very narrow range of wavelengths centred on 2.01 μm, and so will not be considered here as alternative source of tunable mid-IR radiation [31]. Tm:YLF, with a tuning range of ~1.90 μm to 1.95 μm has proven itself to be an excellent, practical high-power laser source in this region, with output powers of up to 200 W recorded in literature [32-34]. Tm:YAP, while not showing the same extreme high-power performance as Tm:YLF, has shown itself to be perfectly viable as a gain medium for a mid-IR, tunable laser source [12, 28-30]. The "two-for-one" quantum efficiency provided by energy transfer up-conversion caused by cross-relaxation in thulium gain media, matched with the ready availability of efficient high-power diodes at the pump wavelength for Tm:YAP (793 nm) makes them practical as high-efficiency sources [12, 29]. With a tuning range in the region of 1.89 μm to 2.01 μm and output power of up to 72W recorded [28, 35-38], Tm:YAP provides a good platform for mid-IR source development.

Tm:Ho:YAG has also shown some promise as a gain material operating in the mid-IR waveband, but it has some significant drawbacks which lower its desirability as a tunable mid-IR laser material. With the lack of suitably mature pump laser technology at the absorption wavelength of Ho doped gain media (~1.9 μm), Ho

crystals have to be co-doped with Tm crystals to enable widely available high-power laser diodes to be used to pump them [12, 27, 39, 40]; however, research towards direct diode pumping has been undertaken in recent years, but this is far from being a commercially mature technology [41]. The tendency of Ho doped gain materials to only oscillate at a fixed wavelength (~2.1 μm) ultimately precludes their use as tunable mid-IR sources [12, 27, 40, 42].

1.3.2 Mid-Infrared Fibre Laser Sources

With the development of double clad fibre, alongside technological advances in fibre fabrication and high-power laser diodes, the performance of diode-pumped fibre lasers has improved to levels which are viable for practical applications [43]. For infrared laser development, there are several suitable ions and well as glass hosts which can be successfully drawn into fibres. A list of suitable fibre material is shown in table 1.1.

Fibre Material	Infrared Transparency (μm)
Silica [44]	< 2.5
ZBLAN [45]	< 6.0
GLS [46]	< 8.0

Table 1.1 A number of popular fibre materials with infrared transmission, showing these alongside their infrared transparency range.

Silicate glasses are perhaps the most ubiquitous and well known material used in fibre lasers and optics. However, their relatively high maximum phonon energy of 1100 cm^{-1} limits their transmission to wavelengths no longer than 2.5 μm. ZBLAN, a composite glass of several heavy metal fluorides (zirconium, barium, lanthanum, aluminium and sodium) is another potential candidate for hosting mid-IR fibre laser ions, with a maximum phonon energy of 550 cm^{-1} wavelengths of up to 6 μm will readily propagate in ZBLAN fibre. It should be noted however that multiphonon emission becomes an issue in ZBLAN at wavelengths beyond 3 μm [45]. Gallium lanthanum sulphide (GLS) is the final material on our list of mid infrared fibre hosts. Having a maximum phonon energy of 300-450 cm^{-1}, wavelengths of up to 8 μm can be transmitted through a GLS fibre. The high

solubility of rare-earth ions in GLS adds to the materials attractiveness for use as a host; however, this is offset by the somewhat low thermal conductivity of this material, yet it shows good promise for future mid-IR laser development [46, 47].

At the time of writing there are several established ion and fibre host combinations which operate in the mid-infrared region of the spectrum and are listed in table 1.2.

Ion	Host	λ_{pump}(nm)	λ_{laser}(μm)	Output Power	Reference
Tm^{3+}	Silica	787	1.9 (1.86-2.09)	14W	[48]
Ho^{3+}	ZBLAN	805	2.1	8.8W	[49]
Tm^{3+}	ZBLAN	790	2.3	22mW	[50]
Er^{3+}	ZBLAN	792	2.7	1.7W	[51]
Ho^{3+}	ZBLAN	1150	2.9 (~80 nm tuning)	1.3W	[52]
Ho^{3+}	ZBLAN	532	3.22 (3.12-3.14)	11mW	[53]
Er^{3+}	ZBLAN	653	3.45	8mW	[54]
Ho^{3+}	ZBLAN	890	3.95 (3.9-3.95)	11mW	[55]

Table 1.2 A table listing currently established mid-infrared fibre lasers by wavelength of operation. The sources listed here cover the range between 1.9 μm and 3.95 μm.

From table 1.2 it can be seen that fibre lasers have been able to penetrate deep into the mid-IR in terms of wavelength, although high-power, multi-watt level, operation has only been reported at wavelengths of less than 3 μm so far. The largest handicap for fibre lasers in the mid-infrared, in terms of practicality as spectroscopy sources, is the lack of tunable lasers beyond 2.1 μm range, as the majority of the rare-earth ions which have been implemented thus far give narrow bandwidth emission.

Future work in fibre lasers however, does show good scope for deep mid-IR operation up to 5 μm [56-58]. Glasses such as GLS, which have very low phonon

energies, are suitable hosts for dopants with such long wavelength transitions. Issues involving the toxicity of the starting materials as well as difficulties in making ultra-low loss fibre currently impede progress with the practical mass-manufacture of this material. However, in future these problems may be overcome, leading to further practical fibre sources in the mid-IR [43].

1.3.3 Semiconductor Mid-Infrared Laser Sources

Another avenue of approach to the direct generation of mid-IR radiation is by means of semiconductor-based technology. With their mass producability and their capability to be electrically powered, semiconductor lasers lend themselves well to practical applications. When it comes to the production of high-power, tunable mid-IR laser radiation, there are three semiconductor technologies which are of particular note – interband edge emitting diode lasers, semiconductor disk lasers (SDLs) and quantum cascade lasers (QCLs). These technologies differ in their fundamental approach and have distinct advantages and disadvantages, which shall be dealt with independently in the following sections, beginning with interband diode lasers.

1.3.3.1 Interband Heterojunction Diode Lasers

Interband semiconductor edge emitting diode lasers are a broadly ubiquitous laser platform used in some capacity (often as a pump source) in many laser systems. Depending on the interband alignment, these lasers are classified into two broad types – type I lasers where the upper laser and lower laser levels are found in the conduction and valence bands of one layer (a direct transition) or type II lasers where the upper laser level is found in the conduction band of one layer and the lower laser level is to be found in the valence band of an adjacent layer (an indirect transition). A diagram of these band structures is shown in figure 1.4.

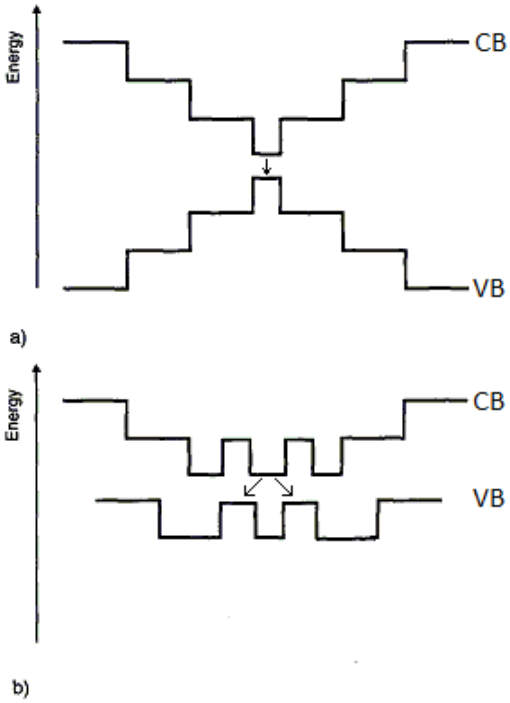

Figure 1.4 The band structures of type I and type II semiconductor diodes. Figure 1.4 a) shows a type I material where the lower and upper laser level are in the same layer while a type II material, where the upper and lower laser levels are in adjacent layers is shown in figure 1.4 b)

In type I materials, the transition which determines the energy, and therefore the wavelength, of the laser photons is set by the band gap of the material. Such direct transition is favoured and therefore can be considered to be more efficient in comparison to indirect transitions where other factors don't strongly effect efficiency. With type II materials the transition occurs between two different layers and is as such an indirect transition, which negatively impacts efficiency. However, by transitioning between two separate layers, the wavelength of the emitted photon can be engineered to some degree by selecting different materials as it is the combination of the two which determines the output wavelength. The electron and hole confinement is also separated, leading to greater confinement and therefore an increased efficiency compared to laser devices where confinement is traditionally poor – such as in type I lasers operating at longer wavelengths. From current type I and type II edge emitting diode lasers, devices operating between 1.9 μm to 4.0 μm [59-65] have been realised using antimonide based semiconductor materials, while lasers operating from 3 μm all the way out to 30 μm [66, 67] have been demonstrated for lead-salt based devices. While

these devices offer all the advantages that diode lasers are well known for, such as ease of mass manufacture, the ability to be electrically pumped and high output powers for room temperature operation – they also suffer from all of the well-known drawbacks of diode lasers, such as poor mode quality of the emitted laser beam along with limitations on longer wavelength (post 5 μm) emission, such as losses due to Auger recombination at room temperature which is the main loss mechanism in such diode lasers.

1.3.3.2 Semiconductor Disk Lasers

Semiconductor disk lasers, also known as vertical external-cavity surface-emitting lasers (VECSELs) are a class of laser which differentiates itself from traditional semiconductor lasers by having its emission perpendicular to the plane of the device, allowing for larger emission areas and therefore, when optically-pumped at least, aiding with good beam quality and thermal dissipation in the chip [68]. The implementation of an external cavity also allows for the insertion of intracavity components to control the properties of the spatial and longitudinal modes emitted from the laser as well as allowing access to the high intracavity field. While the first SDL was demonstrated in 1966, it was not until the late 1990's that practical laser devices were realised and the full potential of the technology began to be explored [68-70]. With SDLs being treated in further detail in chapter 2, especially with regards to their operating principles, only achievements in mid-infrared semiconductor lasers shall be discussed here.

Mid-infrared SDLs based on the GaSb material systems have been demonstrated operating between 1.9 μm and 2.8 μm in recent years [71-76] by groups in both Freiburg and Tampere, with a record output power for a cw-SDL of 20 W being demonstrated by the Fraunhofer IAF in Freiburg [77]. The differential efficiency within GaSb devices is the current limiting factor in further improving the output power of such devices and can be attributed to the lower than typical internal efficiency as well as internal losses within such devices – which is similar to edge emitting analogues of the same devices [77].

1.3.3.3 Quantum Cascade Lasers

A second important semiconductor based approach to tunable laser emission is the use of so called quantum cascade lasers (QCLs). First developed by Faist et al. in 1994 [78]. Quantum cascade lasers are highly structured, epitaxially grown semiconductor devices consisting of many thin (~nm) layers. These lasers, rather than being based on emission from electron-hole pair recombination between the conduction and valence bands in the semiconductor medium, rely instead upon the emission of radiation by an electron as it transits from one subband to another in the conduction band of the highly engineered semiconductor structure. A simplified diagram of a section of the active region structure of a QCL is shown in figure 1.5.

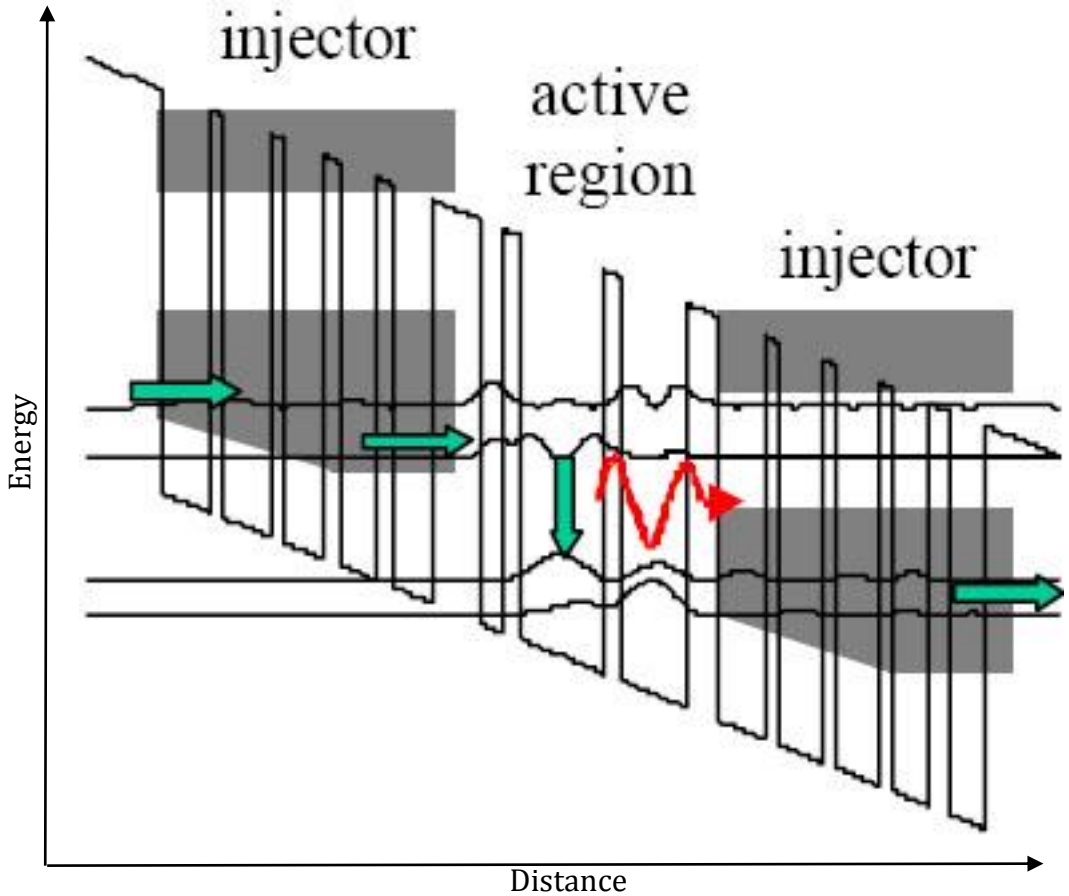

Figure 1.5 A simplified diagram of the conduction band structure of a QCL showing several injector regions and a single active region (band energy vs. propagation distance). This basic structure is repeated a number of times in the QCL allowing a single carrier to create multiple photons.

When an electric field is applied to a quantum cascade laser, electrons can transition across the injector regions into the active regions by means of quantum tunnelling. The electrons arrive in the upper state of the active regions, whereupon they move from the upper state to a lower band, emitting radiation. They can then tunnel through the next injector region into the following active region, where they once again arrive in the upper state. This process repeats as the electron cascades through the device creating a photon at each transition (hence the name, quantum cascade laser) thereby building up gain in the optical field. The key advantage of QCLs is that the operational wavelength of the laser depends only upon the structure of the device, rather than the band gap or transition within the constituent materials. By engineering these structures, wavelengths in the range between 3 μm to 150 μm have been successfully demonstrated [79-82].

While quantum cascade lasers demonstrate an impressive range of emission wavelengths as well as high efficiency, they have several drawbacks which hinder there adoption as a widespread technology of choice for mid-infrared laser emission. The typical powers emitted by QCL devices in the mid-infrared tends to be limited to the 10's to 100's of mW at best and often requires cryogenic cooling or operation in the pulsed regime, both of which preclude their use as a practical laser source for certain real-world applications.

The complex growth required to realise the precise multilayer structures which quantum cascade lasers call for is another challenge which must be overcome in implementing QCL devices in a practical context. The structures require many thin semiconductor layers to be grown epitaxially, and as such the accuracy required makes repeatability of the growth very difficult and very precise calibration of the growth is required. This all contributes to the relatively high (£10k+) cost of individual sources despite the eventual economy of scale usually associated with semiconductor wafer fabrication.

1.4 Nonlinear Frequency Conversion in the Mid-Infrared

After the first demonstration of frequency conversion by the generation of second harmonic radiation by Franken et al in 1961 [6], demonstrating the feasibility of the preceding theoretical work in this area, the field of non-linear frequency conversion opened up and much experimental work has been undertaken since. There are many different methods in which the frequency of optical radiation can be altered or shifted, but the most common can be split into two broad categories – three-wave mixing processes which are mediated by the second order nonlinearity and four-wave mixing processes which are mediated by the third order nonlinearity. Three-wave mixing processes include second harmonic generation, sum-frequency generation, difference-frequency generation and optical parametric oscillation. Four-wave mixing processes include third harmonic generation, four-wave mixing through various combinations of sum and difference-frequency generation and stimulated Raman scattering. In the interest of tunable mid-infrared source development there are two processes in particular which shall be focussed upon – optical parametric oscillation and difference-frequency generation. With their ability to take a source of laser light and convert it to arbitrarily long wavelengths, limited only by the phase matching and transparency of the nonlinear medium, these techniques provide the perfect platform to convert existing, high-performance, laser sources and transfer their output into the mid-infrared. In the following subsections a more detailed description of the parametric down conversion process and difference-frequency generation shall be given, although a more formalised discussion of the intricacies of optical parametric oscillation is provided in chapter 2.

With their capability to take established laser sources and convert their output to longer wavelengths, optical parametric oscillators (OPOs) appear to be an ideal way to produce infrared, and indeed possibly even longer, wavelength laser systems. First demonstrated in 1965 by Giordmaine and Miller [7], optical parametric oscillator sources are now commonly available as commercial, tunable laser sources. With their broad tunability and single pump path

compared to difference frequency techniques, OPO devices seem to be perfect for the task of frequency conversion. However, these systems also exhibit several drawbacks, which detract from their initially attractive characteristics for long wavelength source development. High pump power thresholds tend to hinder OPO efficiency (optimal efficiency for an OPO occurs at ~2.5x threshold, see chapter 2 and [10, 83, 84]) or preclude operation outright, while their sometimes poor efficiency away from optimal conditions as well as the additional complication of appending an OPO cavity to another laser system can render them somewhat impractical for many applications.

In the parametric downconversion process, a photon of energy $\hbar\omega_1$ is split into two photons of energy $\hbar\omega_2$ and $\hbar\omega_3$ in a nonlinear dielectric crystal where, from conservation of energy, $\hbar\omega_1 = \hbar\omega_2 + \hbar\omega_3$, as such the frequency of the generated signal and idler photons must sum to the frequency of the initial pump photon, as shown in figure 1.6.

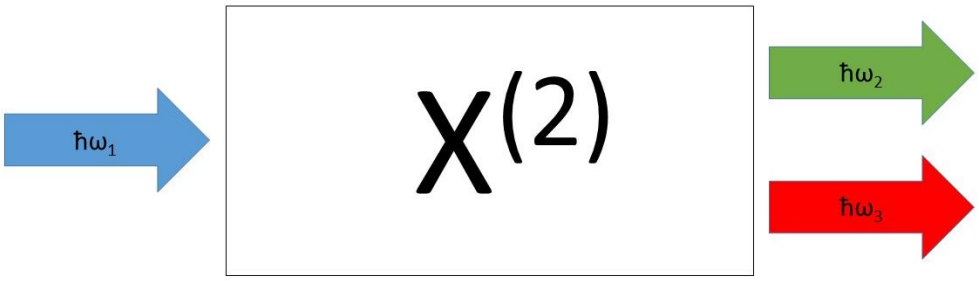

Figure 1.6 A simplified diagram of the parametric downconversion process. A single photon of energy $\hbar\omega_1$ is downconverted into two photons of energy $\hbar\omega_2$ and $\hbar\omega_3$ whose energy is determined by conservation of momentum.

Conservation of momentum is also key to defining the output from an optical parametric oscillator, with $\hbar k_1 = \hbar k_2 + \hbar k_3$, and as such the wavevector of the pump photon must also be equal to the sum of the wavevectors of the signal and idler photons. For the second condition to hold true, the generated signal and idler waves must remain in phase with the pump – a condition known as phase matching. Under optimal phase matching conditions the difference between the wavevectors $\Delta k = 0$, while the parametric gain varies as a sinc^2 function whose

argument is proportional to Δk. This provides wavelength selective gain in a parametric device. This, combined with the otherwise arbitrary parameters in the system, allows for a single-frequency, tunable source to be constructed from an OPO. There are two phase matching techniques which are implemented in optical parametric oscillators to ensure optimum frequency conversion – birefringent phase matching and quasi-phase matching. In birefringent phase matching, a birefringent crystal is used at a particular angle to the propagating beams to keep the phase velocity of the pump, signal and idler matched by utilising the different refractive indices of the various crystal axes. In quasi-phase matched media, the direction of the nonlinear coefficient is periodically reversed to keep the generated signal and idler waves in phase. For a more detailed discussion on phase matching, and optical parametric oscillators in general, see chapter 2. A more in depth discussion on mid-IR OPO crystals shall also be given in a later section.

Another means by which long wavelength generation can be achieved through nonlinear optical processes is via difference frequency generation. After the first demonstration of frequency mixing in 1961 by Bass et al. [85] difference frequency generation became a viable way of producing longer wavelength laser radiation. While similar to parametric downconversion in its adherence to conservation of energy and momentum, the equations are balanced subtly differently. In a difference frequency generator, pump and signal photons are launched into the nonlinear medium and an idler photon is produced whose energy is equal to the difference between the pump and the signal, such that, $\hbar\omega_1 - \hbar\omega_2 = \hbar\omega_3$, as shown in figure 1.7.

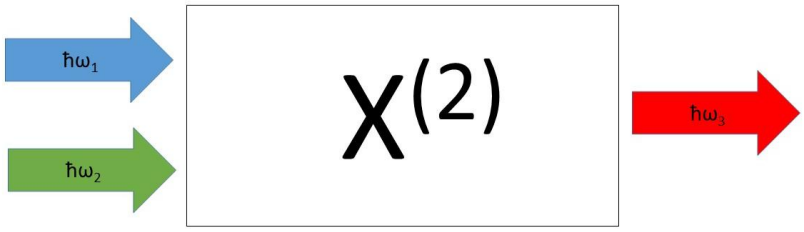

Figure 1.7 A simplified diagram of the difference frequency process. Two photons of energy ħω1 and ħω2 interact to produce a third photon of ħω3 whose energy is determined by conservation of energy.

Phase matching is therefore also critical in the difference frequency generation process, with practical gain only being achieved when the pump, signal and idler are phasematched with each other. Difference frequency conversion has the advantage of being a thresholdless process, removing the reaching of a minimum pump power as a barrier to operation. However, if one is seeking a broadly tunable DFG device, the need for broadly tunable pump laser sources renders these systems complex and expensive.

Difference frequency systems have demonstrated an excellent range of operating wavelengths and have shown deep penetration into the infrared with wavelengths as long as 18 μm being reported in the mid-IR as well as THz operation [86, 87]. A table summarising noteworthy DFG systems operating in the mid-IR is shown in table 1.3.

Pump Laser	Signal Laser	Nonlinear Material	λ_p(μm)	λ_s(μm)	λ_{DFG}(μm)	Ref.
Ti:Sapphire	Ti:Sapphire	KTP	0.69-0.75	0.91-1.05	2.3-1.8	[88]
OPA	OPA	$GaAsS_2$	1.1-1.6	1.6-2.93	2.4-12	[89]
Ti:Sapphire	OPG/OPA	CaF_2 & BaF_2	0.81	1.2-1.5	2.5-7.6	[90]
ECDL	HeNe	$Ti:LiNbO_3$	1.5-1.58	3.39	2.68-2.95	[91]
Ti:Sapphire	Nd:YAG	KTP	0.77-0.82	1.06	3.0-3.6	[92]
Nd:YAG	OPO	RTA	1.06	1.43-1.6	3.2-4.2	[93]
OPO	OPO	$GaAsSe_2$	1.7-2.1	2.26-2.84	5.0-18.0	[86]
DL	DL	$AgGaS_2$	0.766-0.786	0.83-0.868	6.8-12.5	[94]
ZGP OPG	ZGP OPG	$CdGeAs_2$	4-5	6.5-9.5	7-20	[95]

Table 1.4 A selection of mid-IR generating DFG devices. The devices in this table span a wide range of wavelengths from 2.3 μm to 20 μm.

In the next section orientation-patterned gallium arsenide (OP-GaAs) shall be discussed, along with its competitor nonlinear crystals in the infrared.

1.5 Orientation-Patterned Gallium Arsenide

With the multitude of applications in the mid-IR which can be met with nonlinear frequency conversion, the desire to develop semiconductor nonlinear materials, with their broad transmissions spectra in the infra-red, led to a push for technological development in this area. While a number of materials have been developed in this area, such as CdSiP and ZGP, one particularly stand out performer is orientation-patterned gallium arsenide. While the large nonlinear coefficient of GaAs has been known of since the 1960's [96], the crystal's isotropic nature prevented access to its nonlinearities by traditional means. The introduction of quasi-phase-matching techniques delivered a means by which the nonlinearities of isotropic crystals could be accessed; however, this still provided no succour for those wishing to harness the large nonlinearity of GaAs, as it lacked a dipole moment which could be exploited by known electrical poling techniques like those used with PPLN. It was not until 2006 [97], with the maturation of hydroxide-phase vapour epitaxy techniques for growing inverted layers of GaAs, that quasi-phase matched samples of suitable quality could be grown in a reasonable time-frame, enabling research in earnest on this material.

In this section an overview of OP-GaAs, including its growth and material properties shall be given alongside a brief discussion of alternative materials.

1.5.1 Alternative Materials to OP-GaAs

While OP-GaAs has displayed great potential as a nonlinear medium for generating mid-IR radiation, there are other materials, which for various reasons, are also suitable material choices for mid-IR generation. Suitable materials for efficient mid-infrared frequency conversion include zinc germanium phosphide (ZGP), cadmium silicon phosphate (CdSiP) and orientation-patterned gallium phosphide (OP-GaP). These materials all have their own innate advantages and drawbacks which shall be discussed in this section.

The first material to arise which filled the void in mid-infrared nonlinear device development was zinc germanium phosphide. The transmission range of ZGP lies between 2 μm to 8 μm, and as such ZGP covers most of the mid-IR and some of the chemical fingerprint region, however it does not cover all of the desired spectral range and requires a 2 μm pump source [98]. It should also be noted that ZGP has some absorption at the pump wavelength, which is dependent on material quality, with the highest damage threshold being reported as 2 J/cm^2 [98]. With a nonlinear coefficient of 75 pm/V, this gives ZGP a figure of merit (FOM = d_{eff}^2/n^3, see chapter 2) of roughly 181 [99]. With a natural birefringence, ZGP does not require quasi-phase matching to achieve efficient down-conversion.

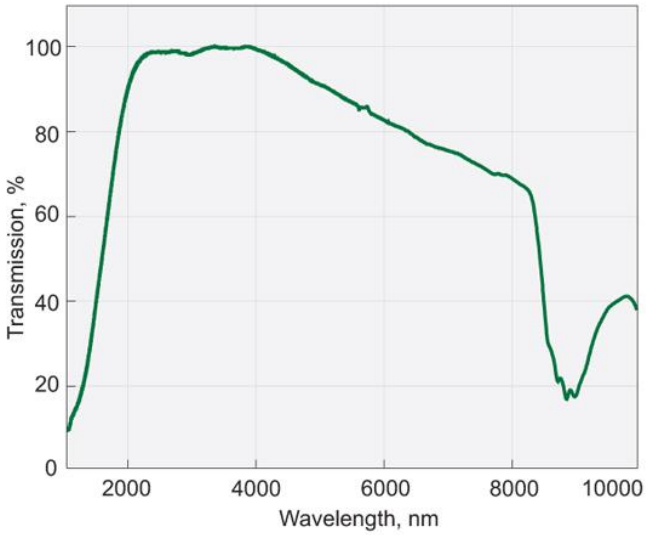

Figure 1.8 The transmission spectrum of ZGP. Courtesy of Eksma optics [100]. ZGP is shown to have a transmission range from 0.5 μm to 9 μm.

Another suitable material for mid-IR development is cadmium silicon phosphate (CdSiP). This material has a transmission range from 0.5 μm to 9 μm [101]. The near-infrared transparency of CdSiP allows for the use of more well established pump lasers based on neodymium but at a maximum wavelength of 9 μm, still does not cover the full chemical fingerprint region. CdSiP is inhibited by its relatively low damage threshold, with blackening of the crystal beginning at 0.1 J/cm^2 [102]. However, a high nonlinear coefficient of 84.5 pm/V gives CdSiP a good FOM of ~264 [101]. Also birefringent phase-matching techniques can be used with CdSiP to achieve efficient downconversion.

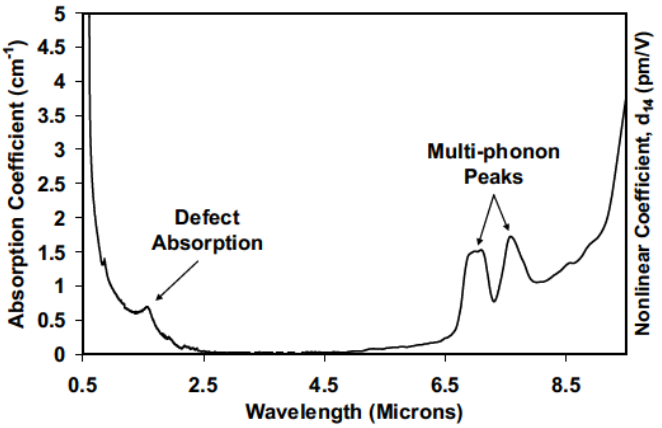

Figure 1.9 The absorption coefficient of $CdSiP_2$ between 0.5 µm and 9 µm, showing high transmission in this range. Courtesy of [103].

Finally, the recent development of application quality orientation-patterned gallium phosphide (OP-GaP) has added a new, promising material to the mid-infrared source developer's options. Possessing a transmission range from 0.6 µm to 11 µm [104], this material combines both ease of pumping with a broad transmission range, covering most of the mid-IR and chemical fingerprint region. The material is also quite resistant to being damaged optically, with a damage threshold of up to 1.5 J/cm^{-2} being reported. While it has a lower nonlinear coefficient than the other materials presented here, OP-GaP still has a good nonlinear coefficient of 45 pm/V and a viable FOM of 68 [104, 105]. The materials isotropic structure has meant that advancements in semiconductor growth techniques were required before quasi-phase matched crystals could be produced to a suitable quality.

Material	Transmission Range (µm)	Nonlinear coefficient (pm/V)	Figure Of Merit	Damage Threshold (J/cm^2)	Birefringent
ZGP	2-8	75	181	2	Yes
CdSiP	0.5-9	84	264	0.1	Yes
OP-GaP	0.6-11	45	68	1.5	No
OP-GaAs	2-12	94	225	2	No

Table 1.5 A summary of the key properties of nonlinear crystals with mid-infrared transmission. From the above data, it can be seen that Op-GaAs has the best mixture of properties for mid-IR frequency conversion.

1.5.2 Growth of OP-GaAs

Due to the isotropic nature of the linear refractive index of GaAs, the second order nonlinearity of OP-GaAs cannot be accessed by conventional means. This requires the use of quasi-phase matching to achieve efficient downconversion in OP-GaAs. It should be noted here that the second order nonlinearity can be utilised as the nonlinear refractive index is non-isotropic. Unlike its more ubiquitous counterpart periodically-poled lithium niobate, the structures needed for quasi-phase matching cannot be created by ferro-electric poling, and thus must be manufactured by other means. There exist three techniques which can achieve such structuring of GaAs - diffusion bonded GaAs (DB-GaAs), optically-contacted GaAs (OC-GaAs) and orientation patterned GaAs (OP-GaAs) [106]. DB-GaAs structures are the simplest structures to engineer, created by bringing GaAs plates together under high temperature and pressure until diffusion occurs, but it also exhibit the highest losses of those which are available. OC-GaAs structures, created by bonding together GaAs plates via capillary bonding which makes it trickier to engineer, offers improved performance over diffusion bonding. However orientation patterned growth of OP-GaAs provides the highest quality material with the lowest losses in the region of $<0.005\ cm^{-1}$ [106].

The production of OP-GaAs of suitable thickness is a considerably more intensive and technically challenging process than the two processes described above. In particular, the capital intensive nature of acquiring and maintaining the hydroxide-phase vapour epitaxy equipment used in the process has been the major obstacle in OP-GaAs development, with only AFRL, Thales and more recently BAE Systems having developed this capability [107]. To grow practicably thick OP-GaAs, a four stage growth process must be undertaken, which is shown in figure 1.10. The rest of this paragraph gives only a brief overview of the growth process, for a more detailed explanation, the paper of Eyres et al [108] gives an excellent account of performing OP-GaAs growth. First GaAs/Ge/GaAs heteroepitaxy is used to create an inverted layer, where the lattice is “flipped” such that the sign of the nonlinearity is reversed, on a GaAs substrate (1.10(a)),

the wafer is then patterned to create an orientation template (1.10(b)). Molecular beam epitaxy is then performed to grow a seed layer for the OP-GaAs crystal (1.10(c)) before the final, thick growth is performed by hydroxide-phase vapour epitaxy (1.10(d)) [97, 107-109].

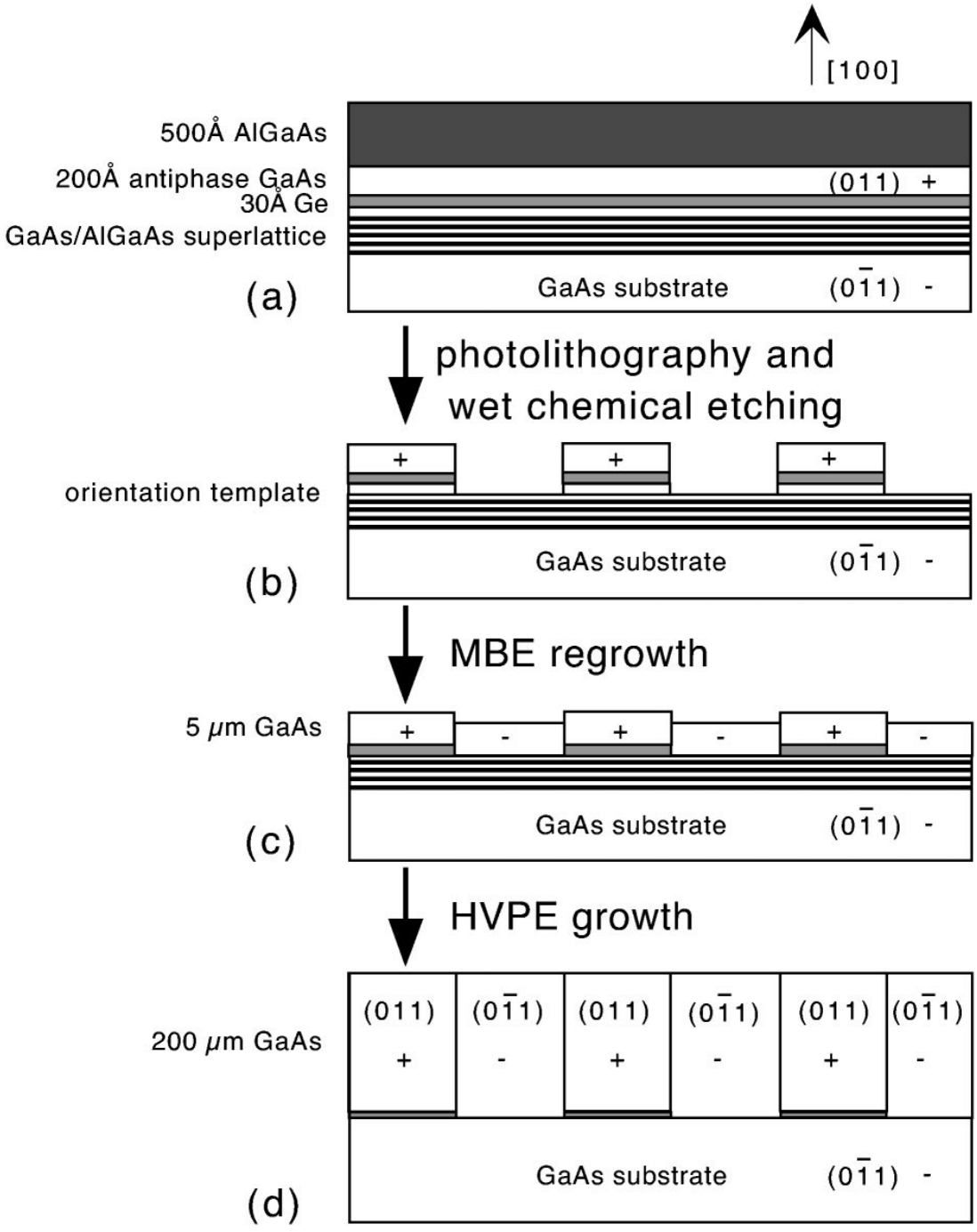

Figure 1.10 The fabrication process for thick orientation-patterned gallium arsenide. The ± signs indicate the domain nonlinear susceptibility. Reproduced from "Eyres, L., et al., All-epitaxial Fabrication of Thick, Orientation-patterned GaAs Films for Nonlinear Optical Frequency Conversion. Applied Physics Letters, 2001. 79(7): p. 904-906", with the permission of AIP Publishing.[108].

1.5.3 Material Properties of OP-GaAs

When it comes to evaluating the suitability of a crystal for nonlinear frequency conversion purposes, there are four key properties of the material which must be taken into account – the transmission range of the crystal must include the pump, signal and idler waves to minimise unnecessary losses, the size of the nonlinear coefficient and the figure of merit (the ratio of the nonlinear coefficient squared to the refractive index of the medium cubed) which represents the efficiency at which pump can be converted to signal and idler and finally the damage threshold, which sets a limit on the fluence which can be passed through the crystal without damaging it and thus caps maximum input and output energies. When it comes to all of these parameters, OP-GaAs fares comparatively well to its peers (see table 1.5). The broad transparency range of 2 μm to 12 μm [110-113] covers a vast swathe of the mid-infrared region of the spectrum (indeed, more than its counterparts) including the entirety of the chemical fingerprint region. However the cut-on wavelength of 2 μm requires that less mature laser technologies to be used as pump sources.

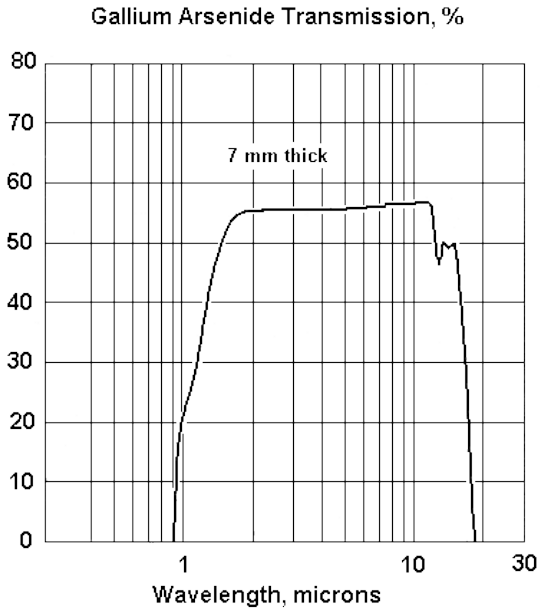

Figure 1.11 The transmission spectrum of Gallium Arsenide. This spectrum also shows the Fresnel reflections, which is why the transmission shown is far below the 100% reported in the regeion of interest from 2 μm to 12 μm. Image courtesy of [114].

A high nonlinear coefficient of 94 pm/V [115] places it ahead of all its competitors, and its figure of merit in the region of 225 [116] is bested only by CdSiP. A high damage threshold of 2 J/cm^2 [110] is also at the top of its class. The combination of all these properties make OP-GaAs an ideal material for mid-infrared frequency conversion devices. It is for this reason that OP-GaAs was chosen for use in the work in this thesis, developing mid-infrared OPO systems for use in spectroscopy applications.

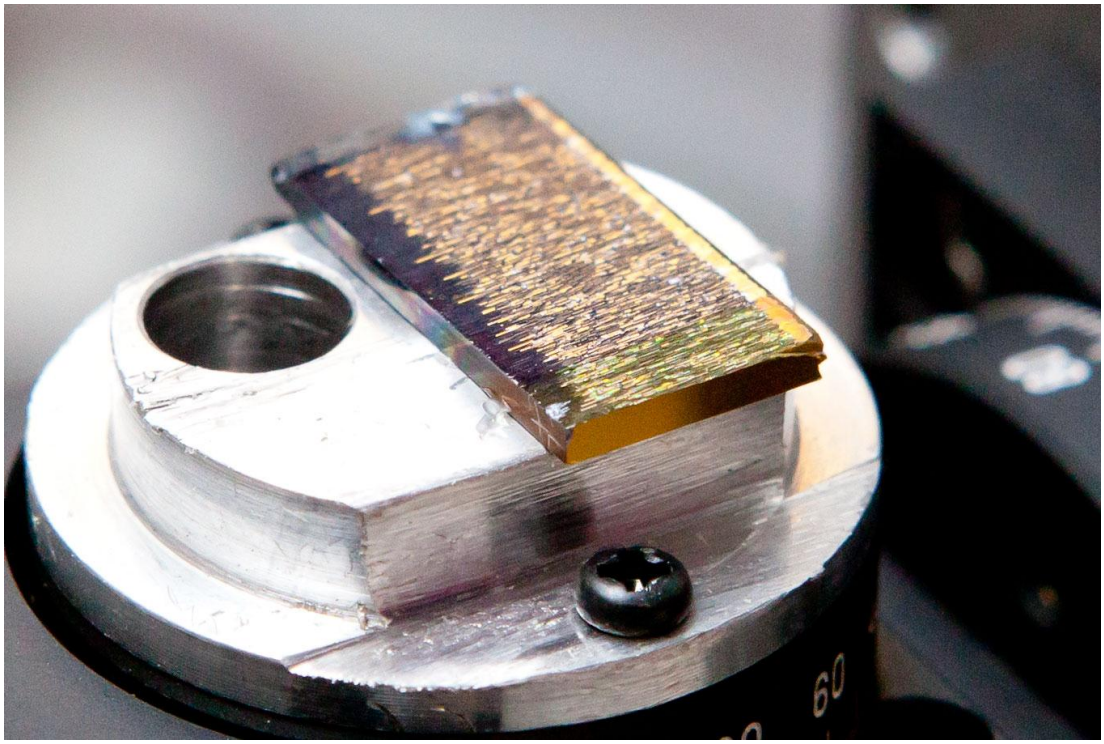

Figure 1.12 A colour photograph of one of the OP-GaAs crystals (26K – see appendix A) which was later implemented in this work.

1.6 Conclusions

The need for tunable mid-IR laser devices has been demonstrated due to the desire to satisfy the demand for such laser sources for applications in this region especially in the context of gas sensing due to the spectroscopic nature of gasses between 6 μm to 12 μm – the so-called chemical fingerprint region. A device which offers 100's of mW of power which is tunable across this entire range would satisfy the application demand for such a laser.

Current solid-state laser sources, both crystalline and fibre, have been explored but no adequate solution has been shown to exist which meets the demands outlined above. Semiconductor lasers were also explored but were also found wanting for such broadly tunable, high-power laser source development. However, nonlinear frequency conversion was found to be a viable path towards the construction of a broadly tunable, truly practicable mid-infrared laser source.

Difference frequency generation was considered as a method for producing a tunable mid-IR laser source to meet the application. However the need to use two separate pump lasers and the additional complications this brings precludes this technique for the purposes of a practical device. By process of elimination, this leaves only parametric downconversion as the most viable means of producing a tunable mid-IR laser source.

A variety of materials were considered as nonlinear conversion media and their suitability was assessed and compared with OP-GaAs – with OP-GaAs showing the greatest potential for source development in this region. This thesis therefore focuses on the development of OP-GaAs based optical parametric oscillator devices.

The 2nd chapter of this thesis discusses the technical and theoretical points of semiconductor disk laser and optical parametric oscillator devices. This is to help orient the reader around the finer points of such devices and how this effects the design and construction of practical laser sources based on them.

The 3rd chapter of this thesis chronicles the construction and characterisation of a pulsed optical parametric oscillator using a Q-switched Tm:YAP laser as a pump source. Discussions on how the device can be improved shall be offered. The limitations of such a device shall also be presented.

The 4th and 5th chapters detail the attempts to construct an intracavity cw-OPO using GaSb semiconductor disk lasers and thorough discussion on what is precluding device operation and a discourse on how these can be overcome shall be delivered.

The 6th and final chapter shall contain a summary of the conclusions which can be drawn from this work and improvements which can be made on the researched devices contained herein. A discussion on future work in this field and potential research directions shall also be presented.

1.7 References

1. Maiman, T.H., *Optical and Microwave-optical Experiments in Ruby.* Physical Review Letters, 1960. **4**(11): p. 564-566.
2. Krier, A., H.H. Gao, and Y. Mao, *A room temperature photovoltaic detector for the mid-infrared (1.8-3.4) wavelength region.* Semiconductor Science and Technology, 1998. **13**(8): p. 950.
3. Tittel, F.K., D. Richter, and A. Fried, *Mid-infrared Laser Applications in Spectroscopy*, in *Solid-State Mid-Infrared Laser Sources*. 2003, Springer. p. 458-529.
4. Waynant, R.W., I.K. Ilev, and I. Gannot, *Mid–infrared Laser Applications in Medicine and Biology.* Philosophical Transactions of the Royal Society of London A: Mathematical, Physical and Engineering Sciences, 2001. **359**(1780): p. 635-644.
5. Willer, U., et al., *Near-and Mid-infrared Laser Monitoring of Industrial Processes, Environment and Security Applications.* Optics and Lasers in Engineering, 2006. **44**(7): p. 699-710.
6. Franken, P.A., et al., *Generation of Optical Harmonics.* Physical Review Letters, 1961. **7**(4): p. 118-119.
7. Giordmaine, J.A. and R.C. Miller, *Tunable Coherent Parametric Oscillation in $LiNbO_3$ at Optical Frequencies.* Physical Review Letters, 1965. **14**(24): p. 973-976.
8. Smith, R.G. and J.V. Parker, *Experimental Observation of and Comments on Optical Parametric Oscillation Internal to the Laser Cavity.* Journal of Applied Physics, 1970. **41**(8): p. 3401-3408.
9. Colville, F.G., M.H. Dunn, and M. Ebrahimzadeh, *Continuous-wave, Singly Resonant, Intracavity Parametric Oscillator.* Optics Letters, 1997. **22**(2): p. 75-77.
10. Stothard, D.J.M., *Practical Continuous Wave Optical Parametric Oscillators*, in *Advances in Optical and Photonic Devices*, K.Y. Kim, Editor. 2010, InTech.
11. Rothman, L.S., et al., *The HITRAN2012 Molecular Spectroscopic Database.* Journal of Quantitative Spectroscopy and Radiative Transfer, 2013. **130**: p. 4-50.
12. Elder, I.F. and M.J.P. Payne, *Lasing in Diode-pumped Tm:YAP, Tm,Ho:YAP and Tm,Ho:YLF.* Optics Communications, 1998. **145**(1–6): p. 329-339.
13. Sorokina, I.T., *Crystalline Mid-infrared Lasers*. 2003: Springer.
14. Johnson, L., R. Dietz, and H. Guggenheim, *Optical Maser Oscillation from Ni^{2+} in Mg F_2 Involving Simultaneous Emission of Phonons.* Physical Review Letters, 1963. **11**(7): p. 318.

15. Welford, D. and P.F. Moulton, *Room-temperature Operation of a Co:MgF_2 Laser.* Optics Letters, 1988. **13**(11): p. 975-977.
16. Fedorov, V.V., et al., *3.77-5.05-μm Tunable Solid-state Lasers Based on Fe^{2+}-doped ZnSe Crystals Operating at Low and Room Temperatures.* IEEE Journal of Quantum Electronics, 2006. **42**(9): p. 907-917.
17. Page, R.H., et al., *Cr^{2+}-doped Zinc Chalcogenides as Efficient, Widely Tunable mid-infrared Lasers.* IEEE Journal of Quantum Electronics, 1997. **33**(4): p. 609-619.
18. Carrig, T.J., et al., *Mode-locked Cr^{2+}:ZnSe Laser.* Optics Letters, 2000. **25**(3): p. 168-170.
19. Demirbas, U. and A. Sennaroglu, *Intracavity-pumped Cr^{2+}:ZnSe Laser with Ultrabroad Tuning Range Between 1880 and 3100 nm.* Optics Letters, 2006. **31**(15): p. 2293-2295.
20. Tolstik, N., E. Sorokin, and I.T. Sorokina, *Graphene Mode-locked Cr:ZnS Laser with 41 fs Pulse Duration.* Optics Express, 2014. **22**(5): p. 5564-5571.
21. Hempler, N., et al., *Semiconductor Disk Laser Pumped Cr^{2+}:ZnSe lasers.* Optics Express, 2009. **17**(20): p. 18136-18141.
22. Hempler, N., et al. *Semiconductor Disk Laser Pumped Cr^{2+}:Chalcogenide Lasers*. in *Conference on Lasers and Electro-Optics/Quantum Electronics and Laser Science Conference and Photonic Applications Systems Technologies*. 2008. San Jose, California: Optical Society of America.
23. Pollock, C.R., *Optical Properties of Laser-active Color Centers.* Journal of Luminescence, 1986. **35**(2): p. 65-78.
24. Gellermann, W., *Color Center Lasers.* Journal of Physics and Chemistry of Solids, 1991. **52**(1): p. 249-297.
25. Mollenauer, L.F. and D.H. Olson, *Broadly Tunable Lasers Using Color Centers.* Journal of Applied Physics, 1975. **46**(7): p. 3109-3118.
26. Dieke, G.H. and H.M. Crosswhite, *The Spectra of the Doubly and Triply Ionized Rare Earths.* Applied Optics, 1963. **2**(7): p. 675-686.
27. Weber, M.J., et al., *Laser Action from Ho^{3+}, Er^{3+}, and Tm^{3+}in $YAlO_3$.* IEEE Journal of Quantum Electronics, 1973. **9**(11): p. 1079-1086.
28. Cemy, P. and D. Burns, *Modeling and Experimental Investigation of a Diode-pumped Tm:$YAlO_3$ Laser with a- and b-cut Crystal Orientations.* IEEE Journal of Selected Topics in Quantum Electronics, 2005. **11**(3): p. 674-681.
29. Elder, I.F. and J. Payne, *Diode-pumped, Room-temperature Tm:YAP Laser.* Applied Optics, 1997. **36**(33): p. 8606-8610.
30. Stoneman, R.C. and L. Esterowitz, *Efficient 1.94 μm Tm:YALO Laser.* IEEE Journal of Selected Topics in Quantum Electronics, 1995. **1**(1): p. 78-81.
31. Li, C., et al., *Diode-pumped High-efficiency Tm:YAG Lasers.* Optics Express, 1999. **4**(1): p. 12-18.
32. Schellhorn, M., et al. *High-Power Diode-Pumped Tm:YLF Slab Laser*. in *Lasers and Electro-Optics 2009 and the European Quantum Electronics Conference. CLEO Europe - EQEC 2009. European Conference on*. 2009.
33. Li, J., et al., *A 200 W INNOSLAB Tm:YLF Laser.* Laser Physics Letters, 2013. **10**(5): p. 055002.

34. Strauss, H.J., et al., *Tm:YLF Slab Wavelength-selected Laser.* Optical Materials Express, 2012. **2**(8): p. 1165-1170.
35. Han, L., et al., *High Power Slab Tm:YAP Laser Dual-end-pumped by Fiber Coupled Laser Diodes.* Optical and Quantum Electronics, 2015. **47**(5): p. 1055-1061.
36. Cheng, X., et al., *High-power Diode-end-pumped Tm:YAP and Tm:YLF Slab Lasers.* Chinese Optics Letters, 2011. **9**(9): p. 091406.
37. Lu, Y., et al., *Anisotropy of thermal and spectral characteristics in Tm:YAP laser crystals.* Journal of Alloys and Compounds, 2008. **453**(1–2): p. 482-486.
38. Lu, Y., et al., *Growth and optical properties of Tm:$YAlO_3$ single crystals with different Tm concentrations.* Journal of Alloys and Compounds, 2007. **429**(1–2): p. 296-300.
39. Henderson, S.W., et al., *Eye-safe Coherent Laser Radar System at 2.1 μm using Tm,Ho:YAG Lasers.* Optics Letters, 1991. **16**(10): p. 773-775.
40. Tso Yee, F., et al., *Spectroscopy and Diode Laser-pumped Operation of Tm,Ho:YAG.* IEEE Journal of Quantum Electronics, 1988. **24**(6): p. 924-933.
41. Lamrini, S., et al. *High-Power Ho:YAG Laser in-Band Pumped by Laser Diodes at 1.9 μm and Wavelength-Stabilized by a Volume Bragg Grating*. in *Lasers, Sources and Related Photonic Devices*. 2010. San Diego, California: Optical Society of America.
42. Sudesh, V. and K. Asai, *Spectroscopic and Diode-pumped-laser Properties of Tm, Ho:YLF; Tm, Ho:LuLF; and Tm, Ho:LuAG Crystals: a Comparative Study.* Journal of the Optical Society of America B, 2003. **20**(9): p. 1829-1837.
43. Pollnau, M. and S.D. Jackson, *Mid-infrared Fiber Lasers*, in *Solid-State Mid-Infrared Laser Sources*. 2003, Springer. p. 225-261.
44. Reisfeld, R. and M. Eyal, *Possible Ways of Relaxations for Excited States of Rare Earth Ions in Amorphous Media.* Le Journal de Physique Colloques, 1985. **46**(C7): p. C7-349-C7-355.
45. Wetenkamp, L., *Charakterisierung von Laseraktiv Dotierten Schwermetallfluorid-Gläsern und Faserlasern*. 1991: Technische Hochschule Carolo-Wilhelmina zu Braunschweig.
46. Hewak, D., et al., *Gallium lanthanum sulphide optical fibre for active and passive applications.* 1996.
47. Schweizer, T., et al., *Rare-earth Doped Chalcogenide Glass Fibre Laser.* Electronics Letters, 1997. **33**(5): p. 414-416.
48. Hayward, R., et al., *Efficient Cladding-pumped Tm-doped Silica Fibre Laser with High Power Singlemode Output at 2 μm.* Electronics Letters, 2000. **36**(8): p. 711-712.
49. Jackson, S., *8.8 W Diode-cladding-pumped Tm^{3+}, Ho^{3+}-doped Fluoride Fibre Laser.* Electronics Letters, 2001. **37**(13): p. 821-822.
50. Smart, R.G., et al., *Continuous-wave Oscillation of Tm $^{3+}$-doped Fluorozirconate Fibre Lasers at around 1.47 μm, 1.9 μm and 2.3 μm when Pumped at 790 nm.* Optics Communications, 1991. **82**(5): p. 563-570.
51. Jackson, S.D., T.A. King, and M. Pollnau, *Diode-Pumped 1.7-W Erbium 3-μm Fiber Laser.* Optics Letters, 1999. **24**(16): p. 1133-1135.

52. Sumiyoshi, T., et al., *High-power Continuous-wave 3-and 2-μm Cascade Ho^{3+}: ZBLAN Fiber Laser and its Medical Applications.* IEEE Journal of Selected Topics in Quantum Electronics, 1999. **5**(4): p. 936-943.
53. Carbonnier, C., H. Többen, and U. Unrau, *Room Temperature CW Fibre Laser at 3.22 μm.* Electronics Letters, 1998. **34**(9): p. 893-894.
54. Többen, H., *Room Temperature CW Fibre Laser at 3.5 μm in Er^{3+}-doped ZBLAN Glass.* Electronics Letters, 1992. **28**(14): p. 1361-1362.
55. Schneide, J., C. Carbonnier, and U.B. Unrau, *Characterization of a Ho^{3+}-doped Fluoride Fiber Laser with a 3.9-μm Emission Wavelength.* Applied Optics, 1997. **36**(33): p. 8595-8600.
56. Schweizer, T., et al., *Infrared Emission from Holmium Doped Gallium Lanthanum Sulphide Glass.* Infrared Physics & Technology, 1999. **40**(4): p. 329-335.
57. Schweizer, T., et al., *Infrared Emission and Ion–ion Interactions in Thulium- and Terbium-Doped Gallium Lanthanum Sulfide Glass.* Journal of the Optical Society of America B, 1999. **16**(2): p. 308-316.
58. Schweizer, T., et al., *Spectroscopic Data of the 1.8-, 2.9-, and 4.3-μm Transitions in Dysprosium-doped Gallium Lanthanum Sulfide Glass.* Optics Letters, 1996. **21**(19): p. 1594-1596.
59. Coldren, L.A., S.W. Corzine, and M.L. Mashanovitch, *Diode Lasers and Photonic Integrated Circuits*. Vol. 218. 2012: John Wiley & Sons.
60. Jones, E.D., et al., *Progress in Semiconductor Materials for Optoelectronic Applications Symposium held in Boston, Massachusetts on November 26-29, 2001*. 2002, DTIC Document.
61. Kim, J., et al., *Room-temperature 2.5 μm InGaAsSb/AlGaAsSb Diode Lasers Emitting 1 W Continuous Waves.* Applied Physics Letters, 2002. **81**(17): p. 3146-3148.
62. Schulz, N., et al., *High-brightness Long-wavelength Semiconductor Disk Lasers.* Laser & Photonics Reviews, 2008. **2**(3): p. 160-181.
63. Hempler, N., et al. *Tuning and Brightness Optimization of High-performance GaSb-Based Semiconductor Disk Lasers from 1.86 to 2.80μm*. in *Lasers and Electro-Optics 2009 and the European Quantum Electronics Conference. CLEO Europe-EQEC 2009. European Conference on*. 2009. IEEE.
64. Cerutti, L., et al., *GaSb-based VCSELs Emitting in the Mid-infrared Wavelength Range (2–3μm) Grown by MBE.* Journal of Crystal Growth, 2009. **311**(7): p. 1912-1916.
65. Choi, H., et al., *175 K Continuous Wave Operation of InAsSb/InAlAsSb Quantum-well Diode Lasers Emitting at 3.5 μm.* Applied Physics Letters, 1996. **68**(21): p. 2936-2938.
66. Partin, D.L. and C.M. Thrush, *Wavelength Coverage of Lead-europium-selenide-telluride Diode Lasers.* Applied Physics Letters, 1984. **45**(3): p. 193-195.
67. Preier, H., *Physics and Applications of IV-VI Compound Semiconductor Lasers.* Semiconductor Science and Technology, 1990. **5**(3S): p. S12.
68. Stillman, G.E., et al., *Volume Excitation of an Ultrathin Single-mode CdSe Laser.* Applied Physics Letters, 1966. **9**(7): p. 268-269.

69. Kuznetsov, M., et al., *High-power (>0.5-W CW) Diode-pumped Vertical-external-cavity Surface-emitting Semiconductor Lasers with Circular TEM_{00} Beams.* IEEE Photonics Technology Letters, 1997. **9**(8): p. 1063-1065.
70. Kuznetsov, M., et al., *Design and Characteristics of High-power (0.5W CW) Diode-pumped Vertical-external-cavity Surface-emitting Semiconductor Lasers with Circular TEM_{00} Beams.* IEEE Journal of Selected Topics in Quantum Electronics, 1999. **5**(3): p. 561-573.
71. Kaspar, S., et al., *Recent Advances in 2-µm GaSb-Based Semiconductor Disk Laser—Power Scaling, Narrow-Linewidth and Short-Pulse Operation.* IEEE Journal of Selected Topics in Quantum Electronics, 2013. **19**(4): p. 1501908-1501908.
72. Cerutti, L., et al., *High Temperature Continuous Wave Operation of Sb-Based Vertical External Cavity Surface Emitting Laser near 2.3µm.* Journal of Crystal Growth, 2004. **268**(1–2): p. 128-134.
73. Hopkins, J.M., et al., *High-power, (AlGaIn)(AsSb) Semiconductor Disk Laser at 2.0 µm.* Optics Letters, 2008. **33**(2): p. 201-203.
74. Ouvrard, A., et al., *Single-frequency Tunable Sb-based VCSELs Emitting at 2.3 µm.* IEEE Photonics Technology Letters, 2005. **17**(10): p. 2020-2022.
75. Paajaste, J., et al., *High-power and Broadly Tunable GaSb-based Optically Pumped VECSELs Emitting near 2µm.* Journal of Crystal Growth, 2009. **311**(7): p. 1917-1919.
76. Rattunde, M., et al., *GaSb-based 2. X µm Quantum-well Diode Lasers with Low Beam Divergence and High Output Power.* Applied physics letters, 2006. **88**(8): p. 1115.
77. Holl, P., et al., *Recent Advances in Power Scaling of GaSb-based Semiconductor Disk Lasers.* 2015.
78. Faist, J., et al., *Quantum Cascade Laser.* Science, 1994. **264**(5158): p. 553-556.
79. Scalari, G., et al., *THz and sub-THz Quantum Cascade Lasers.* Laser & Photonics Reviews, 2009. **3**(1-2): p. 45-66.
80. Yang, Q., et al., *Room-temperature Short-wavelength (3.7-3.9 µm) GaInAs/AlAsSb Quantum-cascade Lasers.* Applied Physics Letters, 2006. **88**(12): p. 1127.
81. Zhang, S., et al., *3.1 µm Room Temperature InGaAs/AlAsSb/InP Quantum Cascade Lasers.* Applied Physics Letters, 2009. **94**(3): p. 1106.
82. Köhler, R., et al., *Low-threshold Quantum-cascade Lasers at 3.5 THz (λ= 85 µm).* Optics Letters, 2003. **28**(10): p. 810-812.
83. Ebrahimzadeh, M. and M.H. Dunn, *Optical Parametric Oscillators*, in *Handbook of Optics*. 2004, McGraw-Hill.
84. Sutherland, R.L., *Handbook of Nonlinear Optics*. Second Edition ed. 2003: Marcel Dekker.
85. Bass, M., et al., *Optical Mixing.* Physical Review Letters, 1962. **8**(1): p. 18-18.
86. Abedin, K.S., et al., *Difference Frequency Generation of 5–18 µm in a $AgGaSe_2$ Crystal.* Applied Optics, 1998. **37**(9): p. 1642-1646.
87. Scheller, M., et al., *Room Temperature Continuous Wave Milliwatt Terahertz Source.* Optics Express, 2010. **18**(26): p. 27112-27117.

88. Momose, T., T. Wakabayashi, and T. Shida, *Tunable-narrow-linewidth Continuous-wave Mid-infrared Light Generation by Difference-frequency Mixing.* Journal of the Optical Society of America B, 1996. **13**(8): p. 1706-1712.
89. Golubovic, B. and M. Reed, *All-solid-state Generation of 100-kHz Tunable Mid-infrared 50-fs Pulses in Type I and Type II $AgGaS_2$.* Optics Letters, 1998. **23**(22): p. 1760-1762.
90. Nienhuys, H.-K., et al., *Generation of Mid-infrared Pulses by X (3) Difference Frequency Generation in CaF_2 and BaF_2.* Optics Letters, 2001. **26**(17): p. 1350-1352.
91. Hofmann, D., et al., *Quasi-phase-matched Difference-frequency Generation in Periodically Poled Ti: $LiNbO_3$ Channel Waveguides.* Optics Letters, 1999. **24**(13): p. 896-898.
92. Hong, J., et al., *Broadly Tunable Femtosecond Pulse Generation in the near and Mid-infrared.* Applied Optics, 1997. **36**(9): p. 1894-1897.
93. Fenimore, D., et al., *Rubidium Titanyl Arsenate Difference-Frequency Generation and Validation of New Sellmeier Coefficients.* Journal of the Optical Society of America B, 1996. **13**(9): p. 1935-1940.
94. Petrov, V., et al., *Widely Tunable Continuous-wave Mid-infrared Laser Source Based on Difference-frequency Generation in $AgGaS_2$.* Applied Optics, 1998. **37**(21): p. 4925-4928.
95. Vodopyanov, K. and P. Schunemann, *Efficient Difference-frequency Generation of 7-20-μm Radiation in $CdGeAs^2$.* Optics Letters, 1998. **23**(14): p. 1096-1098.
96. Choy, M.M. and R.L. Byer, *Accurate Second-order Susceptibility Measurements of Visible and Infrared Nonlinear Crystals.* Physical Review B, 1976. **14**(4): p. 1693.
97. Bliss, D.F., et al., *Epitaxial growth of thick GaAs on orientation-patterned wafers for nonlinear optical applications.* Journal of Crystal Growth, 2006. **287**(2): p. 673-678.
98. Zawilski, K.T., et al., *Large Aperture Single Crystal $ZnGeP_2$ for High-energy Applications.* Journal of Crystal Growth, 2008. **310**(7): p. 1891-1896.
99. Das, S., et al., *Linear and Nonlinear Optical Properties of $ZnGeP_2$ Crystal for Infrared Laser Device Applications: Revisited.* Applied Optics, 2003. **42**(21): p. 4335-4340.
100. *Eksma Optics*. 24/11/2015]; Available from: http://eksmaoptics.com/out/pictures/master/product/4/zngeptransmision.jpg.
101. Schunemann, P.G., et al. *$CdSiP^2$: A New Nonlinear Optical Crystal for 1-and 1.5-Micron-Pumped Mid-IR Generation*. in *Advanced Solid-State Photonics*. 2009. Optical Society of America.
102. Petrov, V., et al., *Noncritical Singly Resonant Optical Parametric Oscillator Operation near 6.2 μm Based on a $CdSiP_2$ Crystal Pumped at 1064 nm.* Optics Letters, 2009. **34**(16): p. 2399-2401.
103. Schunemann, P.G., et al. *New Mid-IR Nonlinear Optical Crystal: $CdSiP^2$*. in *Conference on Lasers and Electro-Optics*. 2008. Optical Society of America.

104. Yu, X., et al., *Single-phase Growth Studies of GaP on Si by Solid-source Molecular Beam Epitaxy.* Journal of Vacuum Science & Technology B, 2004. **22**(3): p. 1450-1454.
105. Bond, W., *Measurement of the Refractive Indices of Several Crystals.* Journal of Applied Physics, 1965. **36**(5): p. 1674-1677.
106. Schaar, J.E., et al., *Terahertz Sources Based on Intracavity Parametric Down-conversion in Quasi-phase-matched Gallium Arsenide.* IEEE Journal of Selected Topics in Quantum Electronics, 2008. **14**(2): p. 354-362.
107. Schunemann, P.G., et al. *Recent Advances in All-Epitaxial Growth and Properties of Orientation-Patterned Gallium Arsenide (OP-GaAs)*. in *Conference on Lasers and Electro-Optics/International Quantum Electronics Conference*. 2009. Baltimore, Maryland: Optical Society of America.
108. Eyres, L., et al., *All-epitaxial Fabrication of Thick, Orientation-patterned GaAs Films for Nonlinear Optical Frequency Conversion.* Applied Physics Letters, 2001. **79**(7): p. 904-906.
109. Yu, X., et al., *Growth of GaAs with Orientation-patterned Structures for Nonlinear Optics.* Journal of Crystal Growth, 2007. **301–302**(0): p. 163-167.
110. Kieleck, C., et al., *High-efficiency 20–50 kHz Mid-infrared Orientation-patterned GaAs Optical Parametric Oscillator Pumped by a 2 μm Holmium Laser.* Optics Letters, 2009. **34**(3): p. 262-264.
111. Schunemann, P.G., et al. *Recent Advances in All-epitaxial Growth and Properties of Orientation-patterned Gallium Arsenide (OP-GaAs)*. in *Lasers and Electro-Optics, 2009 and 2009 Conference on Quantum electronics and Laser Science Conference. CLEO/QELS 2009. Conference on*. 2009.
112. Schunemann, P.G., et al. *2.05-μm-Laser-Pumped Orientation-Patterned Gallium Arsenide (OPGaAs) OPO*. in *Conference on Lasers and Electro-Optics/Quantum Electronics and Laser Science and Photonic Applications Systems Technologies*. 2005. Baltimore, Maryland: Optical Society of America.
113. Vodopyanov, K.L., et al., *Optical Parametric Oscillation in Quasi-phase-matched GaAs.* Optics Letters, 2004. **29**(16): p. 1912-1914.
114. *Almaz Optics*. 24/11/2015]; Available from: http://www.almazoptics.com/GaAs.htm.
115. Skauli, T., et al., *Measurement of the Nonlinear Coefficient of Orientation-patterned GaAs and Demonstration of Highly Efficient Second-harmonic Generation.* Optics Letters, 2002. **27**(8): p. 628-630.
116. Skauli, T., et al., *Improved Dispersion Relations for GaAs and Applications to Nonlinear Optics.* Journal of Applied Physics, 2003. **94**(10): p. 6447-6455.

Chapter 2
Principles of GaSb Semiconductor Disk Lasers, and Optical Parametric Oscillators

2.1 Introduction

In the previous chapter the motivation behind the work in this thesis, along with both progress in and the current state of the art in the relevant fields were discussed. In this chapter the relevant background concepts and theory underpinning the work contained in this thesis will be presented. Firstly, the operating principles and design considerations, especially those relating to the thermal properties, of semiconductor disk lasers (SDLs) shall be discussed. The parameters specifically relevant to GaSb SDL systems shall also be presented and the impact that these have on design considerations shall be discussed, in particular, solutions to the problem of extracting heat from the gain medium. Next, the principles of operation behind optical parametric oscillators (OPOs) shall be presented, with the measures required to demonstrate practical and efficient OPO devices being given prominent treatment. This includes a discussion of threshold operating conditions, the benefits and disadvantages of intracavity and extracavity techniques, as well as the use of quasi-phase matching techniques to access non-linearities, which would be unavailable through conventional phase matching.

2.2 GaSb Based SDL Structures

2.2.1 Introduction to Semiconductor Disk Lasers

Semiconductor disk lasers (SDLs), also known by the name vertical external cavity surface emitting lasers (VECSELS) were originally demonstrated in 1966,

but their full potential was not realised until the late 1990's as a means to overcome one of the key problems of conventional edge-emitting semiconductor lasers – how to produce high-power lasers with high beam quality, fundamental spatial mode emission [1-3]. While diode lasers are efficient and affordable sources of high-power laser emission, the spatial and spectral mode quality of these devices is often less than is desirable for many scientific and commercial applications which require high beam quality sources, such as areas within non-linear optics including second harmonic generation and parametric downconversion [4-6].

SDLs differ from conventional semiconductor lasers in several key ways. The most fundamental difference is in the directions of emission from the device – while edge emitting devices emit parallel to the plane of the device, SDLs emit perpendicular to the plain of the chip [1]. This allows for larger emission areas, which helps with both producing good beam quality and with thermal dissipation. However, some of the advantages gained by enlarging the emission area can be lost in current injection based devices, as the large area makes an even carrier distribution impossible from edge or ring contacts, leading to a collapse in beam quality in emission diameters larger than ~10 μm. This can be overcome by optically pumping the gain medium [1, 4, 7]. By optically pumping the SDL, it is possible to evenly excite carriers over a wide area in the semiconductor material and also extirpates the need to dope the material with impurities, significantly simplifying the growth of the chips.

Another key advantage of semiconductor disk lasers is their thin disk-like form – by having pump diameters which are larger than the thickness of the chip it is possible to achieve near unidirectional heat flow, which significantly ameliorates, and indeed, at low pump powers almost eliminates entirely, thermal lensing in the gain medium. This is analogous to solid-state thin-disc lasers used to give high-power, good-beam-quality solid-state lasers [8, 9]. To continue the comparison with conventional dielectric solid-state lasers, the use of quantum wells as the gain medium allows for tailoring of the emission wavelength within the capabilities of the semiconductor materials used, unlike dielectric solid state

lasers whose emission is fixed by the ion transition and the host material electronic structure.

The final major difference between SDLs and conventional semiconductor lasers, and its antecedent vertical-cavity surface emitting lasers (VCSELS), is the use of an external mirror to provide feedback. This allows for both shaping and manipulation of the spatial mode inside the cavity, mode-matching between pump and resonator mode for improved power scaling, as well as allowing for the insertion of intracavity elements. This enables both manipulation of the spatial, spectral and temporal properties of the laser as well as allowing access to the high intracavity field, which is perfect for the performance of non-linear physics, which requires high intensities to enact [1, 2, 4, 7, 10-13].

In the next section, SDL device structures shall be outlined along with the composition of the devices used in this work.

2.2.2 SDL Structure and Design

SDL chips consist of multiple semiconductor layers grown on top of each other by means of epitaxy. These layers are subdivided within the structure into several distinct regions which each serve a specific purpose. These layers from the cavity side down are the cap, confinement layer, gain region/pump absorbing layer, distributed Bragg reflector (DBR) and finally the substrate [2, 4, 7]. A diagram of how such a layered structure is composed is shown in figure 2.1.

However, for each of these component layers to function correctly, it is necessary for them to be made from different materials. This can give rise to excessive strain within the material system which can lead to the propagation of defects throughout the device, or even worse, structural failure of the chip [4, 7]. Neither of these is conducive to optimal operation of the device. To prevent this, the material system is chosen such that the various semiconductor alloys used in the device are lattice matched as closely as possible, which reduces the strain

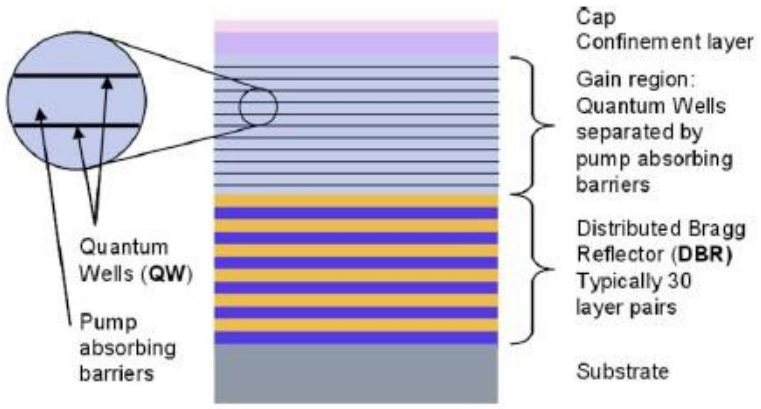

Figure 1. A diagram showing the structure of an SDL device, showing the component layers of the SDL structure.

introduced by lattice mismatch [4, 7, 11, 14-16]. For SDL devices operating in the 2 μm region (AlGaIn)(AsSb) is the material system of choice [11, 14, 17]. This system is well lattice matched, with a shared lattice constant of ~6.1 Å, which minimizes the unnecessary strain within the device. An energy bandgap diagram showing the (AlGaIn) (AsSb) material system and highlighting the materials important in Mid-IR SDL construction is shown in figure 2.2 [17].

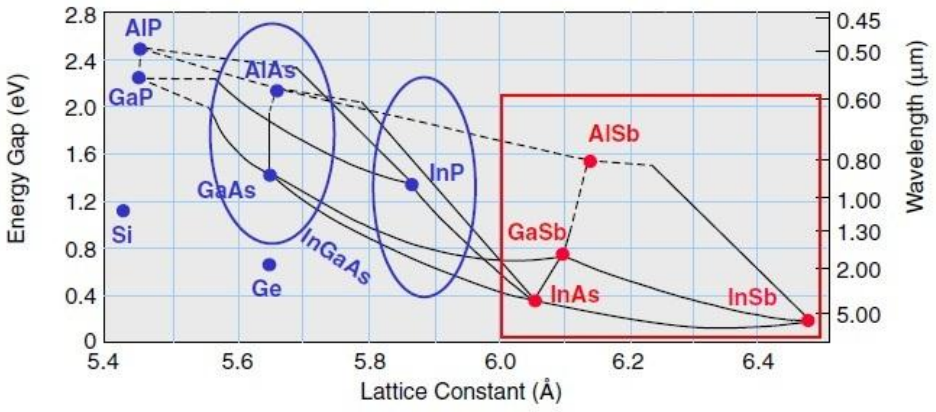

Figure 2.2 An energy badgap diagram (energy gap versus lattice constant) of currently available compound semiconductors with the long wavelength, small bandgap antimonides highlighted in red. Figure adapted from [17]

From the materials highlighted in figure 2.2, it is GaSb quantum wells which are chosen as the gain material for 2.X μm disk lasers and forms the core of the (AlGaIn)(AsSb) material system [11, 14]. In the following subsections the various component parts of the SDL structure shall be described in detail.

2.2.2.1 The Gain/Pump Absorbing Region

In the previous section a brief discussion of the structure of an SDL was presented along with some of the material considerations involved in designing and constructing an SDL. In this section a more in depth look into the gain region in the SDL, arguably the most important structure within the device, shall be undertaken.

The active region of an SDL structure can be separated out into two key components – the pump absorbing barriers and the quantum well regions where laser action takes place. A diagram of this region is shown in figure 2.3. The barrier material is chosen such that it has a larger bandgap than the energy of the desired emission but a smaller bandgap than the corresponding pump wavelength. This leads to efficient absorption of the pump energy and after a short 'relaxation' time the confinement of the carriers within the quantum well gain regions. Using the barrier layers to absorb the pump light separately allows for easier tailoring and optimisation of the absorption properties of the SDL by decoupling them from the devices emission properties [4]. For the GaSb quantum wells, AlGaAsSb alloy barriers were chosen in a proportion so as to maximise gain within in the device without compromising structural integrity [14].

The quantum wells within the SDL structure provide the active laser emission region - carrier recombination in the quantum wells being the source of laser photons in the device. To further enhance the gain available within the device, the gain chip is often constructed such that it is an integer number of half wave-lengths long, forming a standing wave within the device. By carefully considering the widths of barrier and spacer layers the quantum wells are then placed at the antinodes of the device to maximise the field in the quantum wells and improve

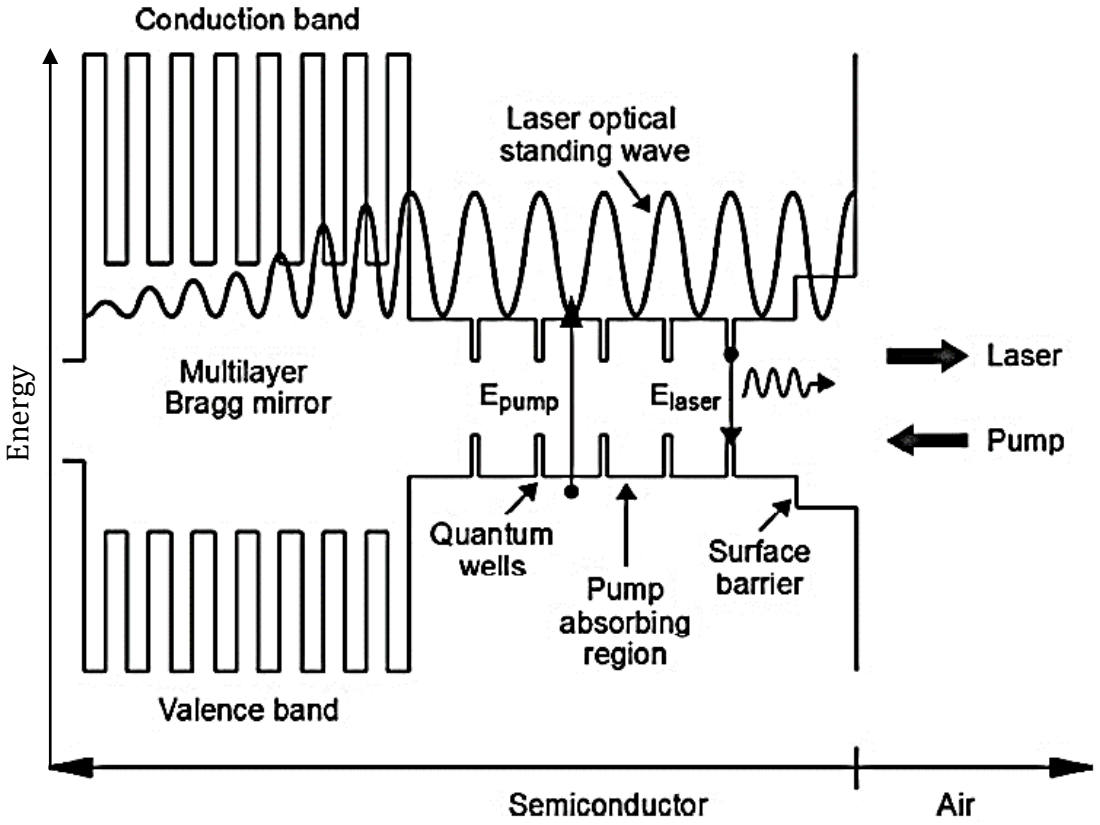

Figure 2.3 A diagram of the band structure within an SDL chip. The chip consists of an active region where pump absorbing barrier material feeds elections in to the quantum wells permitting laser action. Barrier regions are erected around the pump absorbing region to improve electron/hole confinement. In this figure, the wells are placed at the antinodes of the laser field, which is known as a resonant periodic gain (RPG) structure.

efficiency, as shown in figure 2.3 [2, 4, 7, 14]. This is known as a resonant periodic gain (RPG) structural design. Antiresonant devices are also available, where the quantum wells are not placed at the antinodes of the field, such that there is no strong enhancement of the field within the cavity. These devices sacrifice the higher gain available from the antinodes of the field in return for broader tunability. This can be further enhanced by adding multiple wells per node. For the devices used in this work compressively strained (~1.3 %) wells of GaInSb placed in a resonant configuration were used [14].

For the quantum well structures within SDLs the threshold pump power for operation is given by

$$P_{th} = N_{th}\frac{h\nu\left(N_w L_w A_p\right)}{\eta_{abs}\tau(N_{th})} \quad (equation\ 2.1)$$

Where N_{th} is the threshold carrier concentration, hν is the laser photon energy, N_w is the number of quantum wells, L_w is the thickness of the quantum wells, A_p is the area of the incident pump beam, η_{abs} is the absorption efficiency of the device and $\tau(N_{th})$ is the carrier lifetime at the threshold carrier concentration [2, 4].

The output power from the laser is then given by

$$P_{las} = (P_p - P_{th})\eta_{diff} \ (equation\ 2.2)$$

Where P_p is the pump power and η_{diff} is the differential efficiency of the device, which consists of four components – the absorption efficiency, the output efficiency, which is the ratio of useful output coupling to the total loss in the device, the quantum defect, which is the fractional energy difference between the absorbed and emitted photons and finally the radiative efficiency, which is the ratio of radiative carrier recombination to the total carrier recombination in the device [2, 4].

2.2.2.2 The Distributed Bragg Reflector

The next most prominent component in the SDL structure is the distributed Bragg reflector which is grown upon the rear of the chip. With the necessary constraints on both the thickness and the number of quantum wells in the SDL, the relative gain available from an SDL is small (typically a few %) compared to most conventional solid-state lasers (typically greater than 30 %). As a result, SDLs are less able to tolerate large losses within the cavity, thus requiring that the mirrors used within the cavity are of the highest reflectivity possible. It is to this end, that a high reflector (R>99.5 %) is grown up the rear surface of SDL chips [1]. The Bragg reflector consists of pairs of high/low refractive index semiconductor layers arranged in a quarter wave stack. This provides constructive interference on reflection and creates a high reflectivity mirror at the operating wavelength of the device. However, the large number of layers and therefore relatively thick mirror region when compared to the active region acts as a thermal impedance

barrier for extracting heat from the gain medium. This effect is exacerbated for longer wavelength operation. The reflectivity of the Bragg reflector is given by

$$R_{DBR} = \left(\frac{1 - qp^{2N}}{1 + qp^{2N}}\right) \ (equation\ 2.3)$$

Where q is the refractive index contrast between the uppermost layer of the DBR and gain region, p is the refractive index contrast between the high and low refractive index pair in the Bragg reflector and N is the number of layers in the DBR [4]. From the above equation, it is clear to see that the greater of number of pairs within the DBR, the higher the reflectivity of the DBR. However, this increases the thermal resistance between the gain region and the back surface of the SDL, hindering effective removal of heat from the gain medium. This shall be discussed further in the following section. It is therefore optimal to have as high a contrast between the refractive indices of the high/low pairs to limit the thickness of the DBR. The DBRs bandwidth is given by

$$\frac{\lambda_{DBR}}{\lambda_c} = \frac{4}{\pi}\sin^{-1}\left(\frac{1 - p}{1 + p}\right) \ (equation\ 2.4)$$

Equation 2.4 shows that, while high refractive index contrast between pairs reduces the number of layers needed in the DBR for high reflectance, it reduces the bandwidth over which the DBR operates. This implies that, for devices where a broad range of operating wavelengths are required, a smaller index contrast and high number of contrasting refractive layers would be necessary, which has thermal implications for such a device, as discussed later in this chapter. For the GaSb based VECSELS used in this work, AlAsSb/AlGaAsSb pairs were used as the high/low refractive index materials in the DBR [14].

2.2.2.3 The Cap, Confinement and Substrate Layers

The final layers in the SDL structure are the cap, confinement and substrate layers. The cap layer simply serves to protect the SDL structure from both physical and chemical damage at the surface. GaSb was chosen for this purpose in the SDLs used in this thesis for the simplicity and reduced cost of its growth

while lattice matching to the rest of the layers. The substrate layer is the base semiconductor wafer that provides a thick, rigid substrate for the epitaxial growth of the chips to occur on, once again GaSb being the material of choice for the same reasons as for the cap. The confinement layer of the SDL is specifically selected such that it has a larger bandgap than the barrier layers in the gain region, this prevents carriers from leaking out of the gain region to the surface where they can recombine non-radiatively confining recombination to the gain region. An alloy of AlGaAsSb was implemented in the SDL samples used in this thesis for this purpose. The final purpose of the confinement layer is to set the position of the surface of the structure in order to set the surface reflectivity and therefore the standing-wave field strength within the structure to enhance (or reduce) the RPG confinement. In the following section, the thermal management of SDL structures shall be explored and several strategies presented and discussed [14].

2.3 Thermal Management in SDLs

Much like any other laser gain medium, the most constraining factor in realising high-power SDL performance is thermal effects in the gain medium. This can be due to a number of reasons from heating the gain medium until it structurally fails, thermally induced lensing spoiling the beam quality or some other undesirable thermal effect. In the case of SDLs the drifting of the resonant periodic gain in the device with temperature, along with the thermal shift in peak wavelength of operation of the quantum wells, leads to a rollover of the gain at high temperatures [4, 18]. Both of these are typically red-shifts, yet they occur at differing rates, for example the shift in the micro-cavity resonance of the SDL is 0.3 nm/K while the quantum well emission shifts at a rate of about 0.1 nm/K for GaAs based devices [2, 4, 7, 18]. As such, the peak gain of the SDL occurs when the microcavity resonance overlaps with peak quantum well emission at a specific temperature. This leads to SDLs being grown such that they are designed to operate at an optimum internal temperature. The room temperature emission of the quantum wells is blue shifted relative to the microcavity resonance so that

heating of the gain medium brings the SDL to ideal operating temperature. Of course, for effective power scaling of the device, it would be ideal to reach the optimum operating temperature for the highest absorbed pump power available, and so effective thermal management in SDLs is critically important. In the next subsection an introduction to heat flow in SDLs will be given, while in the following subsection techniques which can improve the heat extraction even further shall be presented.

2.3.1 Introduction to Thermal Management in SDLs

In the previous section the importance of maintaining an operating temperature of the SDL close to a pre-designed value in power scaling the device was outlined. To do this, an understanding of heat flow in the SDL structure is required. In this subsection the heat flow in an SDL shall be explored and the relevant design parameters and their implications shall be presented.

To first understand heat flow in an SDL, the effects of its thin-disk-like structure must first be considered. With a pump spot-size which is larger in diameter than the thickness of the pumped region, the heat flow in the device is approximately one dimensional towards the faces of the gain medium [8]. This makes the two faces of the SDL the most effective places to cool the laser from. We shall only consider heat extraction through the back surface of the SDL in this section, as cooling from here is the simplest geometry to implement as it does not require inserting anything extra into the cavity.

If the SDL is cooled from the back surface, this causes the heat to conduct from the active region through the DBR layers and the substrate to the heatsink, which is used to maintain an approximate temperature at the interface. Therefore, we must consider the thermal impedance introduced by the substrate and particularly the impedance introduced by the layers of the DBR when examining the heat extraction from the device.

For a composite series of thin layers of different materials the thermal conductivity in the longitudinal and radial directions is given by

$$k_l = \sum_i t_i \,/\, \sum_i \frac{t_i}{k_i} \quad (equation\ 2.5)$$

$$k_r = \sum_i t_i k_i \,/\, \sum_i t_i \quad (equation\ 2.6)$$

Where k_l and k_r are the longitudinally and radially averaged thermal conductivities of the overall structure respectively here, t_i is the thickness of the ith layer and k_i is the thermal conductivity of the ith layer [4]. From equations 2.5 and 2.6 it can be seen that increasing the number of layers, and therefore the thickness of the DBR, increases the total thermal impedance between the gain region and the heatsink. This in turn reduces the effective heat extraction from the device. It should be noted that in both of the above equations the simplifying assumption has been made that there is no thermal impedance at the interfaces between the layers themselves, which is not really the case. In light of the aforementioned points, it is best practice to use as few layers in the DBR as possible consistent with suitable reflectivity. The values for the GaSb substrate and the materials used in the DBR (AlAsSb/AlGaAsSb) are shown below in table 2.1.

	GaSb	AlAsSb	AlGaAsSb
Thermal Conductivity (W/m/K)	33	9.8	10.5

Table 2.1 A table of the thermal conductivities of the materials used in the substrate (GaSb) and DBR (AlAsSb/AlGaAsSb) of the SDLs implemented in this thesis [4].

However, it should be noted that the heat extracted through the DBR and substrate alone (fig 2.4-left) is typically not sufficient to ensure good power scaling of the SDL. To improve the thermal extraction from the device to the levels required for multi-Watt output, other techniques must be implemented to augment the heat extraction from the gain medium. In the next subsection several techniques for improving the thermal management of SDLs are presented.

2.3.2 Schemes for Improving Heat Extraction

In the previous section we looked at how heat is extracted from SDLs. In this section, schemes for improving the heat extraction, and therefore the power scaling, from the SDL shall be explored. There are two common schemes which are implemented – either removing the substrate to reduce the thermal impedance between the gain region and the rear surface of the SDL (known as a thin device), or the introduction of an intracavity heatspreader to extract and disperse heat from the front of the SDL [4, 11, 14, 18, 19]. In the following subsections we shall discuss both methods in more detail, beginning with the removal of the substrate.

2.3.2.1. Removal of the Substrate (the thin device approach)

One scheme to improve the heat extraction from an SDL is to remove the substrate and solder (usually with a highly thermally conductive metal such as gold) the chip straight to the heatsink. By removing the substrate, a significant thermal impedance between the gain region and the heatsink is removed. This approach is particularly effective for SDL chips where the high/low refractive index materials of the DBR have good thermal conductivity, such as 1μm emitting VECSELs based on GaAs which use GaAs/AlAs mirrors (typical radial and longitudinal thermal conductivities of 69.8 and 61.2 W/m/K) [4, 7, 18]. With a thickness much less than the diameter of the pumped volume, this maximises one dimensional heat flow within the device, allowing for excellent power scaling. Indeed the highest output powers ever recorded from an SDL (106 W) have been achieved using this method [4, 20, 21]. A diagram displaying what a VECSEL prepared in this manner may look like is shown in figure 2.4-centre. However, while this approach is excellent for material systems with good thermal conductivity in the DBR, for those with poorer conductivity (such as the GaSb based material system used in 2 μm SDLs, where a typical 22.5 layer stack has a thickness of 7 μm and a thermal conductivity of 0.01 W/(mm.K), compare with

the GaAs-AlAs stacks typically used in 1 µm SDLs which tend to be 5 µm thick and have a thermal conductivity of about 0.06 W/(mm.K) [22]), another approach must be sought. If the heat cannot be extracted effectively through the back of the chip through the DBR, then it must be extracted through the front surface of the gain material, which we shall now have to consider. This is the crux of the intracavity heatspreader approach (fig 2.4-right), which shall be described in the following subsection.

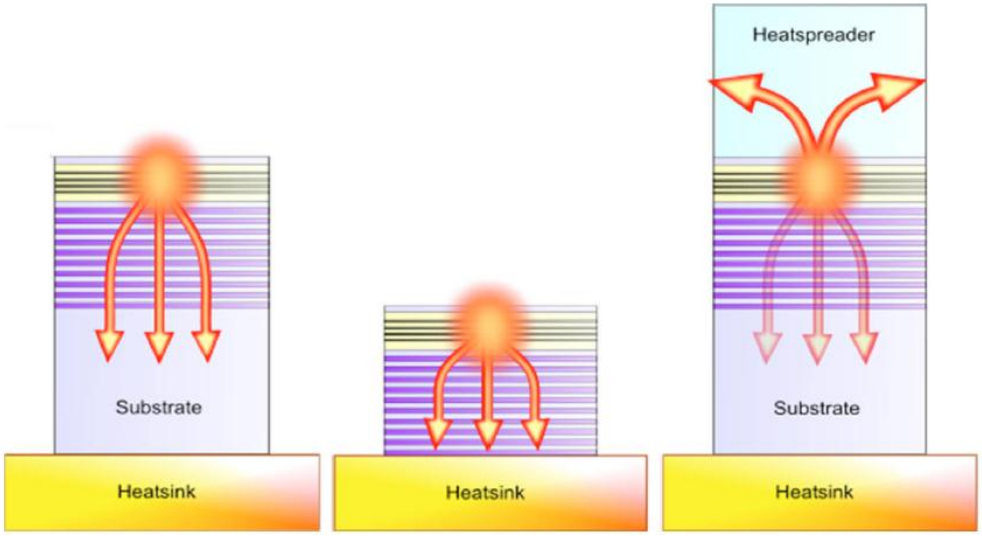

Figure 2.4 A schematic of various thermal management schemes in SDLs. On the left is shown an unprocessed SDL, in the centre an SDL with the substrate removed and on the right and SDL with a heatspreader applied.

2.3.2.2 The Intracavity Heatspreader Approach

One possible approach to improve the heat extraction from the SDL is the implementation of an intracavity heatspreader. With this approach a transparent, high-thermal-conductivity material, such as diamond or silicon carbide is applied to the top surface of the SDL by means of liquid assisted contacting [7, 14, 18]. This allows for efficient extraction of heat from the pumped volume in the gain medium to the heat-spreader, without the need to transport heat through the DBR. From there it is redistributed over the whole SDL before extraction through the rear of the device (reducing the thermal resistance) or extracted straight from the heatspreader to the heat sink. A typical setup of such an SDL is shown in figure 2.4-right. While this approach diminishes the advantages of the thin-disk

approach by adding radial heat flow, as well as introducing additional intracavity loss via the heatspreader, it still allows for significant improvement of the output power to the multiwatt level. In GaSb based SDLs, this is the most effective scheme for extracting heat and power scaling the devices, due to the relatively poor thermal conductance of the DBR [11, 14]. The record output power currently stands at 20 W achieved at Fraunhofer IAF in Freiburg [23]. However efficacy of this technique is critically dependent on how well the heat-spreader is bonded to the gain medium and the implementation of this is not a trivial task.

2.3.3 Conclusions on Thermal Management of SDLs

In the previous section we discussed thermal management in SDL devices as well as several schemes to improve the heat extraction such that high-power multi-watt devices could be realised. This included schemes to both remove the substrate and solder the chips straight to a heatsink and to bond a heatspreader to the top of the device. For the high thermal resistance presented by the DBR in the GaSb based devices used in this thesis, the heatspreader technique has so far proven to be the most effective way to improve power scaling to the multi-watt level in such devices.

It is perhaps also worth mentioning that there are other techniques which can be implemented to reduce the thermal resistance presented by the DBR. Other techniques include wafer fusion techniques where the DBR is grown separately from the rest of the SDL and then fused to the base of the chip, which removes lattice matching constraints from the material by making the choice of DBR material system arbitrary [24, 25]. This allows for a high thermal conductivity DBR to be used regardless of which material system is chosen for the gain region. One other approach which can be implemented is the introduction of a dielectric layer or layers to the DBR [26]. This approach has merit as, while the dielectric layer itself has a lower thermal conductivity than the semiconductor materials used in the DBR, it allows considerably less semiconductor layers to be used, reducing the thickness of the DBR and consequentially the total thermal resistance. However both approaches were not mature technologies when the

samples used in the thesis were grown and so weren't considered for implementation with the current devices.

2.4 Optical Parametric Oscillators

With the initial development of the laser in 1960 by Theodore Maiman, it was not long before the potential for coherent radiation generation by non-linear optical processes was realised [27]. While many non-linear optical effects were discovered in the late 19th and early 20th centuries, it was not until the development of the laser that suitably high intensity, coherent sources which could be deployed in the laboratory allowed for investigations into the generation of coherent radiation. The first demonstration of non-linear frequency conversion of coherent radiation was by Franken et al. in 1961 [28] who published results on frequency doubling in crystal quartz. In the years after this initial demonstration, the field of non-linear optics exploded. It was not long after this that the potential for the development of highly wavelength tunable devices based on parametric generation and amplification was realised with the first demonstration of device based on this principle in 1965 [29]. However with a dearth of suitable materials, the progress in this field slowed down considerably, a situation which was only exacerbated by a shortage of suitably high-power, high spatial and temporal coherence sources. With the discovery of non-linear materials such as β-BaB_2O_4 (BBO), LiB_3O_5 (LBO) and $KTiOPO_4$ (KTP) in the 1980's with high damage thresholds and high non-linearities compared to previous materials, research into the field of parametric oscillators began once again in earnest. With further improvements in the output power, spatial and temporal coherence of available pump lasers, along with a significant reduction in component costs, parametric devices went from being demonstration of proof of principle concept devices to actual, practical sources of broadly tunable coherent radiation. The introduction of quasi-phase-matching (QPM) techniques and materials such as periodically poled lithium niobate (PPLN) improved the situation even further by allowing access to unprecedented crystal lengths, non-linear conversion coefficients and almost arbitrary phase matching wavelengths

by engineering the growth while allowing the OPOs to be pumped with well-established and now ubiquitous pump lasers – in this case diode pumped Nd:YAG and Nd:YVO_4. While this stimulated both research and device construction in the mid-IR region, the transmission range of PPLN only extends to around 4.5 μm, which is somewhat short of the chemical fingerprint region mentioned in the first chapter (~6-12 μm). The desire to develop broadly tunable devices which operate in this region for spectroscopic purposes has led to the recent development of novel semiconductor materials with transmission windows which cover this region of the spectrum such as ZGP, CdSiP, OP-GaP and OP-GaAs representing the current state of the art.

In the following sections, the basic operating principles underpinning optical parametric oscillator devices shall be presented, with particular attention being paid to intracavity and pulsed devices, which shall be implemented later in this thesis.

2.5 Basic Principles

For a dielectric medium the induced polarisation, $\vec{P}$, due to an input optical field, $\vec{E}$, is given by

$$\vec{P} = \varepsilon_0\left[\chi^{(1)}.\vec{E} + \chi^{(2)}.\vec{E}\vec{E} + \chi^{(3)}.\vec{E}\vec{E}\vec{E} + \cdots\right] \ (equation\ 2.7)$$

Where $\chi^{(n)}$ is the nth order susceptibility of the non-linear medium, with $\chi^{(1)}$ giving rise to familiar linear optical properties of a medium such as refraction, dispersion, absorption and birefringence, $\chi^{(2)}$ giving rise to 3 wave-mixing effects such as second harmonic generation, sum and difference frequency generation, the linear electro-optic (Pockels) effect as well the parametric effect, and $\chi^{(3)}$ giving rise to 4-wave mixing effects such as third harmonic generation, the non-linear electro optic (Kerr) effect, Raman scattering, phase conjugation and optical bistability. It is the second order non-linear susceptibility in particular, and the parametric effect that it gives rise to, which is of major importance to this work.

If we wish to quantify and understand the parametric effect in a non-linear medium, a solution to Maxwell's equations where the polarisation term $P^{(2)}$ is equal to $\varepsilon_0\chi^{(2)}$·EE as the polarisation source term in a dielectric medium. While the solution of such an equation is outwith the scope of this thesis, solving this for a lossless non-conducting, non-magnetic medium where the optical fields are infinite, uniform plane waves in the z-direction gives the following coupled wave equations[30].

$$\frac{dE_1(z)}{dz} = i\kappa_1 E_3(z)E_2^*(z)e^{i\Delta kz} \ (equation\ 2.8)$$

$$\frac{dE_2(z)}{dz} = i\kappa_2 E_3(z)E_1^*(z)e^{i\Delta kz} \ (equation\ 2.9)$$

$$\frac{dE_3(z)}{dz} = i\kappa_3 E_1(z)E_2(z)e^{-i\Delta kz} \ (equation\ 2.10)$$

Where E3, E1 and E2 are the pump, signal and idler waves respectively, κ_i = $[\omega_i\chi^{(2)}/2n_ic]$ with i = 1, 2, 3 and n is the refractive index. While $\Delta k=k_3-k_2-k_1$ is the phase mismatch parameter, which shall be dealt with in greater detail later. From the above equations we can see that the amplitudes of the fields of the pump, signal and idler waves are coupled to each other, hence these equations are known as the coupled wave equations. While they can be considered as a basis for many 3 wave mixing phenomena, it is the parametric effect which we shall consider, where $\omega_1 + \omega_2 = \omega_3$.

In the next section the solution to the coupled wave equations will be presented, which shall lead to a discussion of the single pass parametric gain.

2.6 Parametric Gain and Figure of Merit

In the previous section the basics of non-linear optics were presented and the coupled wave equations were introduced. While it is beyond the scope of this thesis to solve the coupled wave equations, there are several texts which make an excellent job of this [30, 31], the solution to this equation for confocally

focused beams where the interaction length is significantly longer than the confocal parameter of the beam is of interest for this thesis.

In the case of confocally focussed beams, where the interaction length is significantly longer than the confocal parameter of the beams, the solution of the coupled wave equations yields the following expression for the gain factor, Γ [30]

$$\Gamma^2 = \frac{16\pi^2 d_{eff}^2}{c\varepsilon_0 n_0 n_3 \lambda_0^3}(1-\delta^2)\hbar_m(B,\xi)\frac{\pi w_3^2}{l} I_3(0) \ (equation\ 2.11)$$

Where $d^2_{eff} = \chi^{(2)}_{eff}/2$ is the effective nonlinear coupling coefficient, ε_0 is the free-space permittivity, $n_0 \sim n_1 \sim n_2$ is the signal and idler refractive index, assuming they are approximately equal and n_3 is the pump refractive index, λ_0 is the degenerate wavelength $2\lambda_0 = \lambda_3$, δ is the degeneracy factor defined such that $1+\delta = \lambda_0/\lambda_2$ and $1-\delta = \lambda_0/\lambda_1$, $\hbar_m(B,\xi)$ is the gain reduction factor which depends on the double refraction parameter B as well as the focussing parameter $\xi = l/b$ where l is the nonlinear crystal length and w_3 is the beam waist of the pump beam[30]. From equation 2.11 it can be seen that there are a number of experimental parameters which one can design for to optimise the gain. However, there are also a selection of parameters which are innate properties of the nonlinear crystal implemented in the experiment. This gives rise to the figure of merit for a nonlinear crystal which is defined,

$$FOM = \frac{d_{eff}^2}{n^3} \ (equation\ 2.12)$$

Where $n^3 = n_1 n_2 n_3$. From equation 2.12 one can deduce that an ever increasing nonlinear coupling coefficient does not necessarily result in an increase in parametric gain, it is also modulated by increasing refractive index. This is particularly important in the case of semiconductor materials such as OP-GaAs where the large d_{eff} (94 pm/V, 60 pm/V when the $2/\pi$ factor for quasi-phase-matching is taken into account [32]) is counterbalanced by the large refractive index ($n \sim 3.3$) which results in a FOM which is only a factor of ~4 greater than PPLN despite its much lower d_{eff} (17 pm/V, $n \sim 2.3$).

By re-examining the coupled wave equations 2.8-2.10 from section 2.5 it can be seen that the transfer of energy from the pump to the signal and idler waves isn't just dependent on the nonlinear coupling between them, but also on the phase mismatch parameter Δk. In the next section the importance of this term, and the strategies, methods and techniques by which one can minimise its impact on the parametric gain in a device, a process known as known as phase matching, shall be discussed.

2.7 Phase Matching

In the previous section of this thesis, the solution of the coupled wave equations was presented with regards to the parametric gain for confocally focussed beams in a nonlinear crystal. However, by referring back to the coupled wave equations, it can be seen that the conversion from the pump field into the signal and idler fields also depends on the phase mismatch between the three fields in the crystal. It is this dependence and strategies for minimizing its impact that will be discussed in this section.

Assuming that the pump field isn't strongly depleted when passing through the nonlinear medium and that the signal and idler fields initially have zero intensity, the solution of the coupled wave equations can be cast in the following form,

$$G_2(l) = \frac{I_2(z=l)}{I_2(z=0)} - 1 = \Gamma^2 l^2 \frac{\sinh^2\left[\Gamma^2 l^2 - \left(\frac{\Delta k l}{2}\right)^2\right]^{\frac{1}{2}}}{\left[\Gamma^2 l^2 - \left(\frac{\Delta k l}{2}\right)^2\right]} \quad (equation\ 2.13)$$

Where $G_2(l)$ is the single pass signal gain when passing through the crystal. For the small gain case, where $\Gamma^2 l^2 << (\Delta k l/2)^2$, we can recast equation 2.13 such that,

$$G_2^{ss} \cong \Gamma^2 l^2 \left[\frac{\sin(\Delta k l/2)}{(\Delta k l/2)}\right]^2 \quad (equation\ 2.14)$$

Which displays a $sinc^2$ dependence on $\Delta k l/2$. The physical meaning behind the phase mismatch factor, Δk, is that it represents the extent of phase velocity

mismatch between the pump, signal and idler waves as they propagate through the nonlinear medium. In the vast majority of cases, the phase velocities of the three waves will be different such that, eventually, the fields move out of phase with each other and interfere destructively, leading to the signal and idler fields being back converted into pump field. Eventually all of the signal and idler fields are back converted into pump and the process begins anew – the distance over which all this occurs is twice the coherence length. For practical OPO systems, the nonlinear crystals are typically many coherence lengths long, and as such a way must be found to keep the signal and idler waves generated in phase with the pump – a process known as phase matching. In more traditional nonlinear materials, which were almost always either uni- or bi-axial, phase matching was achieved by using the multiple refractive indices within the material to find directions of propagation, and different polarization states of the pump, signal and idler waves, within the crystal such that the phase velocities of all three waves were equal. While this method proved effective and allowed for efficient nonlinear frequency conversion within these materials, this meant that researchers and engineers were limited to producing parametric devices from non-isotropic crystals and were forced to use the nonlinearities where phase matching angles were available, which were perhaps not always the largest nonlinearities available within the material.

One alternative method of achieving phase-matching in a nonlinear crystal is to use a process called quasi-phase matching, which shall be discussed in greater detail in the next section.

2.8 Quasi-Phase Matching

In the previous section the effects of phase mismatch on parametric gain within nonlinear crystals was discussed, along with a brief discussion of the traditional techniques used in phase matching. In this section, a more detailed description of the method of quasi-phase matching will discussed along with the benefits and drawbacks that it offers.

As stated in the previous section, when allowed to propagate freely through a non-linear medium, the pump, signal and idler waves at first travel in phase and energy is extracted from the pump to the signal and idler waves. Eventually, due to differing phase velocities, they move out of phase and the generated signal and idler interferes destructively with the signal and idler waves in the medium, leading to back conversion of the signal and idler waves into the pump. The distance over which conversion of pump to signal and idler occurs is known as the coherence length (l_c). In the pioneering work of Armstrong et al [33], it was first suggested that, by flipping the sign of the non-linearity within the medium at the point where back conversion to the pump from the signal and idler would begin, energy would instead continue to be extracted from the pump into the signal and idler. By alternating the sign of the nonlinearity every coherence length, it is possible to maintain a constant transfer of energy from the pump to the signal and idler fields throughout the full length of the crystal. This is the essence of quasi-phase matching. A diagram of how the nonlinear domains within the crystal would line up is shown in figure 2.5.

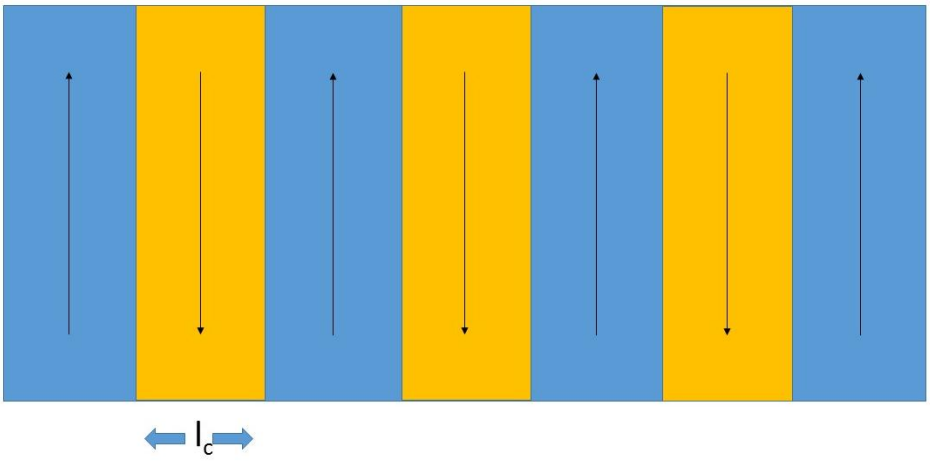

Figure 2.3 Diagram representing how the domain of the nonlinearity would be reversed in a nonlinear crystal in quasi-phase matching. Here l_c denotes one coherence length of the material.

Quasi-phase matching techniques offer several advantages over traditional phase matching techniques. By removing the reliance upon birefringence to achieve phase matching, it is possible to select an arbitrary direction for propagation through the crystal, which allows the experimentalist or engineer to access the

largest nonlinearities within the crystal, as well as being able to access the nonlinearities within isotropic materials. The avoidance of birefringent phase matching also means that the Poynting vectors of all of the waves are in the same direction, preventing walk-off of the pump, signal and idler waves. Provided that growth techniques for the chosen non-linear material are suitably mature, it is also possible to have the crystal phase match successfully anywhere within the transparency range of the crystal, broadening the available wavelength operating range.

Quasi-phase matching also has some disadvantages compared to traditional birefringent phase matching techniques. The materials used in quasi-phase matching often have relatively low damage thresholds, precluding their use in high-power devices. One other key disadvantage of quasi-phase matching is that, since the phase velocities of the waves are not always equally in sync, the transfer of energy between the pump and the signal and idler waves is not always 100 % efficient leading to a factor of $2/\pi$ in the effective nonlinear coefficient – however it should be noted that the conversion efficiency is often still higher than the birefringent phase-matched equivalent due to the ability of quasi-phase-matched materials to access the highest nonlinear coefficient of the material. This is demonstrated in figure 2.6 shown below.

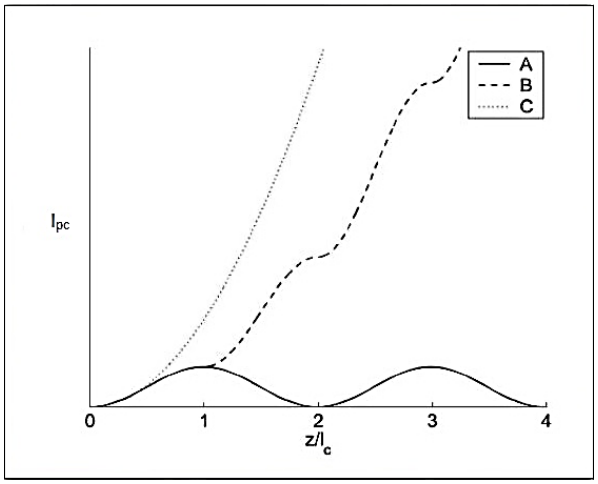

Figure 2.4 A diagram showing the downconverted intensity with respect to the distance, z, propagated through a nonlinear crystal. The light solid line represents a perfectly phasematched system, the dashed line a quasi-phase-matched one while the dark solid line represents what would occur with no phase matching present, with energy transferring between the downconverted waves and the pump over multiple coherence lengths.

In this section we have explored quasi-phase matching processes including their advantages and disadvantages over traditional birefringent techniques. In the next section one of the important consequences of group velocity mismatch in nonlinear crystals shall be explored – the phase matching bandwidth.

2.9 Phase Matching Bandwidth in Nonlinear Crystals

In the previous section the process of quasi-phase matching and some of its advantages and disadvantages compared with more traditional phase matching techniques were presented. In this section we shall look at how the group velocity mismatch affects the conversion of the pump into signal and idler, by examining the linewidth over which the pump is effectively converted into signal and idler – the phase-matching bandwidth.

In the previous sections, only waves which are exactly phase-matched with each other such that $\Delta k = 0$, which is where the maximum parametric gain would be found, were considered. However, one is highly unlikely to encounter a pump laser beam in a practical context which exhibits a linewidth which is an exact delta function, the pump will inevitably have some finite linewidth of some degree. It is of interest to both the experimentalist and device builder to ascertain how much of the laser linewidth contributes usefully to parametric gain to avoid wasting pump power and improve device efficiency.

From equation 2.14 it can be seen that not all solutions such that $\Delta k \neq 0$ result in insignificant parametric gain. Indeed, so long as the pump, signal and idler do not drift into antiphase over the length of the crystal ($\Delta k = \pi$) there will be some useful contribution from the pump into the signal and idler. By varying the signal and idler frequencies while holding the pump constant, the phase mismatch varies such that

$$\frac{\partial}{\partial \omega_p}\Delta k = \frac{\partial k_p}{\partial \omega_p} + \frac{\partial k_s}{\partial \omega_s} - \frac{\partial k_i}{\partial \omega_i} = \frac{1}{v_{g,p}} + \frac{1}{v_{g,s}} - \frac{1}{v_{g,i}} \quad (equation\ 2.15)$$

Where $v_{g,p}$, $v_{g,s}$ and $v_{g,i}$ are the pump, signal and idler group velocities. The signal and idler terms arise in this equation from the automatic adjustment of the signal

and idler wavelengths with the pump wavelength due to conservation of energy and momentum. The phase-matching bandwidth of a parametric device is usually defined as the bandwidth in which the accumulated phase mismatch varies by less the 2.7831rad, which corresponds to the half width of the conversion efficiency curve. For a crystal of length L, the phase matching bandwidth may be defined as,

$$\Delta\omega_p = \frac{2.7831}{\left|\frac{1}{v_{g,p}} + \frac{1}{v_{g,i}} - \frac{1}{v_{g,s}}\right| L} \quad (equation\ 2.16)$$

From equation 2.16 it can be seen that the larger the variation in the group velocities within the material, the narrower the acceptance bandwidth. Likewise, the longer the crystal is, the narrower the bandwidth of the pump which is usefully converted into signal and idler. For practical intracavity optical parametric oscillators, where long interaction lengths are necessary due to the small parametric gains which are often encountered (more on this later), this can result in narrow acceptance bandwidths which can be problematic in efficient device construction.

Now, after examining the phase matching bandwidth this chapter finishes by dealing with the effects associated in general with the parametric effect. From this point forward only the intricacies of optical parametric oscillators shall be considered, beginning with the threshold and conversion efficiency in an optical parametric oscillator.

2.10 Threshold and Conversion Efficiency in Singly Resonant Optical Parametric Oscillators

In the previous sections basic principles of parametric processes which are of interest to this thesis were explored. In the following sections we are going to look at specific processes of import within singly resonant optical parametric oscillators. Singly resonant optical parametric oscillators were chosen as the focus of this thesis, and the underpinning OPO configuration for all of the devices

constructed within this research, due to the simplicity of their realisation and the wide tunability offered by removing any constraints on the idler wavelength, other than those imposed by phase matching with the pump and signal frequencies. This allows for simplified tuning of an optical parametric oscillator compared with doubly resonant OPOs, which is desirable in a potential spectroscopic device.

In this section we shall first deal with the threshold in a continuous-wave, singly-resonant optical parametric oscillator, which is the simplest case that one can consider, along with the conversion efficiency in such devices.

For the sake of simplicity when evolving the equations required to model the threshold in an optical parametric oscillator, the following assumptions are made - (1) that the pump, signal and idler are always plane waves, (2) there shall only be a single pass of the pump through the nonlinear crystal so that downconversion need only be considered in the forward direction in the crystal, (3) the interaction is phase matched and (4) that there is negligible depletion of the pump through the nonlinear crystal (which is appropriate at threshold). This allows the coupled wave equation (see section 2.5) for the pump to be disregarded as the pump is not varying throughout the crystal, leaving only the signal and idler equations to be considered.

For a singly resonant OPO one can make a number of further assumptions. It is assumed that only one of the waves is resonated and that it is always the signal, with the idler wave leaving after a single pass. Since the pump is only propagating through the crystal in the forward direction, we can assume that parametric gain only occurs in the forward direction and finally we assume that the losses for the signal wave are small and that the signal wave field is constant throughout the medium at a first approximation. This reduces the coupled wave equation for the idler wave (equation 2.10) to,

$$\frac{dE_1}{dz} = \left[\frac{id_{eff}\omega_1}{cn_1}\right] E_3 E_2^* \ (equation\ 2.17)$$

All of the above implies that the idler wave grows linearly throughout the nonlinear medium at a constant rate according to the following expression.

$$E_1(z) = i\kappa_1 E_3 E_2^* z \ (equation\ 2.18)$$

Which can then be substituted into the coupled wave equation for the signal (equation 2.9) and with some recasting gives the following expression for the fractional round trip gain in signal intensity,

$$\frac{\delta I_2}{I_2} = \frac{2Z_0\kappa_2\kappa_1 l^2 I_3}{n_3} \ (equation\ 2.19)$$

Where I_2 is the signal intensity, I_3 the pump intensity and $Z_0 = (\mu_0/\varepsilon_0)^{1/2}$. The threshold operating condition is found by setting the above expression for the fractional round trip gain equal to the round trip signal loss, α_2, and with some suitable substitutions gives,

$$I_{th} = \frac{\varepsilon_0 n_3 n_2 n_1 \lambda_1 \lambda_2 \alpha_2}{8\pi^2 l^2 d_{eff}} \ (equation\ 2.20)$$

Where I_{th} is the threshold pump intensity required to achieve OPO operation.

Another factor which it is important to consider when designing an optical parametric device is the pump intensity above threshold for which the most efficient extraction of the pump light takes place. With foreknowledge of this, the experimentalist or engineer can design an OPO to perform at the maximum efficiency for a specified operating pump intensity.

For a singly resonant OPO the input pump intensity for which there is complete extraction of the pump, and thus the most efficient generation, is defined by the following expression,

$$I_{in} = \left(\frac{\pi}{2}\right)^2 I_{th} = 2.47 I_{th} \ (equation\ 2.21)$$

Where I_{in} is the input intensity. From the above expression it can be seen that, for optimum extraction of pump through to signal and idler, one should ideally

design an OPO such that the operating pump intensity is 2.47x larger than the threshold of the OPO.

In this section we have looked at the threshold and optimum operating conditions in a traditional singly resonant optical parametric oscillator cavity. In the next section, intracavity optical parametric oscillators shall be introduced and their advantages, disadvantages and key characteristics presented and discussed.

2.11 Intracavity Optical Parametric Oscillators.

In the previous section the threshold and optimum operating conditions for a traditional singly resonant optical parametric oscillator were presented. However, practical implementation of these devices is often rendered difficult or inefficient near threshold due to the high pump powers that are required to achieve threshold. One way to circumvent this limitation is to place the OPO within the laser cavity, taking advantage of the field enhancement within the cavity to access higher powers without having to resort to higher primary pump powers for the laser. This makes reaching threshold for the OPO much easier to achieve. In this section the important characteristics and the advantages and disadvantages conferred by operating an OPO in the intracavity regime shall be discussed.

The first thing which must be considered when introducing an OPO into the laser cavity is the effect which this has upon the intracavity field of the pump laser itself. It can be determined that there are in fact three clear operating regimes of the pump laser when an OPO is brought to threshold within the laser cavity, which are shown in figure 2.7.

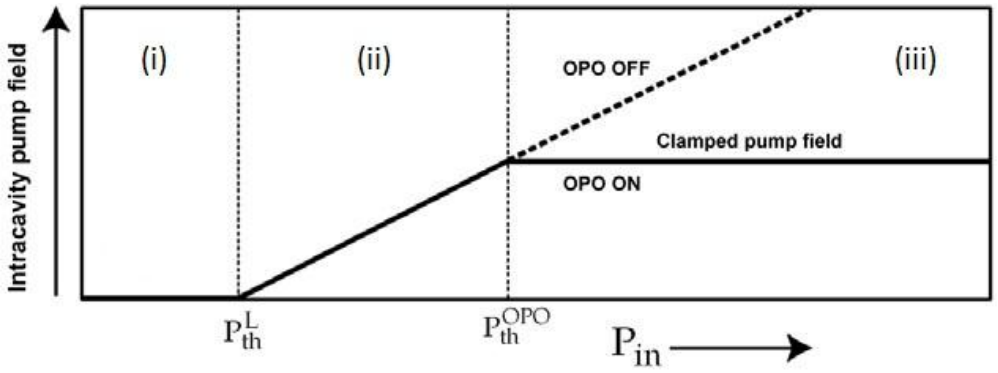

Figure 2.7 The three distinct operating regimes for the intracavity field of a laser with an OPO internal to the laser cavity. In the first section, the pump power to the laser is insufficient to bring the laser to threshold, and no intracavity field builds up. In the second section, sufficient pump power has been supplied to the laser to achieve threshold, and the intracavity field begins to build up with increasing pump power. It is in the third section that the behaviour of the intracavity field deviates from the norm. Under normal circumstances the intracavity field would simply increase linearly with increasing pump power, as shown by the dashed line in the above figure. However, once the OPO is brought to threshold the intracavity field of the laser becomes clamped, as any increase in the intracavity field is downconverted within the cavity by the OPO. Figure courtesy of [34].

The first operating regime is where there is insufficient pump power to bring the laser itself to threshold, which is shown by the first section in figure 2.7(i). The second operating regime, shown by the second section in figure 2.7(ii) is where there is sufficient pump power to bring the laser to threshold but not the OPO. In this regime the intracavity field increases linearly as one would expect with a traditional laser cavity. It is the third operating regime, shown in figure 2.7(iii), where the OPO comes to threshold and traditional laser behaviour is no longer applicable. In a normal laser cavity, the intracavity field would continue to increase linearly with increasing pump field, which is shown by the dotted line in the above figure. However, when the OPO placed internal to the laser cavity reaches threshold, the intracavity field is clamped, in a manner analogous to the upper-state population within a laser once a laser cavity reaches threshold. This is due to the increasing nonlinear losses introduced by the OPO with increasing OPO pump intensity. The additional intracavity power introduced by increasing the pump power for the laser is simply downconverted by the OPO, clamping the intracavity field to the power required to bring the OPO to threshold.

After the effect on the pump laser, the next thing which must be given consideration is the effect upon the OPO that placing it internal to the laser cavity has upon the OPO threshold. It is more convenient to recast the following

equation into threshold intracavity power rather than intensity. The pump also now makes two passes of the nonlinear crystal on a round trip, rather than just one as in the traditional OPO model. Taking these things into account the threshold intracavity power for an intracavity OPO is defined as [30, 34],

$$P_{th} = \frac{\varepsilon_0 n_3 n_2 n_1 \lambda_1 \lambda_2 \pi (\varphi_3^2 + \varphi_2^2) \alpha_2}{16\pi^2 l^2 d_{eff}} \ (equation\ 2.22)$$

Where P_{th} is the threshold intracavity power for OPO operation and $\varphi_3 + \varphi_2$ are the confocally focussed pump and signal mode radii within the nonlinear crystal and are defined such that,

$$\varphi_i = \sqrt{\frac{\lambda_i l}{2\pi}} \ (equation\ 2.23)$$

It should be noted that in equation 2.22 above that there is a factor of 2 reduction in the threshold condition from the traditional singly resonant optical parametric oscillator (SROPO) configuration due to having two passes of the nonlinear crystal on a round trip. This reduces the threshold power requirements even further, tipping the balance further in the intracavity OPOs favour over the traditional SROPO when the desire is for low primary pump power threshold.

The final alteration in the OPO characteristics which shall be considered in this section is the ideal operating conditions of the OPO. In the previous section, optimum downconversion was described as the condition where all of the pump field was depleted and downconverted into signal and idler. For an intracavity OPO it is clear that such conditions would not be the optimal for the laser – if the loss within the laser cavity is so great that the intracavity field is reduced to zero, the pump laser would cease to oscillate. Instead, it is reasonable to conclude that, since the OPO is acting to output couple the intracavity field, the optimum operating condition for the OPO should be where the nonlinear loss introduced by the OPO would be the same as the optimal output coupling for the host laser at that particular pump level [34] . This results in an optimal operating regime such that,

$$P_{th}^{OPO} = \sqrt{P_{th}^{L}.P_{in}}\ (equation\ 2.24)$$

Where P_{in} is the primary pumping power for the laser, the power of the pump laser for the host laser, not the OPO, at which the device is to be optimised. P_{th}^{L} is the threshold of the host laser and P_{th}^{OPO} is the intracavity threshold pump power of the OPO. For a further treatment of the above expression, see the work of Colville, Dunn et al. (1997) [35].

In this section we have so far looked at the threshold condition and optimisation of an intracavity OPO. However, the one thing we are yet to consider is the alteration to the transient dynamics of the pump laser with the introduction on an OPO into the laser cavity. While introducing the OPO into the laser cavity offers strong advantages with regards to reducing the threshold primary pump power requirements, in the next section it shall be shown that this has a detrimental effect on the transient stability of the pump laser, and thus upon the OPO itself, in a continuous wave device.

2.12 Relaxation Oscillations in an Intracavity OPO

In the previous section the impact upon the intracavity field magnitude, the OPO threshold and the optimum operating condition for the device were discussed. In the following section the effect of the introduction of an OPO to the laser cavity on the transient dynamics of the system, in particular the relaxation oscillations of the laser and its implications, shall be discussed.

In a traditional dielectric solid-state laser oscillator the phenomena of relaxation oscillations arise from the interaction between the upper state population and the photon flux within the cavity. Any disturbance in one leads to an interaction between the two, due to the gain dynamics in a solid-state laser where the levels fluctuate until they are damped by the system and vary in frequency according to the following proportion.

$$\omega_{osc} \propto \sqrt{\frac{1}{\tau_u \tau_p}} \ (equation\ 2.25)$$

Where ω_{osc} is the angular frequency of the relaxation oscillations and τ_u and τ_p are the upper state lifetime and the laser cavity photon lifetime. Usually the relaxation oscillations are damped by spontaneous emission from the gain medium. The rate at which damping occurs is inversely proportional the upper-state lifetime of the gain medium. If the upper-state lifetime of the gain medium is short enough compared to the oscillation frequency of the cavity, then it critically damps any relaxation oscillations in the laser.

For the case of an optical parametric oscillator internal to a laser cavity, this is no longer the case. With the inclusion of the OPO, the intracavity laser (henceforth pump) photon flux also interacts with the signal photon flux in the signal cavity. The many component nature of this interaction leads to prolonged and chaotic relaxation oscillations. In addition to this, the shift of the dynamic from upper state laser population → pump photon flux → signal photon flux also changes the dependence to the of the frequency of the relaxation oscillations to the following,

$$\omega_{osc} \propto \sqrt{\frac{1}{\tau_p \tau_s}} \ (equation\ 2.26)$$

With the upper state lifetime dependence now being replaced with a dependence on the signal photon cavity lifetime, τ_s [36, 37]. Therefore the upper state lifetime must now be of a similar order of magnitude to the signal cavity photon lifetime for the laser to upper-state population to be able to respond fast enough for the laser to be able to critically damp any oscillations. In practice this requires the upper-state lifetime of the gain medium to be on the order of nanoseconds, which makes the construction of amplitude stable ICOPOs difficult to achieve in practice using many traditional solid-state gain media such as Nd, Tm etc.

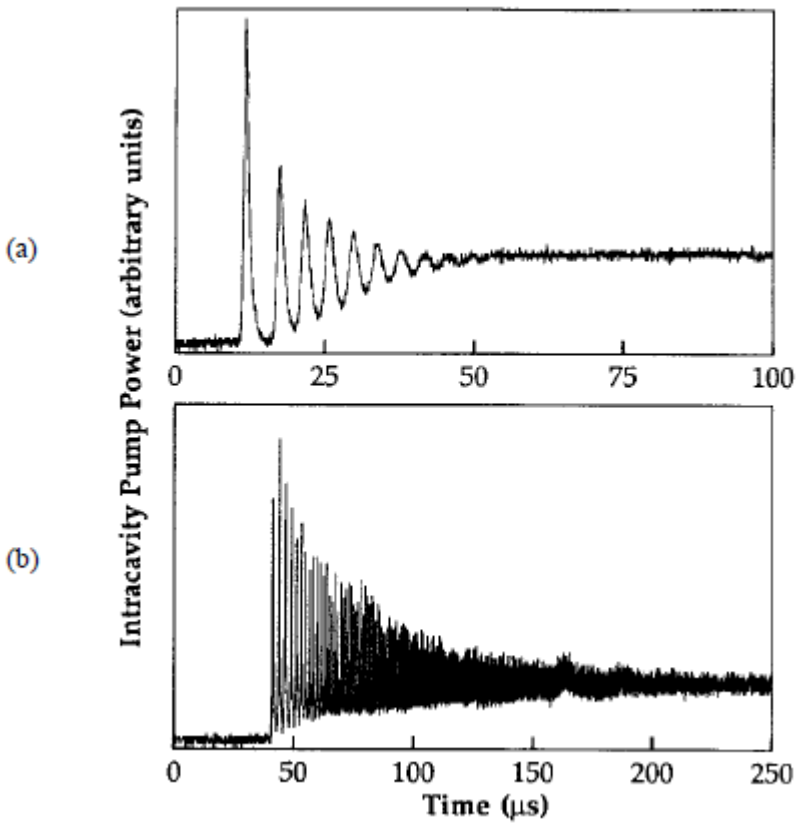

Figure 2.8 The transient dynamics of the pump field in a Nd:YVO4 pumped OPO in a) the absence of and b) the presence of parametric downconversion. Image courtesy of [37]

In this section, the effects on the transient dynamics of adding an OPO internal to a laser cavity have been presented and discussed. One possible method of ameliorating the negative effects on the transient dynamics and indeed of controlling them, is to pulse the pump laser. In the next section pulsed intracavity OPOs, in particular the operating thresholds of such devices, shall be discussed.

2.13 Pulsed Optical Parametric Oscillators

In the previous sections intracavity OPOs were discussed in terms of their threshold characteristics and temporal dynamics. While it can be shown that the ICOPO offers many advantages with regards to improving the threshold characteristics compared to traditional OPO schemes, it can be detrimental to the amplitude noise in such devices by exacerbating the relaxation oscillations within

the cavity. One way of circumventing this problem is by controlling the temporal dynamics of the device by pulsing the pump laser. In this section some of the dynamics and the threshold conditions for a pulsed OPO device shall be presented and discussed.

Pulsed OPO devices are in fact the most studied and most common parametric devices in both industry and research. With their high peak powers and the widespread availability of good quality lasers, pulsed OPOs were actually the first OPO devices to be demonstrated – a $LiNbO_3$ OPO pumped by a nanosecond, frequency doubled, Q-switched Nd:$CaWO_4$ laser at 529 nm in 1965 [38]. It is nanosecond pulsed OPOs which shall be focussed on in particular in this section, where the pulses are produced by Q-switching of the pump laser, due to the simplicity of their implementation using mature modulator technologies such as acousto-optic Q-switches and Pockel's cells.

The basic operation principles are the same for both nanosecond pulsed OPOs and cw-OPO devices. However, the steady-state analysis used in deriving the threshold conditions in a traditional cw-OPO are no longer valid as the near-instantaneous nature of parametric gain does not allow for steady-state conditions to be reached within the timeframe of the pump pulse. This can be contrasted with the more established pulsed-pumped solid-state laser case, where the long upper-state lifetimes of solid-state gain media allows for energy storage between pulses and allows for amplification of the generated pulse beyond the duration of the pump pulse. In a pulsed OPO, the immediate transfer of energy from the pump pulse to the signal pulse means that there is no energy stored within the nonlinear medium, requiring that the signal pulse is only amplified during the duration of the pump pulse. From a pragmatic perspective, if one wishes to achieve the maximum gain within a pulsed OPO, the signal pulse must resonate through the nonlinear crystal as many times as possible within the duration of the pump pulse. This is most easily achieved by decreasing the signal cavity length to increase the number of round trips of the signal within the finite duration of the pulse. From the previous qualitative analysis in this section, it becomes clear that the rise time of the signal pulse has a strong effect on how

much gain can be extracted from the pump pulse, with the rise time of the optical parametric oscillator acting as an effective loss mechanism for the signal pulse. Decreasing the signal cavity length also decreases the rise time of the oscillator, which provides a simple way to ameliorate this issue. It should be noted however that, as the mirrors of the cavity in an ICOPO are highly reflecting for the pump pulse, the leakage of the pump field is negligible during the signal field build-up in comparison to the extra-cavity OPO case. This allows for all of the energy of the pump field to be available to the signal field, leading to the total depletion of the pump pulse within the laser cavity through the parametric process once the OPO reaches threshold [39].

A quantitative time-dependent gain analysis of the equations governing the threshold fluence in pulsed SROPOs was published by Brosnan and Byer in 1979 [40], the evolution of which is beyond the scope of this thesis. The model assumes a Gaussian temporal profile for the pump pulse, and a Gaussian spatial distribution for both the pump and signal pulses, with the idler being entirely unconstrained within the cavity. By defining threshold as a signal energy of ~100 μJ corresponding to a signal power to parametric noise power, $\ln(P^{th}_s/P_n) = 33$ the threshold energy fluence is given by,

$$J_{th} \cong \frac{2.25}{\gamma g_s \zeta}\tau\left[\frac{L}{2\tau c}\ln\frac{P_s^{th}}{P_n} + 2\alpha l + \ln\frac{1}{\sqrt{R}} + \ln 2\right]^2 \ (equation\ 2.27)$$

Where τ is the $1/e^2$ half-width intensity of the pump pulse, L is the cavity length, α is the signal loss within the crystal, R is the mirror reflectivity and l is the crystal length. γ is the modified gain coefficient defined as,

$$\gamma = \frac{2\omega_2\omega_1 d_{eff}^2}{n_3 n_2 n_1 \varepsilon_0 c^3} \ (equation\ 2.28)$$

The factor g_s is the spatial coupling coefficient describing the mode matching between the pump and signal pulses and is defined as,

$$g_s = \frac{w_3^2}{w_3^2 + w_2^2} \ (equation\ 2.29)$$

The parameter ζ is the effective parametric gain length of the crystal. For the quasi-phase matched, isotropic OP-GaAs crystals implemented in this thesis, there is no need to consider walk-off due to differing Poynting vectors as all three of the pump, signal and idler waves are aligned and thus the effective parametric gain length becomes the length of the crystal.

2.14 Conclusions

In this chapter the principles underpinning semiconductor disk lasers and optical parametric oscillators and their impact on experimental design parameters have been discussed. It has been shown that the design considerations for an SDL are important for optimal engineering of the gain medium. It is necessary to select the material system such that the band gap of the quantum wells is in the region in which one would like the SDL to operate, while the materials which must then be used for the other segments of the gain chip should also be latticed match to the quantum well material in the active region to prevent propagation of defects in or structural failure of the material. By designing the SDL chip such that the pump is absorbed in the barrier regions and laser operation occurs in the quantum wells (active region) it is possible to optimise the absorption and emission properties of the SDL chip separately, which can allow for optimal engineering of the chip for the applications which one has in mind. The low gain offered by the few quantum well structures in an SDL requires that there are very few losses within the laser cavity itself. This problem is often ameliorated by the growth of a high-reflectivity Bragg mirror on the rear surface of the chip. However, one must keep in mind that by adding more and more layers to the Bragg stack to achieve a higher reflectivity, one is also creating a larger and larger thermal impedance between the rear-surface of the chip and any heatsinking which the chip is contacted to. This requires that improved thermal management techniques are implemented to manage heat extraction from the device. There are two schemes which are proven to be highly effective and which are now mature methods of heat extraction for SDL gain media – removal of the substrate and the use of a transparent intracavity heatspreader. While removing the

substrate is effective for GaAs based material systems due to the low thermal impedance offered by the Bragg mirror on the chip, the GaSb material system used in 2μm material demands that an intracavity heatspreader is used instead due to the high thermal barrier which the DBR materials used in this system provide.

When it comes to designing an intracavity OPO, the following parameters must be considered. The nonlinear material which one selects must be transparent (lossless) at both the pump, signal and idler frequencies. The next thing to consider is the figure of merit of the material – this figure gives a measure at a glance of the potential conversion efficiency which the material offers and is given by the ratio of the effective nonlinear coefficient squared to the triple product of the refractive indices. The next consideration is whether the material can be phase-matched for the relevant pump, signal and idler frequencies which one wishes to use and whether it is necessary to quasi-phase-match the material or not. It should be noted that it can often be advantageous to make use of quasi-phase-matching as this allows access to the highest nonlinearities within the material, something which more established birefringent phase-matching techniques may not. The phase-matching bandwidth of the nonlinear medium should also be considered, and the pump laser engineered such that the linewidth of the laser is narrower than the phase-matching bandwidth of the nonlinear material. It is also important to consider what the operational output power of the device should be, as an OPO operates at optimal efficiency at ~2.47x over threshold and thus the OPO should be engineered with this in mind. Finally, when dealing with intracavity OPO devices, there are two other important things which must be accounted for – possible extreme and prolonged relaxation oscillations in cw-OPOs and the short time interval where parametric gain is possible in a pulsed OPO. The prolonged relaxation oscillations in a cw-intracavity OPO can be dealt with by selecting a gain medium with an upper state lifetime on the order of the cavity photon lifetime, which tends to be on the order of nanoseconds. The parametric gain in a pulsed OPO can be maximised by increasing the number of passes which the signal makes through the nonlinear crystal while the pump

pulse is propagating within the cavity as well as by reducing the rise time of the signal field within the OPO.

In the following chapter the experimental development of a Tm:YAG pumped pulsed intracavity singly-resonant optical parametric oscillator based on orientation-patterned gallium arsenide shall be presented and its operational characteristics discussed.

2.15 References

1. Kuznetsov, M., et al., *High-power (>0.5 W CW) Diode-pumped Vertical-external-cavity Surface-emitting Semiconductor Lasers with Circular TEM_{00} Beams.* IEEE Photonics Technology Letters, 1997. **9**(8): p. 1063-1065.
2. Kuznetsov, M., et al., *Design and Characteristics of High-power (>0.5 W CW) Diode-pumped Vertical-external-cavity Surface-emitting Semiconductor Lasers with Circular TEM_{00} Beams.* IEEE Journal of Selected Topics in Quantum Electronics, 1999. **5**(3): p. 561-573.
3. Stillman, G.E., et al., *Volume Excitation of an Ultrathin Single-mode CdSe Laser.* Applied Physics Letters, 1966. **9**(7): p. 268-269.
4. *Semiconductor Disk Lasers: Physics and Technology*. 2010: John Wiley and Sons.
5. Svelto, O., *Principles of Lasers*. 2010: Springer.
6. Webb, S.H.a.C., *Laser Physics*. Oxford Master Series in Atomic, Optical and Laser Physics. 2010, U.K.: Oxford University Press.
7. Tropper, A.C., et al., *Vertical-external-cavity Semiconductor Lasers.* Journal of Physics D: Applied Physics, 2004. **37**(9): p. R75.
8. Giesen, A., et al., *Scalable Concept for Diode-pumped High-power Solid-state Lasers.* Applied Physics B, 1994. **58**(5): p. 365-372.
9. Giesen, A. and J. Speiser, *Fifteen Years of Work on Thin-Disk Lasers: Results and Scaling Laws.* IEEE Journal of Selected Topics in Quantum Electronics, 2007. **13**(3): p. 598-609.
10. Härkönen, A., et al., *High Power Frequency Doubled GaInNAs Semiconductor Disk Laser Emitting at 615 nm.* Optics Express, 2007. **15**(6): p. 3224-3229.
11. Hopkins, J.M., et al., *Tunable, Single-frequency, Diode-pumped 2.3μm VECSEL.* Optics Express, 2007. **15**(13): p. 8212-8217.
12. Maclean, A.J., et al., *Continuous Tuning and Efficient Intracavity Second-Harmonic Generation in a Semiconductor Disk Laser With an Intracavity Diamond Heatspreader.* IEEE Journal of Quantum Electronics, 2008. **44**(3): p. 216-225.
13. Raymond, T.D., et al., *Intracavity Frequency Doubling of a Diode-pumped External-cavity Surface-emitting Semiconductor Laser.* Optics Letters, 1999. **24**(16): p. 1127-1129.
14. Hopkins, J.M., et al., *High-power, (AlGaIn)(AsSb) Semiconductor Disk Laser at 2.0 μm.* Optics Letters, 2008. **33**(2): p. 201-203.

15. Konttinen, J., et al., *High-power (>1 W) Dilute Nitride Semiconductor Disk Laser Emitting at 1240 nm.* New Journal of Physics, 2007. **9**(5): p. 140.
16. Smith, S.A., et al. *A 0.6W CW GaInNAs Vertical External-cavity Surface-emitting Laser Operating at 1.32μm*. in *Conference on Lasers and Electro-Optics/International Quantum Electronics Conference and Photonic Applications Systems Technologies*. 2004. San Francisco, California: Optical Society of America.
17. Bennett, B.R., et al., *Antimonide-based Compound Semiconductors for Electronic Devices: A Review.* Solid-State Electronics, 2005. **49**(12): p. 1875-1895.
18. Maclean, A.J., et al., *Limits on Efficiency and Power Scaling in Semiconductor Disk Lasers with Diamond Heatspreaders.* Journal of the Optical Society of America B, 2009. **26**(12): p. 2228-2236.
19. Holms, M.A., et al., *Actively Stabilized Single-frequency Vertical-external-cavity AlGaAs Laser.* IEEE Photonics Technology Letters, 1999. **11**(12): p. 1551-1553.
20. Heinen, B., et al., *106 W Continuous-wave Output Power from Vertical-external-cavity surface-emitting Laser.* Electronics Letters, 2012. **48**(9): p. 516-517.
21. Heinen, B., et al., *106 W Continuous-wave Output Power from Vertical-external-cavity surface-emitting Laser.* Electronics Letters, 2012. **48**(9): p. 516-517.
22. Kemp, A.J., et al., *Thermal Management in 2.3 μm Semiconductor Disk Lasers: a Finite Element Analysis.* IEEE Journal of Quantum Electronics, 2008. **44**(2): p. 125-135.
23. Holl, P., et al., *Recent Advances in Power Scaling of GaSb-based Semiconductor Disk Lasers.* 2015.
24. Rantamäki, A., et al., *3 W of 650 nm Red Emission by Frequency Doubling of Wafer-Fused Semiconductor Disk Laser.* Optics Express, 2010. **18**(21): p. 21645-21650.
25. Lyytikäinen, J., et al., *1.3μm Optically-pumped Semiconductor Disk Laser by Wafer Fusion.* Optics Express, 2009. **17**(11): p. 9047-9052.
26. Rantamäki, A., et al., *High Power Semiconductor Disk Laser with a Semiconductor-Dielectric-metal Compound Mirror.* Applied Physics Letters, 2014. **104**(10): p. 101110.
27. Maiman, T.H., *Optical and Microwave-optical Experiments in Ruby.* Physical Review Letters, 1960. **4**(11): p. 564-566.
28. Franken, P.A., et al., *Generation of Optical Harmonics.* Physical Review Letters, 1961. **7**(4): p. 118-119.
29. Giordmaine, J.A. and R.C. Miller, *Tunable Coherent Parametric Oscillation in $LiNbO_3$ at Optical Frequencies.* Physical Review Letters, 1965. **14**(24): p. 973-976.
30. Ebrahim-Zadeh, M. and M.H. Dunn, *Optical Parametric Oscillators*, in *Handbook of Optics*. 2004, McGraw-Hill.
31. Sutherland, R.L., *Handbook of Nonlinear Optics*. Second Edition ed. 2003: Marcel Dekker.

32. Vodopyanov, K.L., *Pulsed Mid-IR Optical Parametric Oscillators*, in *Solid State Mid-Infrared Laser Sources*, I.T.S.a.K.L. Vodopyanov, Editor. 2003, Springer-Verlag.
33. Armstrong, J.A., et al., *Interactions between Light Waves in a Nonlinear Dielectric.* Physical Review, 1962. **127**(6): p. 1918-1939.
34. Stothard, D.J.M., *Practical Continuous Wave Optical Parametric Oscillators*, in *Advances in Optical and Photonic Devices*, K.Y. Kim, Editor. 2010, InTech.
35. Colville, F.G., M.H. Dunn, and M. Ebrahimzadeh, *Continuous-wave, Singly Resonant, Intracavity Parametric Oscillator.* Optics Letters, 1997. **22**(2): p. 75-77.
36. Stothard, D.J. and M.H. Dunn. *Relaxation Oscillation Suppression in Intra-Cavity Optical Parametric Oscillators*. in *Conference on Lasers and Electro-Optics/International Quantum Electronics Conference*. 2009. Baltimore, Maryland: Optical Society of America.
37. Turnbull, G.A., et al., *Transient Dynamics of CW Intracavity Singly Resonant Optical Parametric Oscillators.* IEEE Journal of Quantum Electronics, 1999. **35**(11): p. 1666-1672.
38. Giordmaine, J. and R.C. Miller, *Tunable Coherent Parametric Oscillation in $LiNbO_3$ at Optical Frequencies.* Physical Review Letters, 1965. **14**(24): p. 973.
39. Debuisschert, T., et al., *Intracavity Optical Parametric Oscillator: Study of the Dynamics in Pulsed Regime.* Journal of the Optical Society of America B, 1996. **13**(7): p. 1569-1587.
40. Brosnan, S. and R.L. Byer, *Optical Parametric Oscillator Threshold and Linewidth Studies.* IEEE Journal of Quantum Electronics, 1979. **15**(6): p. 415-431.

Chapter 3
Tm^{3+}:YAP Pumped, Pulsed OPO Based on OP-GaAs

3.1 Introduction

As discussed in the introductory chapter, the transparency range of OP-GaAs, while excellent at longer wavelengths, introduces issues for the procurement and implementation of suitable pump lasers. One suitable laser for the pumping of OP-GaAs at 2 μm is Tm^{3+}:YAP. Thulium was first demonstrated as a suitable dopant for solid-state lasers in the 2 μm region in 1973 by Weber et al, but the technology of the time required the thulium rods to be co-doped with erbium for effective flash-lamp pumping, which impacted upon efficiency [1]. However, it was with the development of efficient, high-power InGaAs diodes, and their widespread commercial availability, that the potential for high power Tm^{3+}:YAP lasers was truly realised [2-4]. With the demonstration of high power and excellent beam quality lasers, such a system is now a potential pump source for non-linear optical devices [5, 6]. In this chapter, the properties of Tm^{3+}:YAP will first be outlined. The development of a Tm:YAP laser and an associated intracavity OPO system based on OP-GaAs will then be discussed and its performance characterised.

3.2 Properties of Tm^{3+}:YAP

Thulium, like many of its fellow rare-earth elements, makes an excellent choice as a laser ion. There are three common host materials into which thulium has been doped – yttrium aluminium perovskite (YAP, $YAlO_3$), yttrium aluminium garnet (YAG, $Y_3Al_5O_{12}$), and yttrium lithium fluoride (YLF, $LiYF_4$). Each of these hosts comes with their own intrinsic advantages and disadvantages which shall be discussed below.

YAG is perhaps the most common and well known of all host laser materials. Its high thermal conductivity, great mechanical strength and the high optical quality make it a popular choice with laser scientists and engineers for a wide range of dopants and applications. In particular, Nd:YAG is the most widely known and understood doped-dielectric laser today. However, YAG can be unsuitable as a high-power laser host medium due to its cubic structure – the lack of any natural birefringence provided by such a crystal configuration leaves YAG based lasers vulnerable to the effects of thermally induced birefringence [7, 8]. If polarising elements are present, this can introduce losses in the system at larger absorbed pump powers due to the introduction of birefringence in the cavity. The constraints that this provides precludes YAG as an optimal host medium for this application. Both YAP and YLF can overcome this constraint as both materials have an orthorhombic structure, which provides natural birefringence that dominates over thermally induced birefringence [7, 9-12]. In addition, YAG introduces very little broadening to the laser emission, which is good for producing narrow linewidth lasers, but often hampers the tunability of the system, such as in the case of Tm:YAG. This is another reason why YAG would be unsuitable as a pump source for a pump tuned intracavity optical parametric oscillator.

The next material which shall be discussed is YLF. While sharing the same beneficial orthorhombic structure as YAP, YLF suffers from having a lower thermal fracture limit and has polarisation dependant thermal lensing, neither of which are advantageous for high-power operation. While the polarisation dependant thermal lensing in YLF can produce a negative lens, which would compensate for bulging of the crystal faces to reduce thermal lensing, any asymmetric thermal lensing would negatively impact the mode quality [11, 12]. As a single- fundamental-spatial-mode beam is required for non-linear frequency conversion, this renders YLF an unsuitable choice for intracavity frequency conversion. This leaves YAP, which share the benefits of the other yttrium hosts but does not exhibit the major detractions of YAG or YLF, as the best available choice for intracavity frequency conversion applications.

High quality boules of Tm^{3+}:YAP are almost always grown by the Czochralski method [10, 13]. While three forms of Tm^{3+}:YAP are stable (hexagonal, cubic and orthorhombic) the orthorhombic structure, with its natural birefringence, is the most typically used structure [9, 10, 13]. As a biaxial crystal with an orthorhombic structure, YAP has three defined axes labelled a, b and c in Pnma notation (labelled b, c and a respectively in the older Pbnm notation) [5, 9, 14]. As a consequence of this anisotropy, Tm^{3+}:YAP has different absorption and emission characteristics along each axis, which are shown in figure 3.1 [5, 14]. The b-axis of Tm^{3+}:YAP shows a strong absorption peak at 795 nm. As a result, both a and c-cut Tm^{3+}:YAP possess a single strong absorption peak at this wavelength, while b-cut Tm^{3+}:YAP is known to possess a weaker double absorption peak at 793 nm and 799 nm [5, 14]. This makes a and c-cut Tm^{3+}:YAP favourable for diode pumping in preference to b-cut material as a candidate for this research. With its lower pump threshold and broader tuning range [5], which is beneficial for pump tuning of the OPO, c-cut Tm^{3+}:YAP was chosen as the laser medium for producing an intracavity optical parametric oscillator.

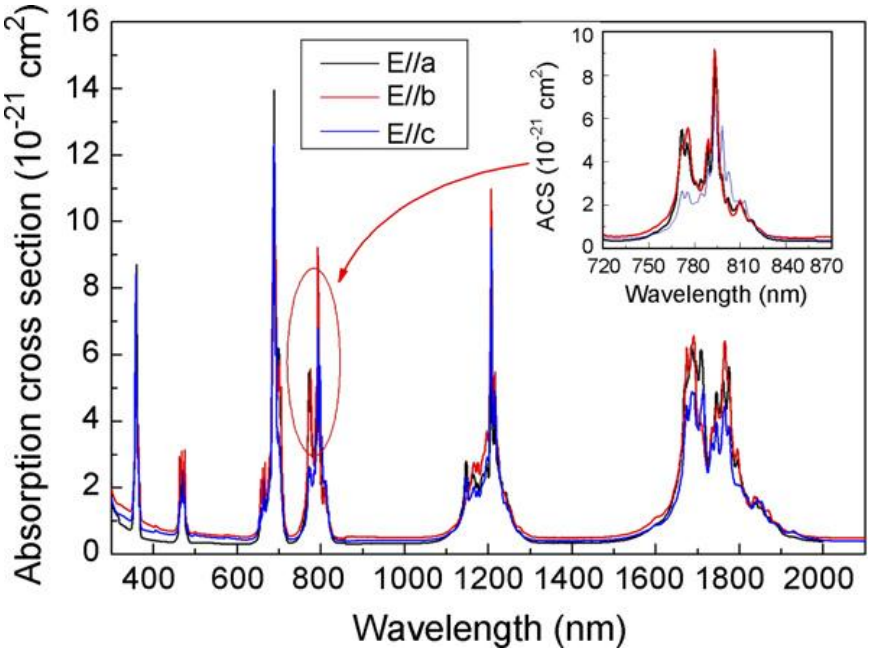

Figure 3.1 The absorption cross-sections of the three crystal axes in Tm:YAP. The b-axis (the red trace) shows a strong absorption peak at 795 nm which is shown in more detailed in the zoomed in section.

As a member of the group of rare-earths (also known as lanthanides), lasing in trivalent thulium ions takes place within the inner ^4F shell of the ions' electronic structure. This is highly advantageous as the outer ^3D shell screens the valence electrons from the crystal field, mitigating this contribution to linebroadening of the laser transitions. This leads to sharper, more defined emission and absorption lines. If one compares this to transition metal ions, where lasing takes place in the outer shells and thus the electrons involved in lasing are directly exposed to the crystal field, transitional metal ions have much broader emission spectrums, with typically broader linewidths, than their rare-earth counterparts.

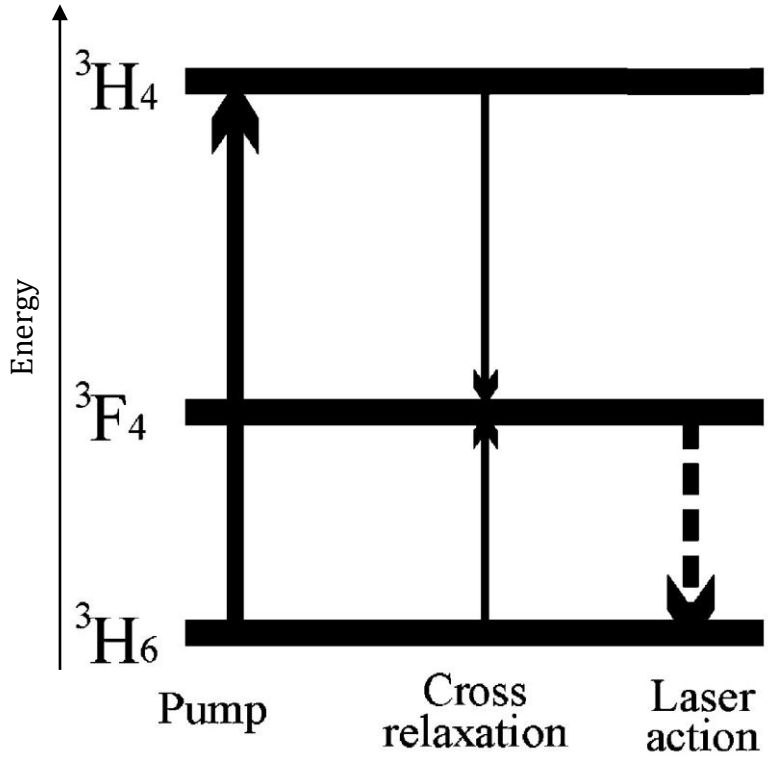

Figure 3.2 A simplified energy level scheme of a Tm^{3+}:YAP ion. The diagram shows a larger spacing between the $^3H_4$ and $^3F_4$ manifolds than between the $^3F_4$ and $^3H_6$ manifolds due to the larger energy difference between the ground state and the upper states of the $^3F_4$ manifold and between the lower states of the $^3F4$ manifold and the upper states of the $^3H_6$ manifold where lasing takes place, with the cross relaxation being a phonon-assisted process. Figure adapted from [5].

A simplified diagram of the energy level scheme in Tm^{3+}:YAP is shown in figure 3.2. As pump radiation is absorbed, electrons are excited from the bottom of the $^3H_6$ manifold to the $^3H_4$ manifold. From there, they then decay to the $^3F_4$ manifold before decaying to the upper levels of the $^3H_6$ manifold – this is the lasing transition. Finally the electrons then decay nonradiatively back down to the

ground state. There are two major points to note from this scheme. The first is that, as the ground state is a manifold of multiple, closely spaced, energy levels, Tm^{3+}:YAP is a quasi-3-level laser and exhibits all of the behaviours related to such devices – such as the requirement that the laser be pumped to transparency due to reabsorption of the laser wavelength by the Tm^{3+} ions before the threshold for laser operation can be reached. Secondly, during the decay from the $^3H_4$ to the $^3F_4$ manifold, it is possible to excite a second thulium ion from the $^3H_6$ to the $^3F_4$ state by cross-relaxation – potentially exciting 2 thulium ions with a single pump photon. While this process is not 100 % efficient, quantum efficiencies, the number of laser photons produced per pump photon, of up to 1.79 have been reported [15].

It should also be noted that Tm^{3+}:YAP has an unusually long upper state lifetime of approximately 4.4 ms [2, 16]. This leads to large, prolonged relaxation oscillations (as discussed in chapter 2) which are detrimental to stable cw-OPO performance. However, this does make it possible to store relatively large amounts of energy in Tm^{3+}:YAP compared to most other gain media, which is ideal for Q-switching.

With the greater peak pump power and therefore ease of reaching threshold provided by Q-switching the parent pump laser, it was decided to first construct a pulsed intracavity OPO to assess the performance and viability of the OP-GaAs crystals in our possession [17]. In the rest of this chapter the cavity design and implementation of a pulsed intracavity OPO device shall be discussed and its major characteristics presented.

3.3 Cavity Design

When designing a cavity to house an optical parametric oscillator there are several things which one must consider. Such considerations include:- should the OPO be single or doubly resonant, how will the resonant signal/idler cavity be separated from the pump cavity, what intracavity components will be needed etc.?

Due to the superior smooth (mode-hop free) tunability offered by a singly resonant OPO when compared to a doubly resonant OPO, along with the relative simplicity and reduced cost of implementing high specification dual-band coatings compared to tri-band coatings, it was decided that a singly resonant intracavity optical parametric oscillator (SR-ICOPO) would be implemented. Due to the simplicity of their realisation and proven efficacy a design similar to those implemented by Stothard et al (and first suggested by Oshman and Harris in 1968) in their analogous Nd:YVO_4 systems was chosen [18-21]. Such designs require that the downconverted signal wave is resonated separately from the pump by means of a dichroic beamsplitter. This is advantageous as it allows the arm of the signal cavity not shared with the pump to be made arbitrarily small, which decreases the signal cavity round trip time. This leads to a larger effective gain being available for the downconversion process per pulse due to the greater number of signal round trips during each pulse. [See chapters 1 & 2 for further discussions]

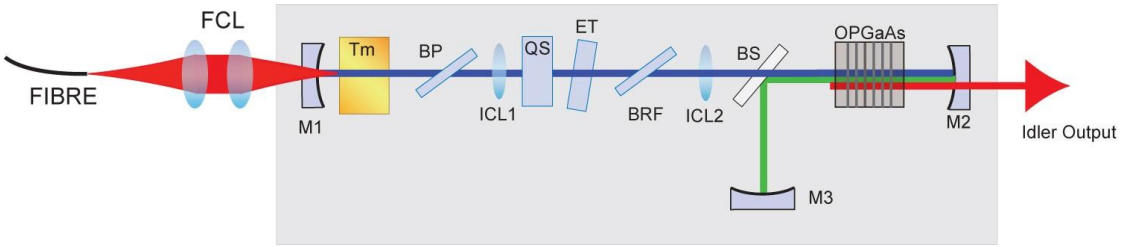

Figure 3.3 A diagram of the pulsed ICOPO based on OP-GaAs. The Tm pump laser was pumped by a 795nm InGaAs diode which was collimated and focussed by a pair of lenses (FCL). Mirror M1(ROC=500mm) was HR @ 2µm and AR @ 795nm, while mirrors M2 and M3 (ROC=50mm) were HR @ both the pump and signal wavelengths, with mirrors M1 and M2, placed 410mm apart, forming the pump laser cavity and M2 and M3 forming the signal cavity. A beamsplitter (BS) was used to separate out the pump and signal cavities and was coated to be AR @ the pump and HR @ the signal. A pair of intracavity lenses (ICL1&2, f=75 and 50mm respectively) were implemented to control the mode size in the cavity. ICL1 was placed 125mm from the end mirror M1, while ICL2 was placed 295mm from M1. A 1mm thick, quartz birefringent filter (BRF) was inserted into the cavity to allow for wavelength selection, with a Brewster plate (BP) being added to further define polarisation. An etalon (ET) was also inserted later to narrow the linewidth of the pump. Finally, an acousto-optic Q-switch (QS) was inserted to modulate the cavity Q.

The final cavity design is shown in figure 3.3 with a photograph of the setup being shown in figure 3.4. This linear cavity contained two intracavity AR coated lenses (ICL1 & 2). These were included to form a collimated section for the Q-Switch and tuning elements, and an appropriate waist in the nonlinear crystal. The end

mirror, M2, was HR at both the pump and signal wavelengths and HT for the nonresonant idler. There is no linear output coupling of the 2 μm pump field, save for the parasitic losses; all of the desired output coupling in this system is through the parametric process. A 5mm long, c-cut, 4 % at. doped Tm^{3+}:YAP crystal was mounted in a water cooled goniometric copper mount, which allowed for rotation of the crystal to allow for the adjustment of the plane of polarisation. The crystal was AR coated at the pump and emission wavelengths. The Tm:YAP laser wavelength was selected by a 1 mm thick quartz birefringent filter (BRF) mounted at Brewster's angle, the selectivity of which was enhanced by an additional Brewster plate (BP). A 1 THz free spectral range (FSR) silicon etalon (ET) could also be included within the collimated section for further spectral narrowing. The combination of the BRF and etalon resulted in course hopping behaviour of the laser every 1 THz as it was tuned over its operating range of 1890-2010 nm. Q-Switching was induced by a water-cooled acousto-optic Q-switch (Gooch and Housego Stallion I-QS027-4C4V5-P5-S11), which could operate up to a pulse repetition rate of ~200 kHz. Its single-pass loss, when holding off laser oscillation was in excess of 50 % on a single pass. The Q-switch was controlled by a digital signal generator, giving control over the frequency and, crucially, the duty cycle. This was necessary in order to drop the Q of the cavity as soon as the parametric process had dumped the circulating 2 μm pump field and so suppress multi-pulsing (see section 3.4.2 for further discussions on this). A repetition rate of 200 kHz was chosen to eliminate the risk of optical damage to intracavity components that results due to the considerable energy storage capacity of Tm^{3+}:YAP. The cavity mode diameter at the Q-Switch, etalon and BRF was approximately 650 μm as shown in figure 3.7.

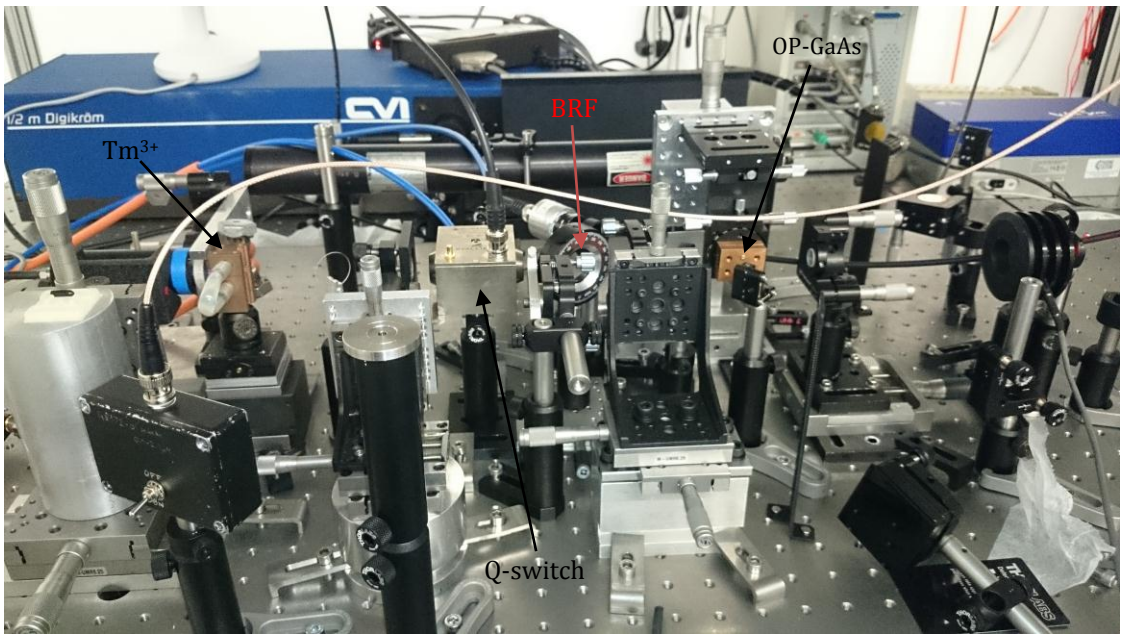

Figure 3.4 A photograph of the ICOPO setup implemented in this chapter. The Tm^{3+} laser crystal, the Q-switch, BRF and OP-GaAs are all highlighted in the image. The beamsplitter is obscured by an x-y-z stage which supports and manoeuvres ICL2. Another such system also supports ICL1.

The 50mm ROC mirror M2, together with the intracavity lens ICL2, resulted in a pump field beam waist of 100 μm located at the centre of the OP-GaAs crystal. The pump and signal cavities were 410 and 135 mm in length, respectively.

An attempt was also made to determine the passive losses within the laser resonator. Both a Findlay-Clay analysis and a Caird analysis were performed, for output couplers of 4 %, 7 % and 10 %, with the resulting data being shown in figures 3.5 and 3.6. From the data provided in figure 3.5, the passive loss estimated by a Findlay-Clay analysis is ~ 47 % - a number which is too large to be physically correct. The Caird analysis, performed using the data in figure 3.6, gives a loss of 0.2 % - a number which is far too small to be a realistic estimate of the sum of the passive losses in the resonator. Indeed, the lenses were assessed separately and were found to have a loss of 0.5 % each on a round trip, rending this physically impossible.

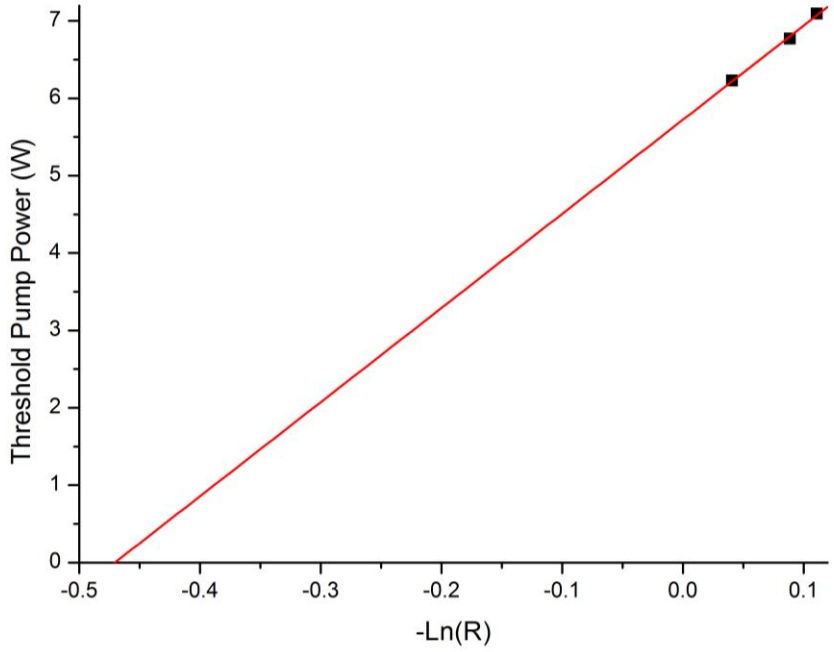

Figure 3.5 A plot of the threshold pump power again the log of the reflectivity for a 4 %, 7 % and 10 % output coupler. A Findlay-Clay analysis gives a passive loss of just over 47 %, a value which is unphysical and thus incorrect.

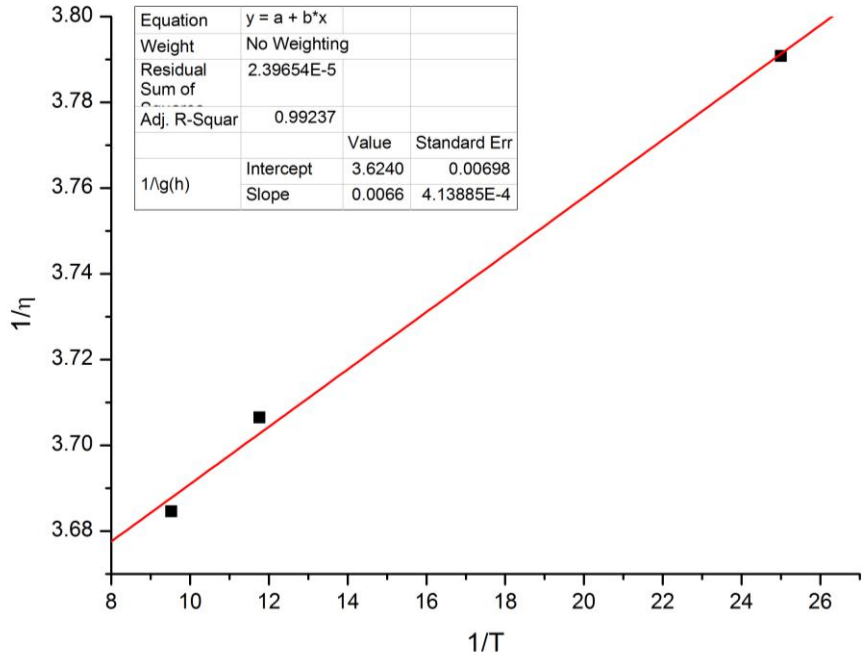

Figure 3.6 A plot of the inverse of the slope efficiency against the inverse of the transmission for a 4 %, 7 % and 10 % output coupler, along with a trendline and the resulting slope and intercept. Performing a Caird analysis on these gives a passive loss of less than one percent. With the lenses in the setup known to have a round trip loss of 0.5 %, the results of this analysis cannot be correct.

As the two standard analyses which are traditionally performed in laser physics failed to produce satisfactory estimates of the passive loss in the laser resonator, a reason was sought as to why these analyses were not applicable to a Tm^{3+}:YAP laser. A closer examination of the assumptions behind both the Findlay-Clay analysis and Caird analysis provide a compelling explanation as to why this may be the case. Both Findlay-Clay and Caird analysis assume that the peak gain is spectrally independent from the loss [22, 23]. For a broadband, quasi-three-level laser such as Tm^{3+}:YAP, this assumption is no longer valid [24]. A method to determine the losses in broadband, quasi-three-level laser systems was recently proposed by Zhao and Major, where a technique based on spectral gain measurements is used to characterise the intracavity losses [24].

OP-GaAs samples 25B and 26K, Λ = 60.5 μm and 56 μm (see appendix A) were both implemented in this system. The crystals were mounted within a passively cooled copper block.

The beam propagation within the Tm^{3+}:YAP pump cavity was modelled using the resonator software Psst!, which is freely available from the University of St. Andrews website, and is shown in figure 3.7. The focus of the laser was outwith the Tm^{3+}:YAP crystal, allowing for optimal mode-matching of the beam and the laser within the crystal. The cavity mode waist within the crystal was approximately 500μm in diameter, which while smaller than the 600 μm waist of the pump beam, works well as a soft aperture to ensure single mode operation. The mode size within the OP-GaAs crystal was estimated to be ~ 100 μm.

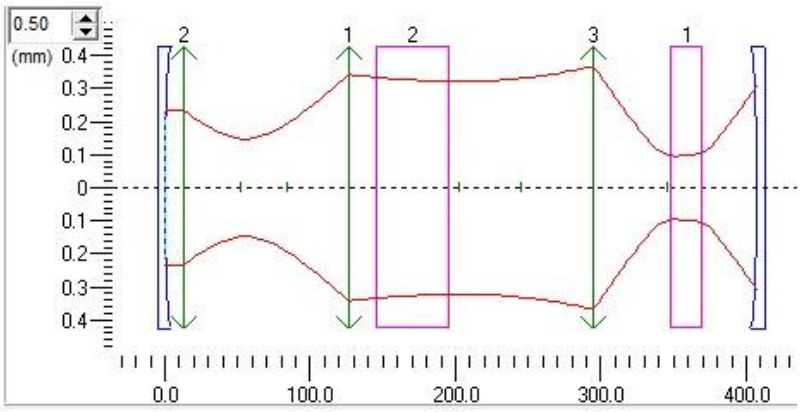

Figure 3.7 Psst! diagram of the resonator mode within the pump cavity of the OPO. The blue shapes represent mirrors, the green arrows lenses and the purple blocks regions of differing refractive index, in this case the Q-switch and the OP-GaAs crystal.

When looking to optimise the performance of an intracavity OPO, the quality of the signal coatings are paramount, as the threshold for operation is highly sensitive to loss at the signal wavelength [17, 20]. The transmission at the signal wavelengths of all of the components of the signal cavity was measured using the idler generated by a tunable Nd:YAG pumped PPLN OPO. The results and their implications on the prospective device are discussed below.

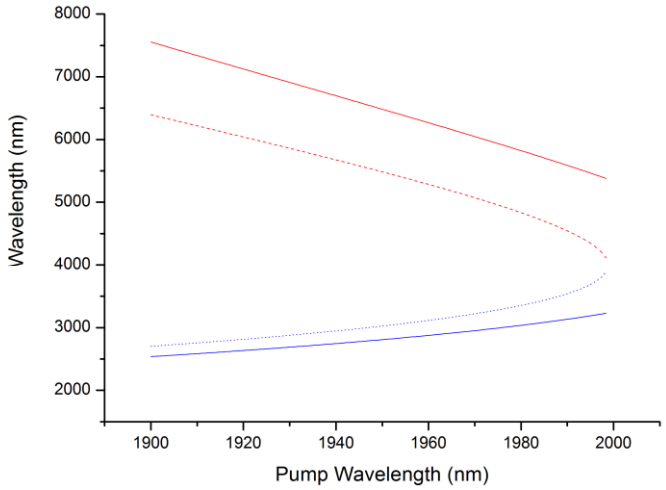

Figure 3.8 A phase matching diagram for OP-GaAs for both 56 μm (dashed lines) and 60.5 μm (solid lines) grating periods showing the signal and idler wavelengths for the relevant tuning range of the thulium pump laser.

The mirrors and beamsplitters (both substrates and ion-beam sputtered coatings) were provided by LaserOptik GmbH. The phase matching curve giving

the signal and idler wavelengths for the OP-GaAs crystals used in this chapter and the transmission for the mirror and beamsplitter coatings are shown in figures 3.8 and 3.9 The transmission for the two OP-GaAs samples (coatings already provided by supplier, not to our specification) is shown in figure 3.10.

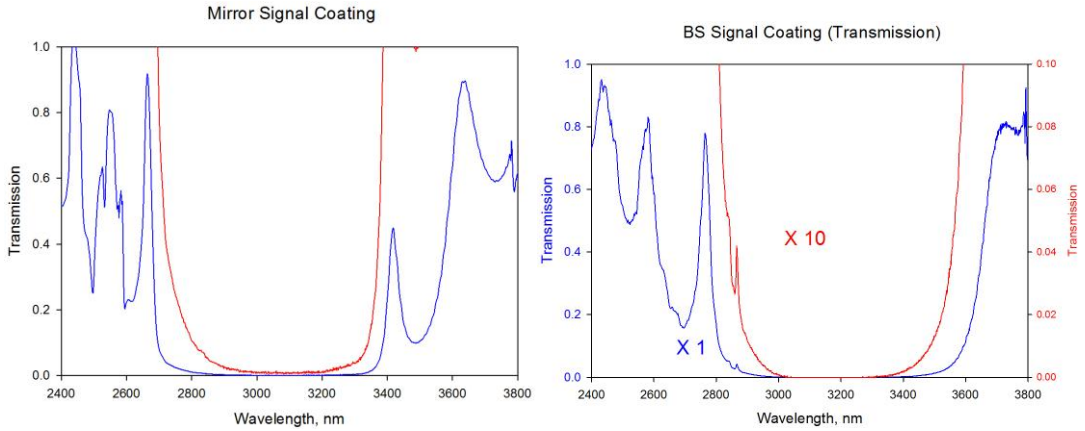

Figure 3.9 The transmission spectrum of the mirrors (left) and beam splitter (right) at the signal wavelength region of the OPO. The red line represents a 10x zoom of the blue trace here.

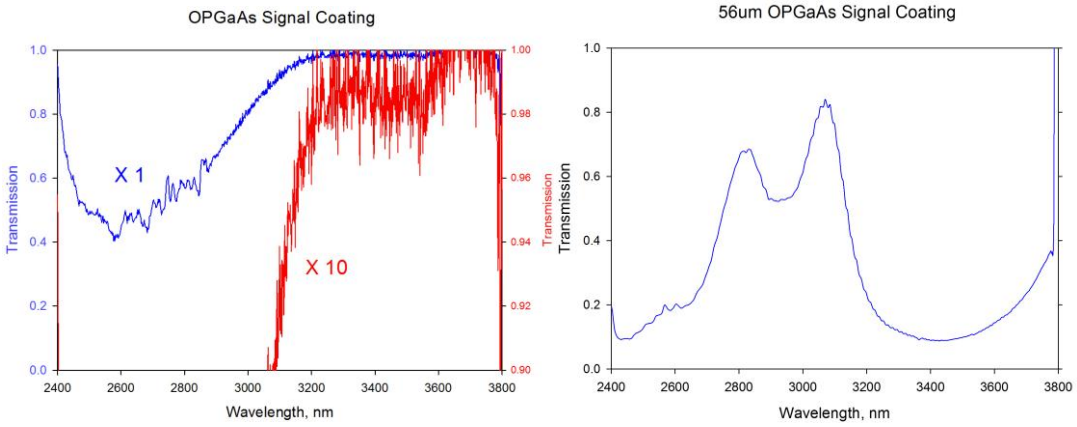

Figure 3.10 The transmission (material+coating) of both OP-GaAs samples 25B (left) and 26K (right) respectively in the signal region. It should be noted that in certain regions, the coating on sample 26K would be better described as being a high reflector, it was later established that it was in fact coated with a partial reflective coating, being AR on one side and PR on the other.

The mirror and beamsplitter coatings are both of excellent quality, reaching transmissions of less than 0.25 % in the spectral region where the signal wave operates. With the operation threshold of the OPO having a strong dependence on the signal loss within the cavity, this is encouraging for successful operation of the device [17]. The signal loss for sample 25B was also low in a region where the resonant signal wave operates; however, this region of operation does not coincide with the preferred wavelengths of operation for the beam splitter and

mirror optics. The coating supplied on sample 26K are of a different nature to the coatings on the other optics. The coating shows no more than 85 % transmission in the spectral region of interest to us, while in another region it offers over 80 % reflection. With the high sensitivity to intracavity loss, this precludes this crystal from use in a cw OPO while it is also likely to hamper, or even preclude, performance in a pulsed OPO device.

3.4 Device Characterisation

3.4.1 Parent Pump Tm^{3+}:YAP Laser Characterisation

Before attempting to construct the cavity outlined in the previous section, the parent pump Tm^{3+}:YAP laser was first characterised. The Tm^{3+}:YAP crystal was placed into a water cooled copper mount and placed between a 500mm ROC high reflecting mirror and a plane output coupler, with the thermal lens in the gain medium being used to stabilize the cavity. A variety of output couplers were then implemented to obtain the various power transfer curves shown in figure 3.11.

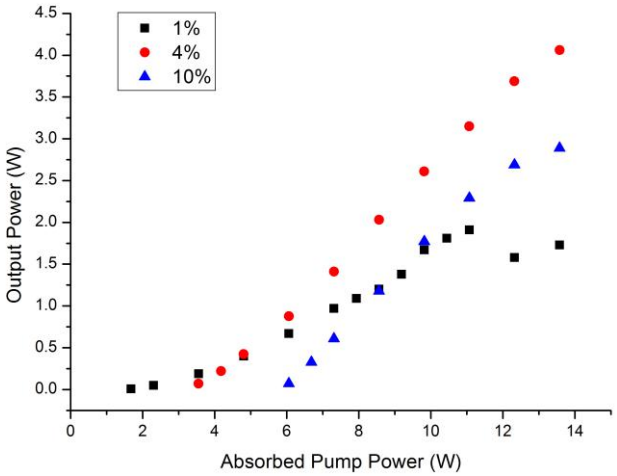

Figure 3.11 Power transfer characteristic for the Tm^{3+}:YAP laser. Power transfers for a 1 %, 4 % and 10 % output coupler are shown.

From figure 3.11 it possible to see that the best output coupler in our possession was 4 % transmission. However, by looking at the maximum output power in relation to output coupling it is possible to see that the optimal output coupling

is closer to 6.5-7 %. Indeed, a 7 % output coupler was borrowed at a later date to confirm this. Sadly the loan did not extend to enough time to generate data points for a power transfer curve. The thermal lens was also estimated from this setup to be 71 mm at 14 W of absorbed pump power.

The cavity in which the Tm^{3+}:YAP was placed was then extended to contain the two intracavity lenses (ICL1&2), the intracavity Q-switch and a 1mm thick quartz birfringent filter (BRF) - (see figure 3.3). A 1 % output coupler was then placed at the focus created by ICL2. The BRF was then rotated and the wavelength output from the laser was recorded by a 0.5 m Digikrom monochromator using a germanium detector and recorded by custom written software for the monochromator. The tuning curve generated is shown in figure 3.12.

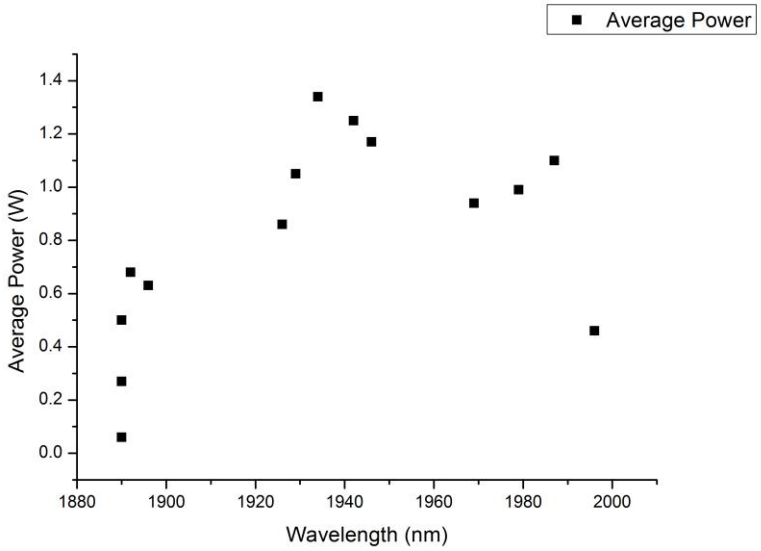

Figure 3.12 The cw tuning curve generated from the c-cut Tm^{3+}:YAP laser. The laser could be tuned between 1.89 μm and 2.01 μm, with the three groups of data points being assigned to transitions from the upper laser level to the top three levels of the ground state, leading to the discontinuity between the data points [7].

From figure 3.12 it can be seen that it is possible to tune the c-cut Tm^{3+}:YAP crystal in our possession from ~1.89 μm to 2.00 μm, offering significant prospects for pump tuning of the OPO, despite the presence of discontinuities in the tuning curve.

3.4.2 Initial Investigations and Temporal Profiling of the Idler Pulse

After investigating the key parameters of the parent pump laser, the cavity was then further extend to match the design shown in figure 3.3. The Q-switch was then turned on at a rep-rate in the 100's of kHz to prevent damage to the intracavity components. The system was then optimised and downconversion was achieved from the pump into the signal and idler. After the first round of optimisation, only 30 mW of useful idler was extracted from 15 W of diode pump power. By examining some of the leaked pump field from the beamsplitter with a fast extended InGaAs photodiode, one could see that the downconversion wasn't very efficient, as shown in figure 3.13 (a. If the system is fully optimised, one would expect the pump to be totally depleted. However, as figure 3.13(a shows, the pump field wasn't completely depleted and was in fact able to recover partially before the Q-switch closed.

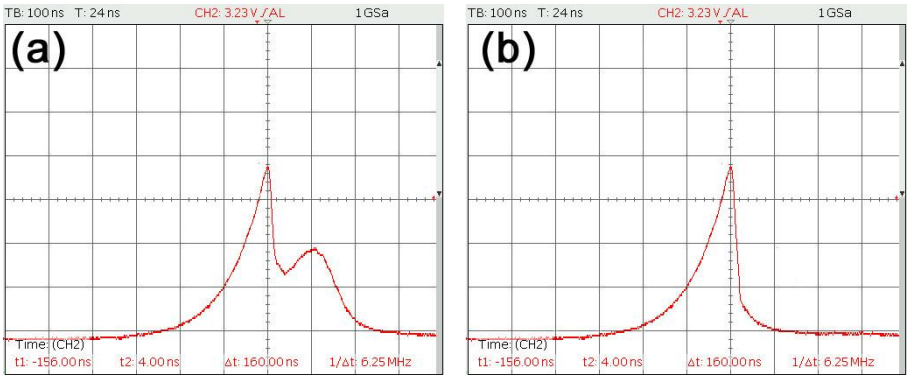

Figure 3.13 Oscilloscope traces recorded on a fast extended InGaAs photodiode showing a) the partial depletion of the pump pulse by the OPO before the etalon was added to the cavity and b) the total depletion of the pump by the OPO after the insertion of the etalon. The area of the photodiode was 1 mm² and it had a risetime of 1 ns.

The non-linear crystal OP-GaAs is known to have a very narrow phase matching bandwidth, often on the order of a few wavenumbers depending on length (which is on the order of 1 nm (~3 cm^{-1}) for a crystal of length 16.4 mm (the same length as sample 25B), pumped at 1.93 μm with a signal and idler of 2.69 μm and 6.89 μm – see chapter 2 for further information in this topic) [25]. So it was suspected that, if the pump pulses were too spectrally broad to fit into the phase matching

bandwidth, this would lead to reduced downconversion efficiency as much of the energy would lie outwith the accepted bandwidth. A 1 THz free spectral range silicon etalon was introduced into the cavity to narrow the spectral linewidth. The effect this had can be seen in figure 3.14. The pump laser was found to have a FWHM of 4.26 nm before the etalon was inserted, which translates to approx. 12 cm^{-1}. This is significantly broader than the phase matching acceptance bandwidth of the crystals. However, once the etalon was included, the linewidth narrowed to 0.25 nm FWHM, which translates to 0.06 cm^{-1}, which lies comfortably within the phase matching bandwidth. This led to total downconversion of the pump pulse, as shown in figure 3.13 b). This improved the useful idler extracted from the OPO by a factor of >3, leading to 100's of mW of idler being produced for 15 W of diode pump power.

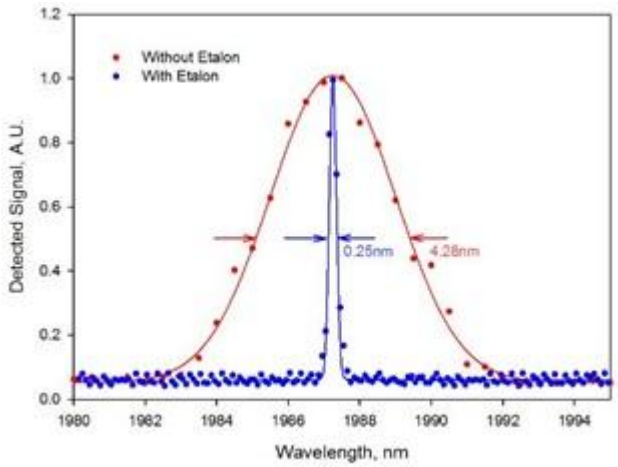

Figure 3.14 A monochromator trace of the pump pulse showing the linewidth before (in red) and after an intracavity etalon had been introduced (in blue). The reduction in linewidth seen is significant, reducing the linewidth from 4.28 nm to 0.25 nm.

To achieve the single depleted pump pulse per Q-switching cycle seen in figure 3.13 b), the repetition rate, as well as the gate width, of the Q-switch had to be adjusted. When the etalon was first inserted, multiple pulsing behaviour was observed, as shown in figure 3.15. This was due to their being enough gain left stored in the upper state population of the Tm^{3+}:YAP for the pump field to recover and deplete again within the gate width of the Q-switch. By narrowing the gate width such that the Q-switch closed as soon as the pump pulse was depleted, single pulses could be generated. Further increasing the repetition rate then

allowed for the optimum extraction of energy by adjusting for the largest number of single pulses per unit time producing the greatest useful average idler output [26].

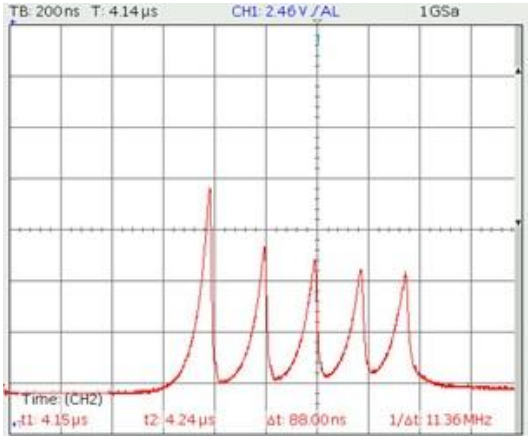

Figure 3.15 An oscilloscope read out showing multiple pulsing behaviour of the pump pulse in the OPO. The pump pulse can be seen to reach threshold of the OPO and deplete, before recoving and repeating the process multiple times.

In order to determine the pulse duration of the idler, one would normally use a fast photo detector that is sensitive to the idler wavelength. However, for the long idler wavelengths generated here (>6 µm), there were no suitable detectors available in our group. To circumvent this, one can instead infer and estimate the pulse duration of the idler by looking at the temporal dynamics of the pump and signal pulses, as the idler pulse is only produced when both the pump and signal pulses are present. In the case where downconversion efficiency is high, the pump pulse begins depleting as soon as the OPO reaches threshold [27]. As the idler pulse can only be generated while both the signal and pump pulses are present, in this situation the idler pulse length can be no longer than the depletion time of the pump pulse. As we were able to demonstrate good downconversion earlier, it is safe to assume that this is a valid assumption for this pulsed ICOPO. To set up the experiment, the pump pulse picked off from the cavity by the back surface of the beamsplitter was fed into a fast extended InGaAs photodiode to measure the pump pulse duration. The output from the end mirror was then passed through a monochromator (Digikrom, 0.5 m throw) to separate out the signal from the pump and the output was detected by an thermo-electrically cooled Vigo systems PVI-2TE-4 (HgCd)Te photo detector, which was sensitive at

the signal wavelength. The output from both photodetectors is shown in figure 3.16.

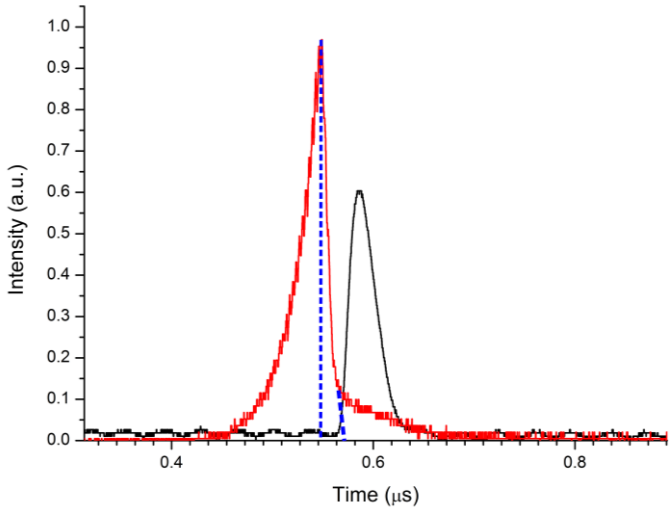

Figure 3.16 A plot showing the pump (red) and signal (black) pules. The region where the pump and signal would be overlapped (they're not overlapped on the graph shown due to the difference in time of flight to the two different detectors) is demarked by the blue dashed lines. This was found to cover a period of ~ 15 ns.

Unfortunately there was some unwanted ringing in the pump detector that obscures the measurement. However, by extrapolating where the pump pulse should have depleted, the overlap between the pump and the signal was estimated to be ~15 ns. From this one can deduce that the idler pulses must be less than 15 ns in duration.

3.4.3 Tuning Performance of the OPO

With the device now operating successfully, the range over which the device could be tuned was investigated. To measure the tuning performance, the output leaking out of the high-reflector M3 at the end of the cavity was collected and fed into a digikrom monochromator with a germanium detector. With only the pump and signal wavelengths being within the detection range of the monochromator,

all idler wavelengths were inferred from the pump and signal wavelengths and conservation of energy.

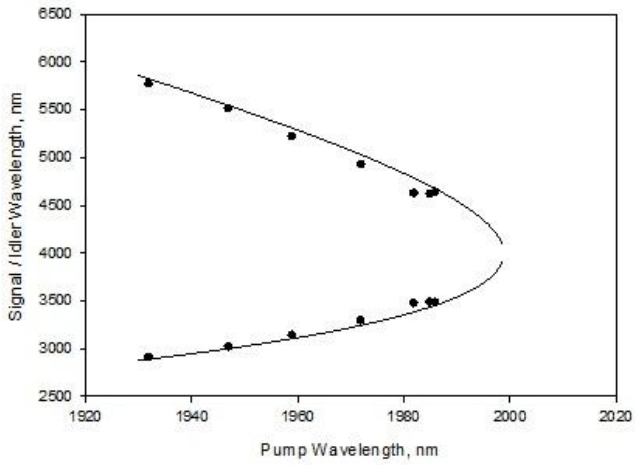

Figure 3.17 The tuning curve generated from crystal 26K, which had a grating pitch of 56 µm. The dots represent measured data points while the curves represent predicted phase matching curves generated by the SNLO software. The data points are spaced 1 THz apart in frequency due to the inclusion of an intracavity etalon.

Initially, crystal 26K was placed into the cavity and, by rotating the birefringent filter, its tuning behaviour was investigated. The resultant tuning curve is shown in figure 3.17 alongside a predicted phase matching curve generated by the modelling software SNLO. It was possible to tune the device from 2.9-3.5 µm (0.6µm) in the signal and 4.6-5.8 µm (1.2µm) in the idler for 54 nm of tuning in the pump. From figure 3.15 it is possible to see that the predicted curve and the measured data points are in good agreement. The data points are spread 1 THz apart due to the inclusion of the THz free spectral range silicon etalon in the cavity.

To produce a truly smooth tuning curve, an intracavity element which selects continuously both for single wavelength and narrow linewidth would need to be implemented. A Lyot filter, a device made by stacking several birefringent filters which are an integer multiple of each other in thickness, was the optimal solution to this problem [28]. A Lyot filter, formally from a Ti:Sapphire laser, was recruited for use in the OPO. The Lyot filter had three plates made from birefringent quartz of thicknesses 0.33 mm, 1.32 mm and 5.29 mm respectively. Unfortunately,

before the Lyot filter could be inserted into the cavity, crystal 26K was recalled from us by its owner.

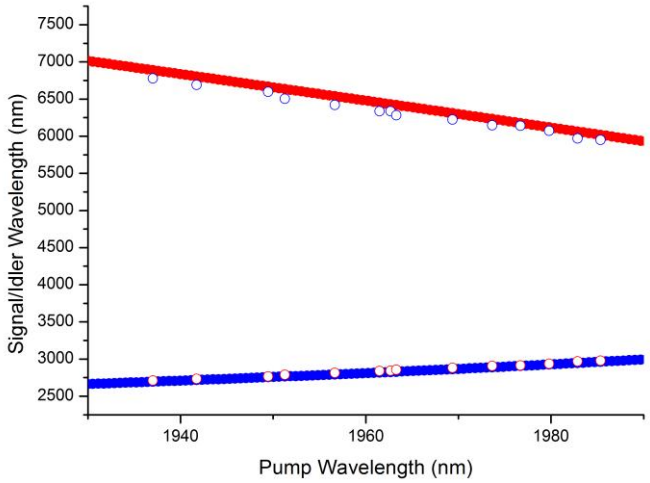

Figure 3.18 The tuning curve produced from crystal 25B. The blue line represents the predicted signal generated by SNLO, while the hollow red circles represent measured data points. The inverted colour scheme at the top of the image represents the idler

With the Lyot filter implemented, crystal 25B, which had a grating period of 60.5μm, was also introduced into the cavity and its tuning performance was then ascertained. The resultant tuning curve is shown in figure 3.18. The OPO could be tuned from 5.9-6.8 μm (0.9 μm) in idler & 2.7-3 μm (0.3 μm) in signal for 50 nm of tuning in the pump. Once again, the experimental results are in good agreement with the theoretical predictions. The two tuning curves are shown together in figure 3.19 for comparison.

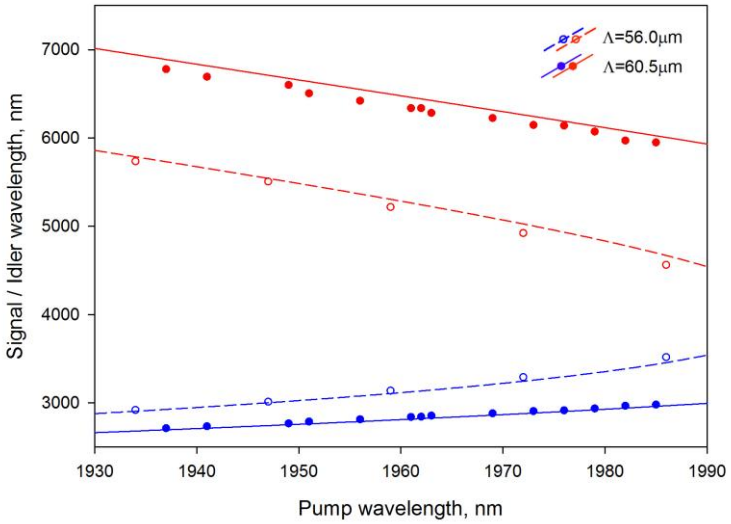

Figure 3.19 A plot showing the tuning curves for both OP-GaAs crystals 25B and 26K. The lines represent the theoretical prediction of the SNLO program while the points represent measured and inferred data.

3.4.4 Power and Efficiency Performance of the OPO

The performance of the OPO was next characterised in terms of its output power and downconversion efficiency. To examine the output power, the etalon was reintroduced into the cavity due to its lower loss compared with the Lyot filter. The extracted idler power was measure by placing a high reflecting slide for the pump and signal in front of a Coherent field mate thermal power meter.

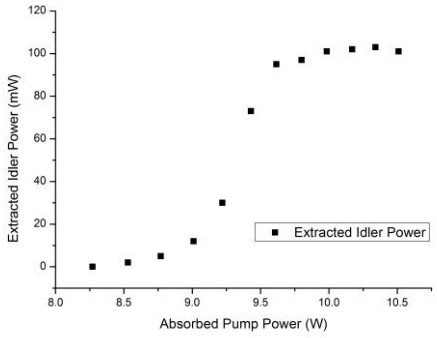

Figure 3.20 A power transfer obtained from the OPO with a fixed rep rate. The output power collapses rapidly as the per pulse energy becomes too low to reach threshold on a single pass of the OP-GaAs crystal.

The output power was then optimised and a power transfer curve was taken by reducing the primary pump power to the Tm^{3+}:YAP laser, and monitoring the fall

in idler power. The resultant curve generated is shown in figure 3.20. It can immediately be seen by an experienced laser scientist or engineer that there is something interesting about this curve. By reducing the absorbed primary pump power in the Tm^{3+}:YAP pump laser, the build-up time for the population inversion to reach a certain level is increased. If the repetition rate, and therefore the time between cavity dumping events, is fixed, then the available energy per pulse is reduced. Once the energy per pulse becomes less than the value required for the OPO to reach threshold on a single pulse, the output power of the laser collapses rapidly with reduced primary pump powers [26]. A second power transfer was taken, varying the repetition rate and gate width until the power is maximised for each data point, which is shown in figure 3.21.

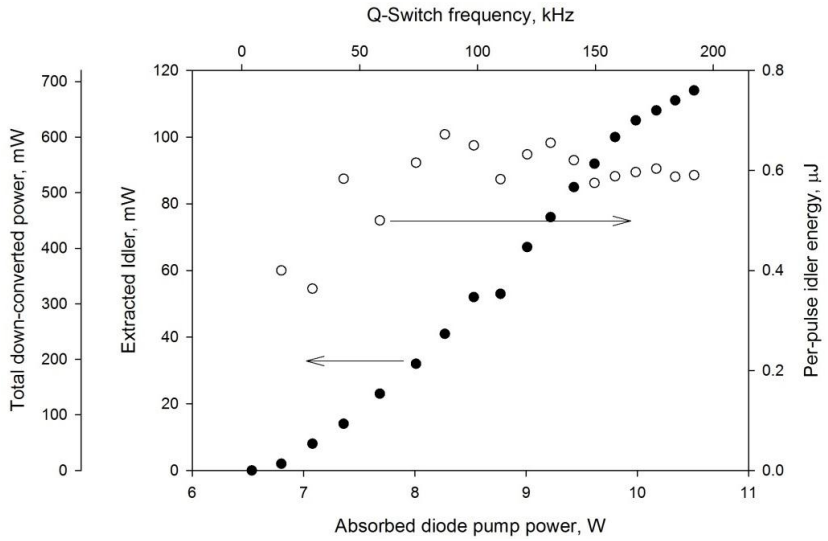

Figure 3.21 The power transfer characteristic obtained by varying the rep rate and the gate width at different pump powers shown alongside the per pulse energy and q-switch rep rate. It can be seen that the optimum per pulse energy is roughly constant once one is pumping far enough above the threshold condition. This may perhaps be due to the OPO only reaching threshold on every second pulse.

.

By looking at the how the per pulse energy varied with each data point, also shown in figure 3.21, it can be seen that the per pulse energy remains roughly constant until the pump laser is brought close to threshold, where the population inversion can never be made large enough to reach the optimal per pulse energy, along with the pulse fluence, which is shown in figure 3.22.

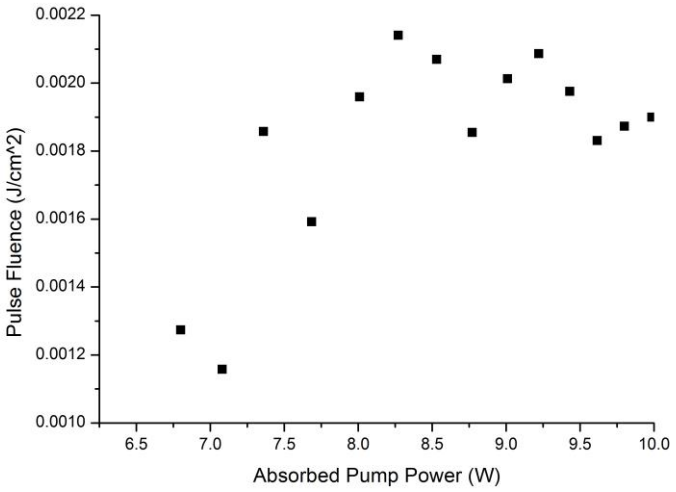

Figure3.22 A plot of the pulse fluence in J/cm^{-2} against absorbed pump power for the data points shown in figure 3.19. It can be seen that the optimum fluence is roughly constant once one is pumping far enough above the threshold condition.

The maximum useful idler power extracted from the laser was 120 mW at a wavelength of 5.3 μm. This was extracted from sample 26K before it was recalled. This was anticipated as sample 26K's shorter grating period, and consequently shorter idler wavelength, lead to each individual idler photon possessing more energy than its longer wavelength counterpart from sample 25B.

When discussing the efficiency of an intracavity OPO device, there are some important, if counter intuitive at first, things to take into account. As the downconversion process is being used to output couple the intracavity field, as opposed to the more traditional extracavity configuration where it is used to downconvert the output coupled field from the pump laser, the definition of downconversion efficiency has to be redressed. Therefore, to define the downconversion efficiency of an intracavity OPO, the total downconverted power (which consists of the total power of the signal and idler fields extracted from both facets of the non-linear crystal) is compared to the field that could be output coupled for the equivalent amount of linear loss [20, 26]. With 120 mW of useful idler being extracted at a wavelength of 5.3 μm, there was an estimated 650 mW of downconverted power (both signal and idler), assuming that the idler power emitted from both facets of the non-linear crystal was of equal magnitude. As the

intracavity pump field was completely depleted, it can be assumed that the OPO is acting as an optimal output coupler for the laser. From earlier in this chapter, we know that the optimal output coupling for the Tm^{3+}:YAP laser was in the region of 7 %. The end mirror of the OPO was replaced with a 7 % output coupler and 1.08 W of 2 μm radiation was extracted. From our earlier definition, this gives a downconversion efficiency of 60 % [26].

3.5 Tm^{3+}:YAP Pump Laser Efficiency

In the previous section, we characterized the efficiency of the OPO. However, to set this into the context of device efficiency, the efficiency of the parent pump laser under Q-switched conditions must also be characterized. In this section the efficiency of the parent pump laser in both cw and Q-switched conditions shall be characterised and compared, and the implications that this has on the device will be discussed.

The efficiency of a 4-level solid state laser gain material is fundamentally limited by the quantum defect between pump and laser photons, along with the pump power required to create a sufficient population inversion in the gain medium, with this being seen as the maximum approachable limit for device efficiency. In a quasi-3-level system such as thulium, the reabsorption losses caused by the reabsorption of laser photons by ions in the ground state complicate the picture and hinder the creation of a population inversion. For a true 3-level system, this leads to a fractional population inversion of >50 % of the laser ions being required to bring the laser to threshold. With the lower laser level not being completely populated, instead only being thermally populated according to Boltzmann's distribution, the population inversion required by a quasi-3-level system can be (and often is) less than the 50 % required by a true 3-level system, but can never be as low as the single ion required to create a population inversion in a true 4-level system. This pushes up the absorbed pump power required to reach threshold in a quasi-3-level system.

With pulsed systems, there is another source of inefficiency introduced into the

system – spontaneous emission of photons from ions in the upper laser level while the Q-switch is holding off the cavity. The major factors governing this process are the upper state lifetime of the lasing transition and the repetition rate at which the Q-switch operates. If the hold off time of the Q-switch is greater than the upper state lifetime, then one can expect a large proportion of excited ions to emit spontaneously, which drastically reduces the efficiency of the device. However, should the upper state lifetime of the lasing transition be much longer than the hold off time of the Q-switch, then one can expect very little spontaneous emission from the upper laser level between pulses, reducing the unnecessary losses the Q-switching process can introduce, and improving the efficiency of the device close to cw like levels. For the laser described in this chapter the upper state lifetime was 4.4 ms and the repetition rate 200 kHz, giving a pulse every 5 μs, which is saturated down to cw like levels and is well in the high efficiency regime [26].

To investigate the impact that the Q-switching process was having on the efficiency of the device, the following experiment was undertaken. One can measure the fraction of the population inversion that was lost to spontaneous emission during operation by measuring the fluorescence while the cavity is blocked and during laser operation and compare the two to see the ratio of upper state ions which contribute to stimulated emission. Unfortunately, it was impossible to access the fluorescence emitted from the Tm^{3+}:YAP laser directly due to the water cooled copper block it was mounted in. This required the development of an alternative experimental approach. The experiment was setup as follows in figure 3.23.

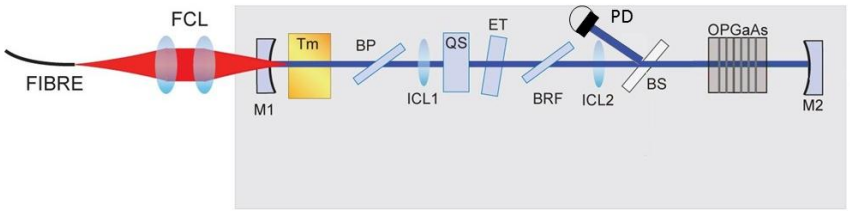

Figure 3.23 A diagram of the setup used to measure the fluorescence output from the gain medium. The setup is mostly identical to the setup in figure 3.3. except that a photodiode (PD) has been placed to detect the light rejected from the cavity by the beam splitter. A 1400 nm long-pass filter was placed in front of the diode to exclude any 795 nm pump light from the measurement.

The laser was setup up as shown in figure 3.23, much like it was for the earlier experiments in figure 3.3, but without the addition of the signal cavity of the OPO. To measure the fluorescence from the crystal, an extended InGaAs photodiode was used to collect and measure the pick off from the back of the beamsplitter – allowing for measurement of the spontaneous emission into the cavity. A 1400 nm long-pass filter was placed in front of the photodiode to block out any pump light. This approach comes with an additional drawback, however. With the photodiode being placed such that it detects photons emitted into the cavity, as soon as the laser begins to oscillate, the stimulated emission from the laser into the cavity will mask the spontaneous emission due to its much greater intensity. This makes it impossible to measure the spontaneous emission during operation of the device, rending direct measurement of the relative levels of spontaneous and stimulated emission during operation unachievable. However, the level of spontaneous emission during operation can be inferred from what the level of spontaneous emission is at threshold, if one assumes the gain of the laser is well clamped above threshold. With this in mind, the experiment was performed and the following results were produced, as shown in figure 3.24.

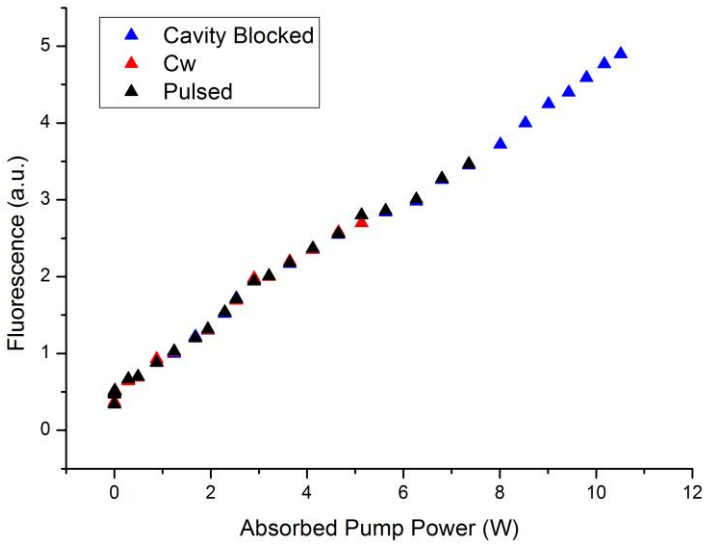

Figure 3.24 A plot of the spontaneous emission from the laser when the cavity is blocked (shown by the blue triangles), when the laser is operating cw below threshold (shown by the red triangles) and when the laser is operating in the pulsed regime below threshold (shown by the blue triangles).

From the data presented in figure 3.24, by taking the ratio of the fluorescence at threshold for each process compared to the fluorescence from the cavity when blocked at the maximum absorbed pump power it was experimentally operated at, it can be shown that 55 % of the excited ions in the cw regime emit spontaneously while 70 % of ions in the pulsed case do likewise at the maximum absorbed pump power (one can deduce this by taking the ratio of fluorescence at threshold for each case in which the laser operates and comparing it to the fluorescence produced at the maximum absorbed power the laser was operated at with lasing inhibited– when the cavity was blocked in this case). This indicates that there is only a small increase in inefficiency due to the Q-switching process. However, with over 50 % of the ions in the gain medium emitting spontaneously in the cw-case, it does indicate the parent pump laser itself is inefficient, which renders the optical to optical efficiency of the whole device to be poorer than one would hope. With the high threshold pump powers, reducing the threshold would significantly reduce the inefficiency of the device.

There are several, fundamental reasons why the parent pump laser itself is inefficient, and these all lie with its quasi-3-level nature. While this introduces some unavoidable increases to the pump power required to reach threshold, it also introduces several parameter dependent increases which will be discussed below, as well as improvements that can be made to the set up to minimize them. The threshold absorbed pump power of a quasi-3-level system depends on a number of factors, which hold to the relation shown below [29].

$$P_{th} = \frac{\gamma\left(1+\frac{\sigma_a N_t l}{\gamma}\right)}{\eta_p}\left(\frac{h\nu_p}{\tau}\right)\left[\frac{\pi\left(\omega_2^0+\omega_2^p\right)}{2\left(\sigma_a+\sigma_e\right)}\right] \quad (equation\ 3.1)$$

Where γ is the total losses within the cavity, N_t is the number density of ions, l is the length of the crystal, η_p is the quantum defect within the laser (one must take into account up-conversion in Tm:YAP here), ν_p is the frequency of the laser photons, τ is the upper state lifetime of the lasing transition, ω_0 and ω_p are the cavity and pump mode radii in the crystal respectively and σ_e and σ_a are the emission and absorption cross sections respectively here [29].

While there is little which can be done to alter certain factors such as the loss within the resonator (the system already consists entirely of low loss components and high reflector mirrors and was constructed to minimize losses), the laser frequency, the upper state lifetime or the emission and absorption cross section, there are other factors which we can adjust to improve the laser performance. The simplest parameters which are available for us to adjust are the length of the crystal and the pump and cavity mode sizes. From equation 2.1 it can be seen that decreasing the length of the crystal leads to a corresponding linear decrease in pump threshold. Reducing the crystal length also leads to greater confocality in the crystal which leads to a smaller average pump waist within it, which produces another decrease in the threshold. It is also within the experimenter's power to reduce the size of the pump waist, and consequentially the cavity mode size when mode matched, in the crystal. This also leads to a reduction in the operating threshold according to equation 3.1. Using brighter pump sources, provides a simple, if expensive, route to improving device efficiency.

From the above analysis we conclude that, while the OPO shows good downconversion efficiency, the parent pump laser shows poor efficiency. In the context of producing a practical device with good wall plug efficiency, several improvements to the parent pump laser system would have to be made. By shortening the crystal length and coating its rear face with an AR coating to recycle the diode pump and increasing the brightness of the diode, the threshold for operation of the device, and consequently the output power for a given diode pump power could be improved.

3.6 Conclusions

Tm^{3+}:YAP was identified as a suitable pump laser for an OP-GaAs OPO. By examining its properties, in particular its long upper state lifetime, it was concluded that first constructing a pulsed OPO would be the best path of progression. The operation of a Tm^{3+}:YAP pumped pulsed OPO based on orientation patterned gallium arsenide was demonstrated. For 15 W of incident

diode pump power (10.5 W absorbed) up to 120 mW of useful idler (650 mW of total downconverted power) could be extracted from the device at a repetition rate of 200kHz. Based on output coupling 1.08 W at 7 % output coupling, this gives us a downconversion efficiency of 60 %. The OPO could be tuned over the range 2.9-3.5 μm (0.6 μm) in the signal and 4.6-5.8 μm (1.2 μm) in the idler for 54 nm of tuning in the pump for a 56 μm period crystal. For a crystal of QPM grating period of 60.5 μm the OPO could be tuned over the range 5.9-6.8 μm (0.9 μm) in idler & 2.7-3 μm (0.3 μm) in signal for 50 nm of tuning in the pump. While the downconversion efficiency of the OPO is good, the Tm^{3+}:YAP pump laser was shown to be inefficient itself, rendering the device as a whole inefficient in terms of optical to optical efficiency. This is, however, to the best of our knowledge, the first and only intracavity pumped OP-GaAs OPO pumped with Tm^{3+}:YAP in the world.

The performance of the device demonstrated in this chapter could be improved in a number of ways. The most significant, and also the easiest to ameliorate, are the factors related to the high threshold pump power of the Tm^{3+}:YAP laser. Earlier in the chapter, it was discussed how reducing the length of the crystal would decrease the threshold pump power required for laser operation. By replacing the current crystal with a shorter crystal, such as a 2.5 mm long crystal (such as those commercially available from Scientific Materials Corporation) would lead to significantly reduced pump thresholds with regards to absorbed pump power. By replacing the coatings on one face of the crystal with one which is AR at the emission wavelength, but HR at the pump, the transmitted pump can be recycled. This would increase the amount of pump power absorbed from the diode laser for a given amount of electrical power. The fibre coupled diode laser which was used to pump the thulium laser also offers an easy path towards device optimisation. With a fibre core diameter of 600 μm, the beam wasn't particularly bright which led to the requirement of a relatively large cavity mode diameter within the crystal. By switching to a brighter pump diode (200 μm fibre diode pump lasers are now commercially available), the threshold pump power of the laser could be reduced even further, increasing wall plug efficiency of the device.

However, in this regime, care must be taken to control the thermal lensing within the crystal by using an approach such as more aggressive cooling or pumping with a top hat pump beam.

The downconversion efficiency within the OPO would be another area where improvements could be made. The signal coatings for the OP-GaAs crystals in our possession at this stage in the project (samples 25B and 26K) were non-optimal for the range of pump wavelengths available from the Tm^{3+}:YAP laser. It was later discovered that they were supplied coated for Ho:YAG wavelengths (~2.1 μm). The OP-GaAs crystals both phase matched for the pump wavelength in areas of moderate to serious loss at the signal wavelength from the coatings on their end facets. Indeed the coating on sample 26K was actually acting as more of a high reflector for the signal with the end facet acting as the terminus of the signal cavity. The overlap between all of the signal coatings for sample 26K are shown in figure 3.25. The mirror and beamsplitter coatings, however, align reasonably well with Tm^{3+}:YAP's gain bandwidth.

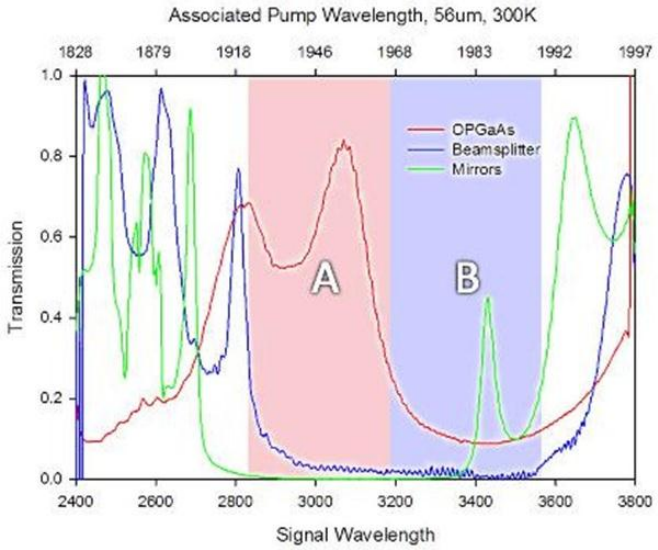

Figure 3.25 A diagram showing the overlap between the signal coatings on the mirror, beamsplitter and crystal for sample 26K. While section A offers up to ~85 % transmissin in the OP-GaAs crystal, in section B the coating actually offers up to 90 % reflectivity, which inhibits operation in this range.

Unfortunately, the case was not so clear for sample 25B. Not only were the signal coatings of the crystal not well matched to our pump, to also further constrain things, the signal wavelengths generated by sample 25B were not well matched

to the beamsplitter and mirror coatings either. The overlap between the various coatings are shown in figure 3.26

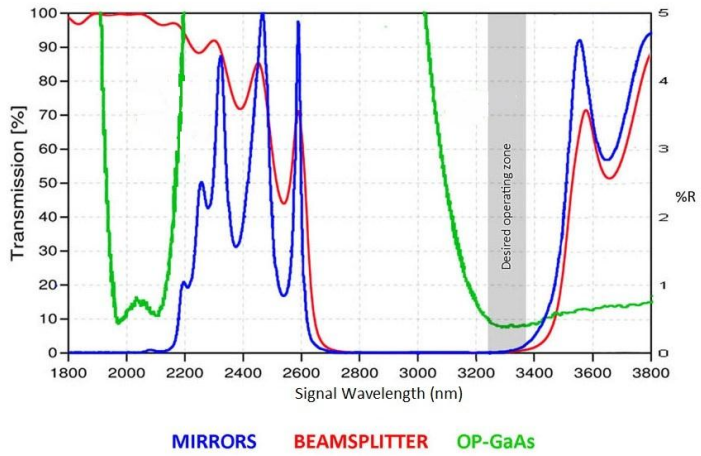

Figure 3.26 A plot displaying the overlap between the mirror, beamsplitter and OP-GaAs. The area highlighted in grey shows the region where the losses at the signal wavelength are minimized, unfortunately this required a pump wavelength of 2020-2030 nm which is outwith the gain bandwidth of Thulium.

From figure 3.26 it is possible to see that the smallest round trip loss introduced by the signal coatings is at a point between 3200 nm and 3400 nm – which requires and a pump wavelength of 2020-2030 nm. This lies outwith the gain bandwidth of a Tm^{3+}:YAP laser, making optimum operating parameters unreachable. By recoating both sample 25B and 26K such that the signal loss at the appropriate wavelengths is minimized, as well as having a new set of beamsplitter and mirror optics made which are compatible with the signal wavelengths of sample 25B, the efficiency of downconversion process can be enhanced.

In the next chapter, an investigation is undertaken into producing a cw-ICOPO based on Op-GaAs using a SDL as a pump source. The initial investigations into this shall be outlined and the requirement thresholds modelled, and shall be presented along with a characterisation of the system.

3.7 References

1. Weber, M.J., et al., *Laser Action from Ho^{3+}, Er^{3+}, and Tm^{3+} in $YAlO_3$.* IEEE Journal of Quantum Electronics, 1973. **9**(11): p. 1079-1086.

2. Elder, I.F. and J. Payne, *Diode-pumped, Room-temperature Tm:YAP Laser.* Applied Optics, 1997. **36**(33): p. 8606-8610.
3. Elder, I.F. and M.J.P. Payne, *Lasing in Diode-pumped Tm:YAP, Tm,Ho:YAP and Tm,Ho:YLF.* Optics Communications, 1998. **145**(1–6): p. 329-339.
4. Stoneman, R.C. and L. Esterowitz, *Efficient 1.94 μm Tm:YALO Laser.* IEEE Journal of Selected Topics in Quantum Electronics, 1995. **1**(1): p. 78-81.
5. Cemy, P. and D. Burns, *Modeling and Experimental Investigation of a Diode-pumped Tm:$YAlO_3$ Laser with a- and b-cut Crystal Orientations.* IEEE Journal of Selected Topics in Quantum Electronics, 2005. **11**(3): p. 674-681.
6. Cerny, P., G.J. Valentine, and D. Burns, *Actively Stabilised Diode Pumped Tm:YAlO Laser.* Electronics Letters, 2004. **40**(17): p. 1061-1063.
7. Elder, I.F. and M.J.P. Payne, *YAP versus YAG as a diode-pumped host for thulium.* Optics Communications, 1998. **148**(4–6): p. 265-269.
8. Suni, P.J.M. and S.W. Henderson, *1-mJ/pulse Tm:YAG laser pumped by a 3-W diode laser.* Optics Letters, 1991. **16**(11): p. 817-819.
9. Lu, Y., et al., *Growth and optical properties of Tm:$YAlO_3$ single crystals with different Tm concentrations.* Journal of Alloys and Compounds, 2007. **429**(1–2): p. 296-300.
10. Weber, M.J., et al., *Czochralski Growth and Properties of $YAlO_3$ Laser Crystals.* Applied Physics Letters, 1969. **15**(10): p. 342-345.
11. Duan, X.M., et al., *Diode-pumped High Efficient Tm:YLF Laser Output at 1908 nm with Near-diffraction Limited Beam Quality.* Laser Physics Letters, 2008. **5**(5): p. 347.
12. Hardman, P.J., et al., *Energy-transfer upconversion and thermal lensing in high-power end-pumped Nd:YLF laser crystals.* IEEE Journal of Quantum Electronics, 1999. **35**(4): p. 647-655.
13. Basavalingu, B., et al., *Hydrothermal synthesis and characterization of orthorhombic yttrium aluminum perovskites (YAP).* Materials Chemistry and Physics, 2008. **112**(3): p. 723-725.
14. Lu, Y., et al., *Anisotropy of thermal and spectral characteristics in Tm:YAP laser crystals.* Journal of Alloys and Compounds, 2008. **453**(1–2): p. 482-486.
15. Thevar, T. and N.P. Barnes, *Diode-pumped, continuous-wave Tm:YAIO3 laser.* Applied Optics, 2006. **45**(14): p. 3352-3355.
16. Payne, S.A., et al., *Infrared Cross-section Measurements for Crystals Doped with Er^{3+}, Tm^{3+}, and Ho^{3+}.* IEEE Journal of Quantum Electronics, 1992. **28**(11): p. 2619-2630.
17. Stothard, D.J.M., *Practical Continuous Wave Optical Parametric Oscillators*, in *Advances in Optical and Photonic Devices*, K.Y. Kim, Editor. 2010, InTech.
18. Oshman, M. and S. Harris, *Theory of Optical Parametric Oscillation Internal to the Laser Cavity.* IEEE Journal of Quantum Electronics, 1968. **4**(8): p. 491-502.
19. Stothard, D., I. Lindsay, and M. Dunn, *Continuous-wave pump-enhanced optical parametric oscillator with ring resonator for wide and continuous tuning of single-frequency radiation.* Optics Express, 2004. **12**(3): p. 502-511.

20. Stothard, D.J.M., M. Ebrahimzadeh, and M.H. Dunn, *Low-pump-threshold continuous-wave singly resonant optical parametric oscillator.* Optics Letters, 1998. **23**(24): p. 1895-1897.
21. Stothard, D.J.M., et al. *Compact, All Solid-State, High Repetition Rate Intracavity Optical Parametric Oscillator and its application to the Spectroscopic Imaging of Gases and Liquids*. in *Conference on Lasers and Electro-Optics, 2007. CLEO 2007.* 2007.
22. Caird, J.A., et al., *Quantum Electronic Properties of the $Na_3Ga_2LiF_{12}:Cr^{3+}$ laser.* IEEE Journal of Quantum Electronics, 1988. **24**(6): p. 1077-1099.
23. Findlay, D. and R. Clay, *The Measurement of Internal Losses in 4-level Lasers.* Physics Letters, 1966. **20**(3): p. 277-278.
24. Zhao, H. and A. Major, *Dynamic Characterization of Intracavity Losses in Broadband Quasi-three-level Lasers.* Optics Express, 2014. **22**(22): p. 26651-26658.
25. Vodopyanov, K.L., et al., *Optical Parametric Oscillation in Quasi-phase-matched GaAs.* Optics Letters, 2004. **29**(16): p. 1912-1914.
26. Stothard, D.J.M., C.F. Rae, and M.H. Dunn, *An Intracavity Optical Parametric Oscillator With Very High Repetition Rate and Broad Tunability Based Upon Room Temperature Periodically Poled MgO:$LiNbO_3$ With Fanned Grating Design.* IEEE Journal of Quantum Electronics, 2009. **45**(3): p. 256-263.
27. Debuisschert, T., et al., *Intracavity Optical Parametric Oscillator: Study of the Dynamics in Pulsed Regime.* Journal of the Optical Society of America B, 1996. **13**(7): p. 1569-1587.
28. Preuss, D.R. and J.L. Gole, *Three-stage Birefringent Filter Tuning Smoothly over the Visible Region: Theoretical Treatment and Experimental Design.* Applied Optics, 1980. **19**(5): p. 702-710.
29. Svelto, O., *Principles of Lasers*. 2010: Springer.

Chapter 4
GaSb Semiconductor Disk Laser Pumped CW-ICOPO Based on OP-GaAs Sample 25B

4.1 Introduction

After the successful demonstration of a Tm^{3+}:YAP pumped pulsed ICOPO based on OP-GaAs in the previous chapter, the next challenge which presented itself was the construction of a continuous wave intracavity OPO based upon the same non-linear material, which shall be covered in this chapter. Continuous wave OPO devices present several distinct advantages and disadvantages over their pulse pumped counterparts, these include the potential for narrower linewidth operation in the continuous wave regime, balanced against the ease of reaching threshold and detection advantages offered by the pulsed regime. As discussed in chapter 2, continuous wave intracavity parametric oscillators are highly susceptible to prolonged and erratic relaxation oscillations when implemented with a long upper state lifetime laser [1-4]. This precludes the use of Tm^{3+}:YAP as a suitable pump laser for an ICOPO in the intracavity regime. Tm^{3+}:YAP's long upper state lifetime of 4.4 ms, as discussed previously in chapter 3, is orders of magnitude larger than the photon cavity lifetime, which is on the order of ns [5-9]. With an upper state lifetime in the order of nanoseconds and a wavelength of laser operation in the 2 μm region, GaSb semiconductor disk lasers provide the ideal platform for a continuous wave intracavity optical parametric oscillator based on OP-GaAs [3, 10-12].

The GaSb sample implemented in this chapter was cleaved from wafer number II 3491 which was supplied by the Fraunhofer Centre for Applied Solid-State Physics (Fraunhofer-IAF). This wafer was originally supplied for, and implemented in, the VERTIGO EU project, and bonded to a 250 μm diamond heat-

spreader by M Squared Lasers Ltd. using their proprietary bonding process. The SDL device structure itself was 10 μm thick (not including substrate) and was grown monolithically using molecular beam epitaxy on a 2" GaSb wafer. The Bragg mirror consisted of a 22.5 $AlAs_{0.08}Sb_{0.92}$/GaSb pairs with R>99.5 % and a stop band centred on 1.95 μm. The active region comprised $Al_{0.30}Ga_{0.70}As_{0.02}Sb_{0.98}$ barriers and ten compressively strained (~1.3 %) 10 μm thick $Ga_{0.74}In_{0.26}Sb$ quantum wells. $Al_{0.85}Ga_{0.15}As_{0.068}Sb_{0.932}$ was used as the window layer. This particular quantum well structure provides enhanced hole confinement and reduced temperature sensitivity compared to using more typical GaSb barriers [13]. The compressive strain enhances the carrier confinement and reduces the available density of states at the valence band edge. This leads to a reduction in the carrier density required for transparency, thereby reducing the pump power required for reaching threshold as well as an increase in the differential gain. The quantum wells were distributed in the active region over the six antinodes of the intracavity optical field in the standard resonant periodic gain (RPG) configuration [14]. The room temperature emission of the quantum wells was blueshifted with respect to both the microcavity resonance (between the DBR and the device surface) and the resonant periodic gain position. This compensates for device heating and maximizes the high power performance. The structure was finally capped with a 10 nm GaSb layer to mitigate surface oxidation [11].

In this chapter the above sample will be characterised and its potential for use in an OP-GaAs based ICOPO utilising sample 25B (see chapter 3) shall be modelled and discussed. A design for an ICOPO based on this SDL device shall be put forward and the results and conclusions obtained from its construction shall be presented.

4.2 SDL Performance Characterisation

The SDL chip used in this work was originally used in the VERTIGO project several years before and had been bonded to a 250 μm piece of unwedged, uncoated diamond in-house via capillary bonding and had shown exceptional

performance [11]. With M Squared Laser Ltd (M2) collaborating in this project, their proprietary bonding technique was applied to the sample and the performance compared with our own in house capillary bonding techniques. The bonded SDL chip is shown in figure 4.1. The experiment was setup as shown in figure 4.2.

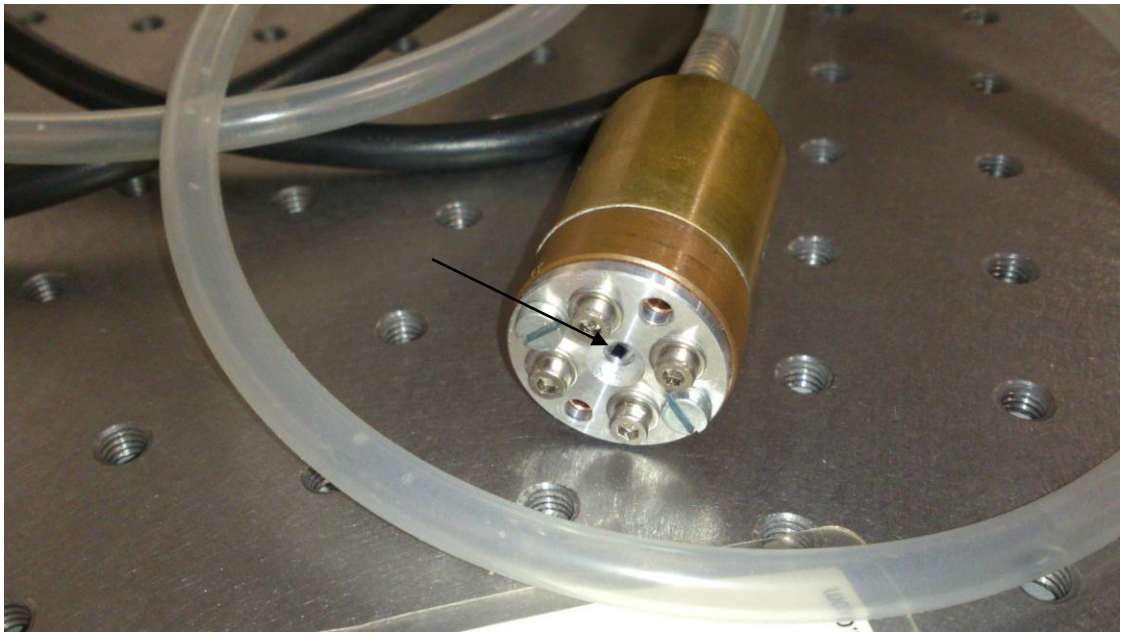

Figure 4.1 The SDL chip (centre, indicated by the arrow) bonded to diamond and housed in a copper and steel mount by M2 lasers limited, which was then bonded to a brass water cooled mount.

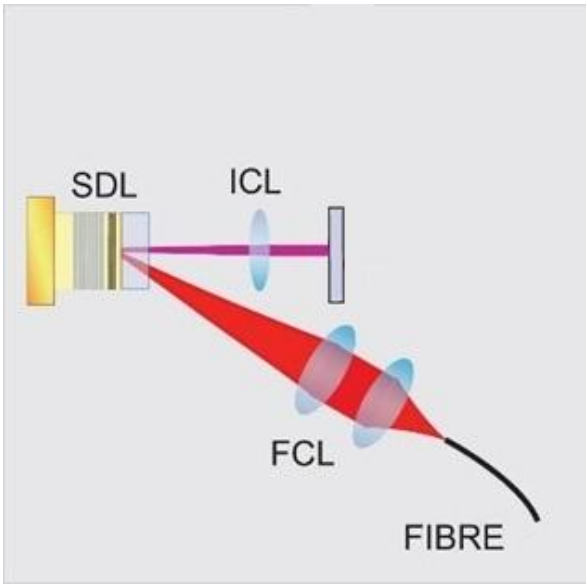

Figure 4.2 A schematic of the set up used to investigate the performance of the M2 squared bonded SDL material. Lenses FCL represent a pair of lenses which reimage the fibre tip onto the SDL while intracavity lens (ICL) was used to stabilise the cavity.

The SDL chip was placed into a cavity containing a single intracavity lens (AR coated at 2 μm, focal length 75 mm) to stabilise the laser and a 10% output coupler and pumped at 973 nm by a 105 μm-core-diameter fibre-coupled diode laser whose tip was reimaged onto the chip, to compare the new bonding technique against the optimal performance of the old bonding technique. The laser was water cooled to 15 degrees centigrade and a power transfer was obtained. This is shown in figure 4.3, alongside the data obtained from the in-house bonding method during the VERTIGO project.

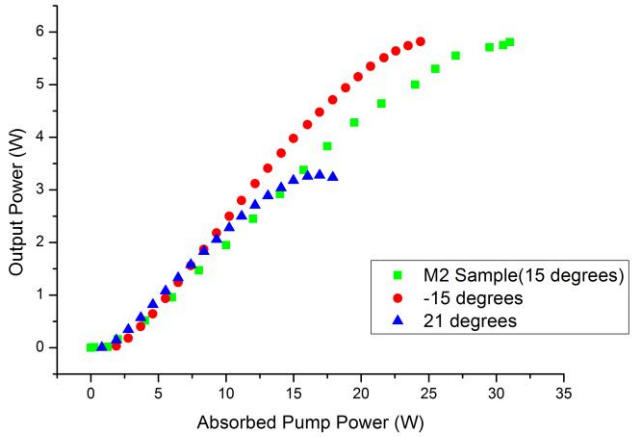

Figure 4.3 A comparison between the power transfer obtained from the M2 proprietary bonding process and the in house capillary bonding technique. The M2 bonded sample shows comparable performance to an in-house bonded sample cooled to -15 degrees

From figure 4.3 it is possible to see that the M2 bonding approach gives comparable performance at 15 degrees centigrade to the in-house bonding approach at -15 degrees centigrade, both reaching a maximum output power of 5.82 W and corresponding to 58.2 W of intracavity power, and clearly offers superior performance to the in-house bonding method at room temperature. This is due to increased thermal extraction from the gain medium as a result of the new bonding process. This decreases the internal temperature of the device, and so raises the pump power required to heat the device such that the peak emission wavelength of the quantum wells and the microcavity resonance of the SDL are aligned. This in turn increases the pump power required to reach thermal

rollover and thus increases the maximum output power from the device (see chapter 2 for further explanation).

The tuning range of the SDL chip was then characterised, to evaluate whether or not it would overlap with the signal range of crystal 25B and the beamsplitter and mirror optics (see chapter 3). A 1 mm thick quartz birefringent filter was inserted into the cavity to allow for tuning of the SDL and a monochromator was used to determine the wavelength. The tuning range of the SDL is shown in figure 4.4.

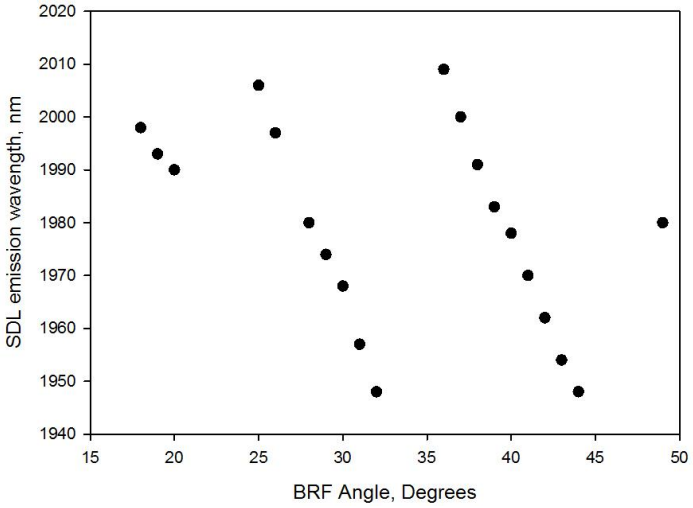

Figure 4.4 The tuning range of the SDL. The laser could be tuned smoothly using a birefringent filter (BRF) from 1945 nm to 2010 nm.

The SDL was found to tune through a range of 1945 nm to 2010 nm with the mounting cooled to 15 degrees centigrade, with the peak output power being obtained in the centre of the range at 1975 nm. This range is shorter in wavelength than the 1955 nm to 2025 nm range reported from the VERTIGO project at the same cooling temperature and is likely due to a decrease in the internal temperature due to the more effective heatsinking provided by the M2 proprietary bonding method, which would have shifted the peak emission wavelength of the quantum wells in the SDL (see chapter 2)

The coatings of the beamspllitter and mirror optics and the signal coating of 25B are shown again in figure 4.5 (see chapter 3 for further detail). From figure 4.5 it can be seen that the region in which the coatings best overlap is between 2020

nm and 2030 nm which is outwith the tuning range of the SDL. It must be stressed that the coatings on the crystal were not chosen for this application, but were inherited with the crystal from its owner. To examine the possibility of reaching threshold with the SDL at its optimum conditions, the threshold for the laser had to be modelled, which shall be presented in the next section.

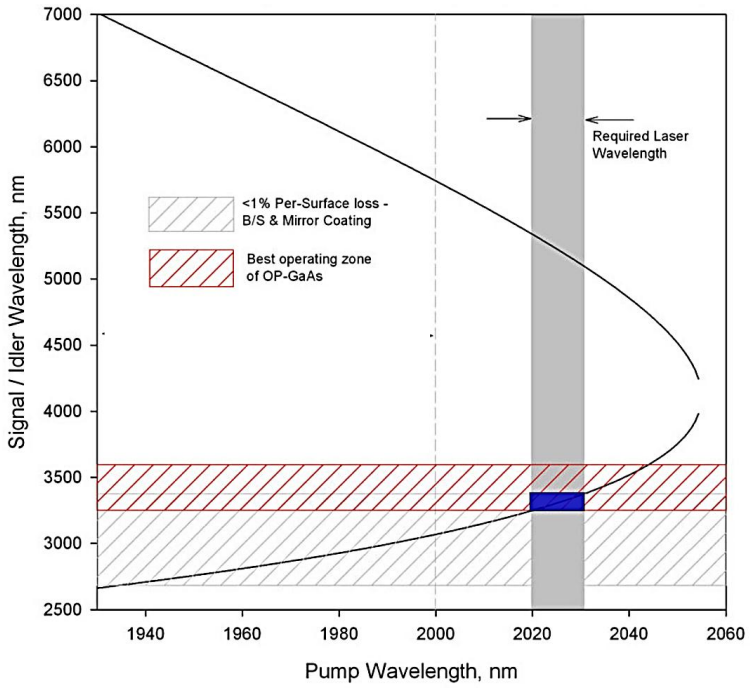

Figure 4.5 A diagram showing the lowest loss regions of the coatings on the OP-GaAs crystal (the red shaded area) and the beamspllitter and mirror optics (The light grey shaded area) overlaid with the phase matching curve of crystal 25B. Where all of these parameters overlap (indicated by the blue block) is the laser wavelength required for optimal operation of the ICOPO, which is shown as a grey bar on the figure.

4.3 Threshold Modelling of OP-GaAs in a CW-ICOPO

It was known from the work undertaken in chapter 3 what the signal coating losses of crystal 25B, as well as those of the beamsplitter and mirror optics used in the OPO cavity, were. The dimensions of crystal 25B were 1.4 mm x 6 mm x 16.8 mm with the quasi-phase matched region having a grating period of 60.5 μm. However, to model the threshold for the crystal, it was also crucial to know what the refractive index of the material would be for the pump, signal and idler wavelengths. To determine this, the Sellmeier equations for gallium arsenide were used. From the work of Skauli et al. [15] the Sellmeier coefficients were

determined to be g_0 = 5.372514, g_1 = 27.83972, g_2 = 0.031764 + 4.350 x 10^{-5} x ΔT + 4.664 x 10^{-7} x ΔT^2 and g_3 = 0.00143636. This can be substituted into Sellmeier's form of the equation to the determine the refractive index which has the form,

$$n(\lambda) = \sqrt{g_0 + \frac{g_1}{\lambda_1^2 - \lambda^2} + \frac{g_2}{\lambda_2^2 - \lambda^2} + \frac{g_3}{\lambda_3^2 - \lambda^2}} \ (equation\ 4.1)$$

Where λ_1 = 0.4431307 + 0.000050564 x ΔT, λ_2 = 0.8746453 + 0.0001913ΔT - 4.882 x $10^{-7}\Delta T^2$ and λ_3 = 36.9166 - 0.011622ΔT.

With the Sellmeier coefficients and equation now established, the threshold for oscillation can now be modelled. By taking equation 2.22 from chapter 2 and recasting it for angular frequency the threshold pump power of an intracavity OPO can be defined as,

$$P_{th} = \frac{\left(n(\lambda_p)n(\lambda_s)n(\lambda_i)\epsilon_0 c^3\right).\pi.\left[\psi_p^2 + \psi_s^2\right]}{4\omega_s\omega_i d_{eff}^2 l^2 h_m}\alpha_s \ (equation\ 4.2)$$

Where n(λ) is the refractive index for the pump, signal and idler, ε_0 is the permittivity of free space, c the speed of light in vacuum, ψ_s and ψ_p are the pump and signal mode radii (see equation 2.23 in chapter 2 for the confocal case), ω the signal and idler angular frequency, d_{eff} is the effective nonlinear coefficient (60 pm/V for quasi-phase matched OP-GaAs), l is the crystal length and h_m is the gain reduction factor which we assume to be equal to 1 for all subsequent modelling.

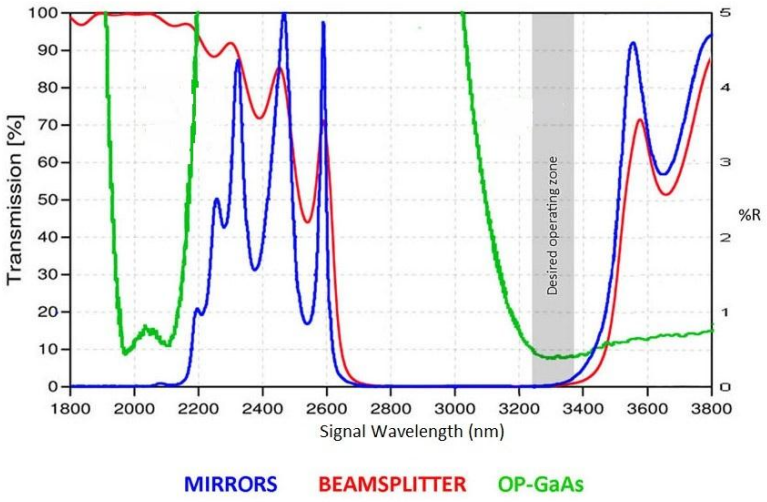

Figure 4.6 Coating transmission/reflection curves for the crystal, mirror and beamsplitter. The transmission of the mirrors and beam slitter corresponds to the left y axis, while the OP- GaAs reflectivity is indicated by the right y-axis. The grey bar shows the region of best overlap between the three.

For a pump wavelength of 1975 nm, which was the peak wavelength of operation for the SDL, the signal loss was ~60 % on a round trip, estimated from the data in figure 4.6. At this pump wavelength, the signal and idler were assumed to be 2900 nm and 6192 nm due to the phase matching condition. This gives refractive indices $n(\lambda_{pump}) = 3.34$, $n(\lambda_{signal}) = 3.314$ and $n(\lambda_{idler}) = 3.392$. For the cavity which had been modelled for implementation of the ICOPO, the spot size in the OP-GaAs was 54 μm (see section 4.4 for further detail). The temperature of the crystal, T, was assumed to be 22 degrees centigrade (room temperature). Under these conditions, the threshold intracavity power of the ICOPO device was 125 W. This value was considered prohibitively high for the operation of the OPO and thus a different strategy would have to be implemented. If one were to compare this to the threshold under optimal conditions, with a pump wavelength of 2025 nm, signal wavelength of 3315 nm and an idler wavelength of 5200 nm and a round trip loss of ~10 % (a conservative estimate, likely to push our estimated threshold above the actual threshold), the threshold intracavity power would be 20 W. If the SDL could be tuned to 2025 nm, then it would perhaps be possible to reach 20 W of intracavity power. In the next section a scheme for implementing an ICOPO device based on a GaSb SDL, alongwith a way of altering its tuning range during operation, shall be presented and the results derived discussed.

4.4 ICOPO Experimental Arrangement

An ICOPO arrangement was decided upon such that there was a collimated section for intracavity optics , such as a BRF, to be placed into as well a tight a focus within the crystal. The final cavity design is shown in figure 4.7. The SDL was pumped by a 973 nm diode laser which was coupled to a 105 μm core-diameter fibre whose tip was reimaged by a pair of collimating and focussing lenses. A pair of intracavity lenses (ICL) were used to create a collimated section in the cavity for inserting intracavity components while creating a tight focus inside the OP-GaAs crystal. The lens closest to the SDL had a focal length of 100 mm and was placed a distance of 97 mm from the SDL. The lens closest to the nonlinear crystal had a focal length of 75 mm and was placed 197 mm from the SDL. Both lenses were AR coated at 2 μm. The nonlinear crystal was inserted such that its centre was 278 mm away from the SDL.

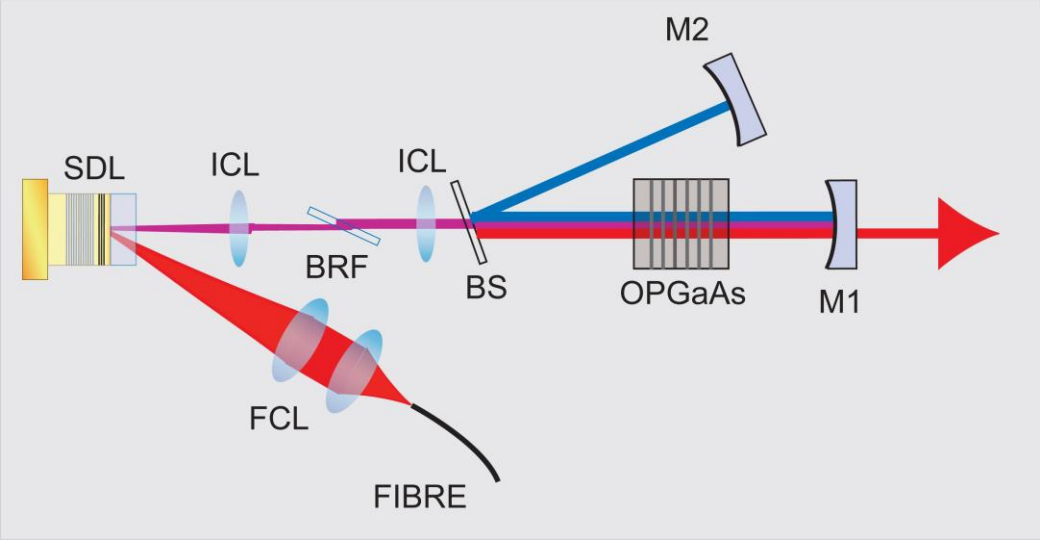

Figure 4.7 A schematic of the ICOPO design implemented to attempt the construction of a 2μm SDL pumped intracavity OPO based on OP-GaAs. The pump laser is collimated and focussed by the lenses FCL on the SDL. The intracavity lenses ICL from a collimated section in the pump cavity to insert the birefringent filter (BRF) then bring the beam to a focus in the OP-GaAs crystal. A beam splitter (BS) is used to separate the pump and signal cavities while mirrors M1 and M2 complete the pump and signal cavities

The pump cavity was completed by placing a high reflecting mirror for the pump and signal wavelengths (M1, ROC= 75 mm) 382mm from the SDL. A birefringent

filter (BRF) (1 mm thick, crystal quartz) was placed into the collimated section of the laser cavity to allow for longitudinal mode selection in the cavity. A beamsplitter (BS), which was antireflection coated at the pump wavelength on both sides and highly reflecting for the signal on one side for an insertion angle of 22.5 degrees to the beam (45 degrees deflection angle), was inserted into the cavity to separate out the pump and signal cavity arms. A second mirror which was highly reflecting at the signal wavelength (M2, ROC = 75mm) was placed facing the beamsplitter to complete the signal cavity. A photograph of the setup is shown in figure 4.8 and a diagram of the intracavity field radii within the pump cavity is shown in figure 4.9.

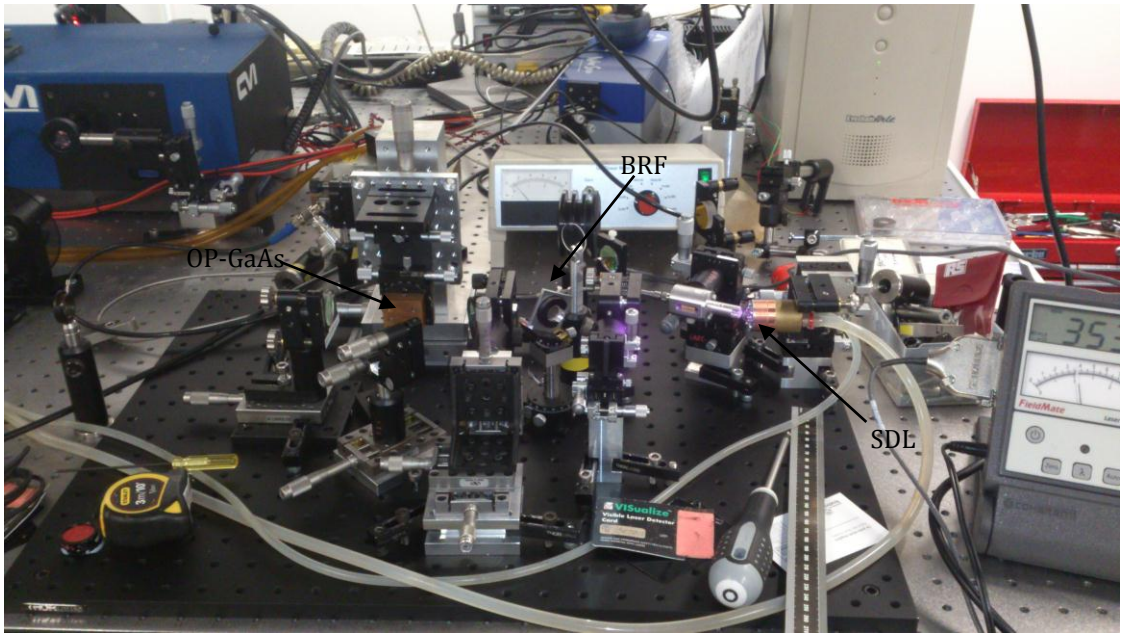

Figure 4.8. A photograph of the final setup for the investigations undertaken in this chapter. The SDL, BRF and OP-GaAs crystal are highlighted on the photograph for clarity.

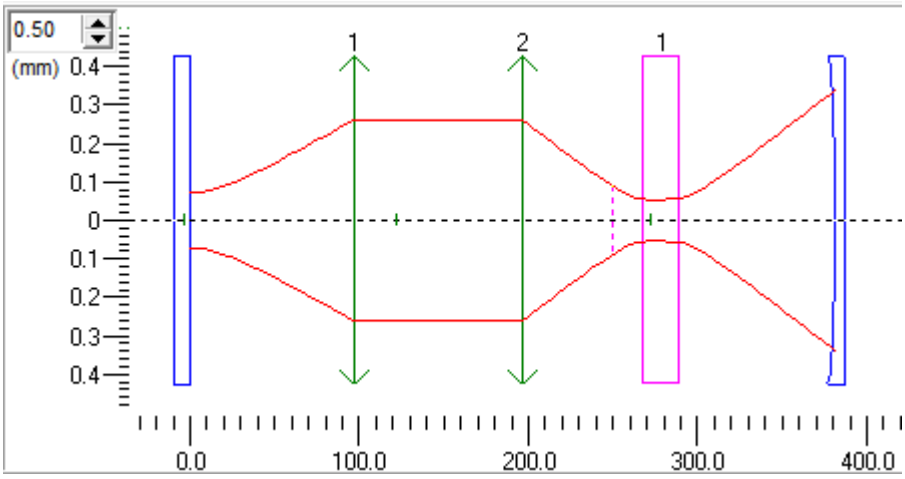

Figure 4.9 A diagram showing the evolution of the mode radius of the intracavity field in the SDL ICOPO cavity. The blue shapes represent mirrors, the green arrows lenses and the purple block a region of differing refractive index, in this case the OP-GaAs crystal (n = 3.4). The red trace shows the intracavity field.

The mode size of the diode pump spot was mode matched at 148 μm in diameter to the pump (optimal performance being achieved with the focus of the pump being placed slightly outside the chip for reasons of thermal management). The mode radius in the collimated section was 260 μm (520 μm in diameter) which was small enough to pass through the birefringent filter. The mode radius in the crystal was 54 μm, which while tight, still gives a suitable Rayleigh range (9.2 mm) to prevent clipping of the beam in the crystal for the given spot size at the focus in the crystal.

While ~100 W of intracavity field was demonstrated at the peak operating wavelength of the SDL with the OP-GaAs crystal in the cavity, this still fell short of the intracavity power required to reach threshold with the OPO and so threshold was not achieved. Thus, the next challenge which had to be solved was how to shift the gain bandwidth of the SDL such that it would operate at a wavelength of ~2025 nm. This was achieved by raising the SDL mount temperature higher than the 15 degrees to which it had originally been cooled. By raising the temperature to which the mount is cooled, the internal temperature of the SDL chip is increased for a given absorbed pump power. This in turn alters both the resonant periodic gain within the SDL microcavity, shifting it to longer wavelengths, as well as increasing the peak wavelength at which the quantum wells operate to longer wavelengths as well – a process known as

temperature tuning. The rejected power from the birefringent filter in the cavity was redirected into a monochromator to measure the wavelength of the laser, while the temperature to which the mount was held was steadily increased. By heating the mount to 35 degrees centigrade, it was possible to shift the gain bandwidth of the SDL to encompass 2025 nm. The intracavity field generated in the laser at this wavelength was 18 W for 40 W of incident pump power, just shy of the predicted threshold of 20 W. While pushing the temperature of the mount even higher may have allowed for 2025 nm to be the central operating wavelength of the laser, it was thought that the high internal temperatures under these conditions may have damaged the chip. This precluded operation of the OPO under the current circumstances, therefore another solution had to be sought for bringing the OPO to threshold. In the next section, conclusions which can be drawn from this chapter will be summarised and a scheme to lower the operating threshold of the OPO within the gain bandwidth of the SDL will be presented and discussed along with its implementation.

4.5 Conclusions

A GaSb based SDL chip cleaved from sample II 3491 was bonded to a 250 μm thick plane/plane diamond heatspreader by M2 laser limited using their proprietary bonding technique. The performance of this novel and innovative bonding technique was compared with regular capillary bonding techniques which had been performed in house on the same sample. The new bonding technique showed equal performance at 15 degrees centigrade to the more traditional capillary bonding technique at -15 degrees centigrade, both achieving a maximum output power of 5.82 W from a 10 % output coupler. This showed good potential for intracavity frequency conversion in the laser as this corresponded to an intracavity field of 58.2W with a relatively high loss in the cavity of 10 %. The new bonding technique also altered the tuning range of the laser, shifting it from 1955 nm to 2025 nm to 1945 nm to 2010 nm at 15 degrees centigrade. High signal losses in the cavity phase matched with the peak operating wavelength of the SDL rendered attempts to construct an ICOPO in this wavelength range

impractical, and so the sample was cooled to a higher temperature of 35 degrees to redshift the gain bandwidth of the laser to the lowest loss region of the signal coating where the threshold was ~20 W. While this did lead to a shift of the gain bandwidth to encompass the optimum (lowest-loss) range of the signal coating, the much reduced gain and efficiency of the device (18 W of intracavity power being the peak intracavity field generated) precluded operation of the OPO. Ultimately, with the non-optimal, inherited coatings upon the OP-GaAs, it was never going to feasible to bring the ICOPO to threshold with the semiconductor material which was implemented.

To have the best chance of bringing the OPO to threshold with the gain material available, it was concluded that our best option was to have to OP-GaAs crystal (25B) recoated such that the losses at the signal wavelength due to the AR coating on the crystal were minimised in the region which phase-matched with the gain bandwidth of the SDL when chilled to 15 degrees centigrade. The transmission of the current signal coating is shown in figure 4.10.

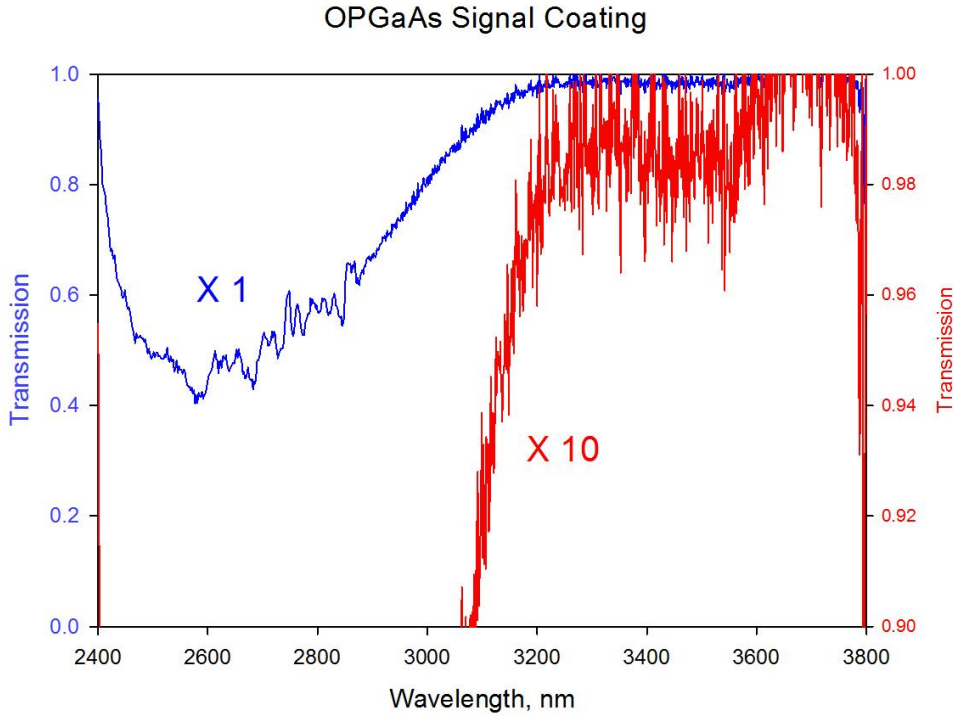

Figure 4.10. A transmission spectrum of the current coating of crystal 25B in the signal wavelength range, with the red trace being a 10 x zoom of the blue trace. The crystal only shows ultra-low losses above 3200 nm.

Phase matching curves were calculated using the freely available SNLO software package, with a diagram of the phase matching curve with the gain bandwidth of the laser overlaid being shown in figure 4.11. This was then used to determine what the signal coating range on the crystal should be recoated. This was chosen to be, after some negotiation with the coating company to about optimising the coating performance, R<0.25 % @ 1940 to 1980 nm, R<0.1 % @ 2700 to 2940 nm, R<5 % @ 6100 to 6840 nm. Emphasis was placed on optimising the coating performance at the signal wavelength range as the performance of the ICOPO is most sensitive to this parameter. In the next chapter the characterisation and construction of an ICOPO with the newly recoated crystal shall be presented along with any results and conclusions from this endeavour, which shall then be discussed.

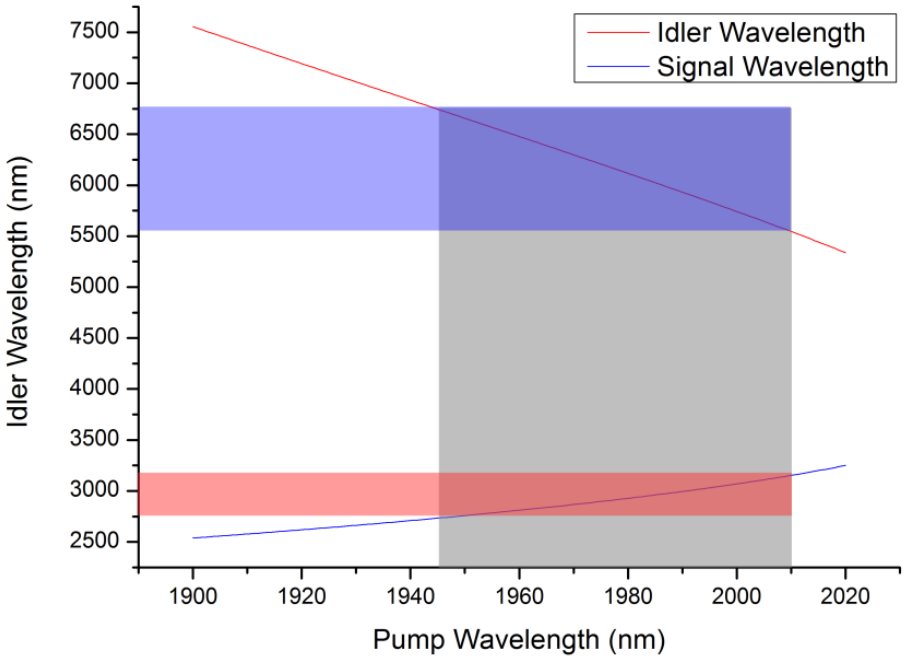

Figure 4.11 A phase matching diagram for an OP-GaAs crystal with a quasi-phase matching period of 60.5 µm. The gain bandwidth of the SDL material used in this chapter is overlaid on the diagram as a transparent grey quadrilateral spanning 1945 nm to 2010 nm. The signal region this phase matches to is shown by the red quadrilateral, which spans the range 2750 nm to 3250 nm, and the idler range is shown in blue and spans a range of ~5500 nm to 6750 nm.

4.6 References

1. Stothard, D.J.M., *Practical Continuous Wave Optical Parametric Oscillators*, in *Advances in Optical and Photonic Devices*, K.Y. Kim, Editor. 2010, InTech.
2. Stothard, D.J.M. and M.H. Dunn, *Relaxation Oscillation Suppression in Continuous-wave Intracavity Optical Parametric Oscillators.* Optics Express, 2010. **18**(2): p. 1336-1348.
3. Stothard, D.J.M., et al., *Stable, Continuous-wave, Intracavity, Optical Parametric Oscillator Pumped by a Semiconductor Disk Laser (VECSEL).* Optics Express, 2009. **17**(13): p. 10648-10658.
4. Turnbull, G.A., et al., *Transient Dynamics of CW Intracavity Singly Resonant Optical Parametric Oscillators.* IEEE Journal of Quantum Electronics, 1999. **35**(11): p. 1666-1672.
5. Cemy, P. and D. Burns, *Modeling and Experimental Investigation of a Diode-pumped Tm:$YAlO_3$ Laser with a- and b-cut Crystal Orientations.* IEEE Journal of Selected Topics in Quantum Electronics, 2005. **11**(3): p. 674-681.
6. Cerny, P., G.J. Valentine, and D. Burns, *Actively Stabilised Diode Pumped Tm:YAlO Laser.* Electronics Letters, 2004. **40**(17): p. 1061-1063.
7. Elder, I.F. and J. Payne, *Diode-pumped, Room-temperature Tm:YAP Laser.* Applied Optics, 1997. **36**(33): p. 8606-8610.
8. Stoneman, R.C. and L. Esterowitz, *Efficient 1.94 μm Tm:YALO Laser.* IEEE Journal of Selected Topics in Quantum Electronics, 1995. **1**(1): p. 78-81.
9. Weber, M.J., et al., *Czochralski Growth and Properties of $YAlO_3$ Laser Crystals.* Applied Physics Letters, 1969. **15**(10): p. 342-345.
10. *Semiconductor Disk Lasers: Physics and Technology*. 2010: John Wiley and Sons.
11. Hopkins, J.M., et al., *High-power, (AlGaIn)(AsSb) Semiconductor Disk Laser at 2.0 μm.* Optics Letters, 2008. **33**(2): p. 201-203.
12. Hopkins, J.M., et al., *Tunable, Single-frequency, Diode-pumped 2.3μm VECSEL.* Optics Express, 2007. **15**(13): p. 8212-8217.
13. Härkönen, A., et al., *1 W Antimonide-based Vertical External Cavity Surface Emitting Laser Operating at 2 μm.* Optics Express, 2006. **14**(14): p. 6479-6484.
14. Corzine, S.W., et al., *Efficient, Narrow-linewidth Distributed-Bragg-reflector Surface-emitting Laser with Periodic Gain.* IEEE Photonics Technology Letters, 1989. **1**(3): p. 52-54.
15. Skauli, T., et al., *Improved Dispersion Relations for GaAs and Applications to Nonlinear Optics.* Journal of Applied Physics, 2003. **94**(10): p. 6447-6455.

Chapter 5
GaSb Semiconductor Disk Laser Pumped CW-ICOPO Based on OP-GaAs – Crystals 25E, 60E1 and 60F1

5.1 Introduction

In the previous chapter the characterisation and results from the attempt to construct an SDL ICOPO out of an SDL sample from wafer II 3491 and OP-GaAs crystal 25B were presented. Laser operation with the crystal in the cavity was achieved but the OPO could not be brought to threshold. This was due to the high signal loss in the phase matching range of the crystal accessed by the SDL tuning range, which raised the threshold of operation above the powers that could be achieved with the SDL sample. Even heating the crystal could not shift the gain bandwidth of the SDL enough to sufficiently pump the crystal where it had low signal loss. It was concluded that recoating the crystal for optimal operation with the SDL gain chip would be the best way to implement the ICOPO successfully.

A coating company was contacted in the US (Twinstar Inc.) to have the OP-GaAs polished and recoated such that the signal loss was minimised in the region which phase matched with the gain bandwidth of the SDL. Unfortunately, the crystal snapped during the polishing process and was broken into three pieces, as shown in figure 5.1. The crystal snapped into one piece 10 mm long, one piece 5 mm long and 1 piece 1mm long. The short piece (1 mm long) was discounted for cw-ICOPO operation due to the prohibitively high threshold from the low gain due to the short interaction length. The medium piece and long piece were returned to the coating company in the US again for recoating.

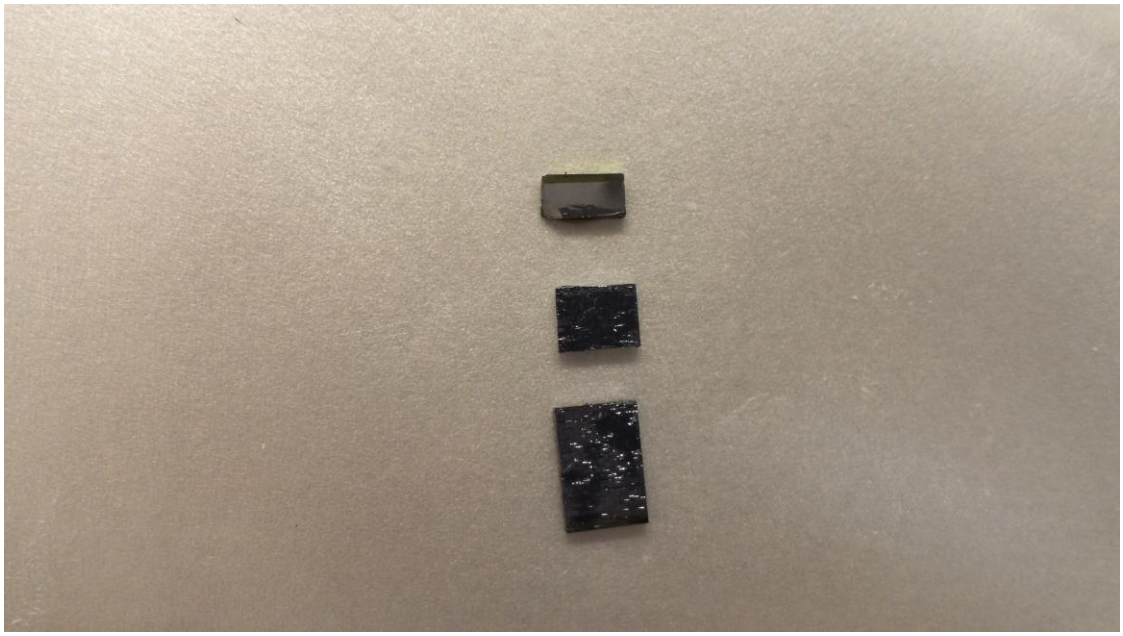

Figure 5.1 The remnants of crystal 25B after it had been broken during polishing. The crystal had snapped into three pieces. One piece about 10mm long, one piece about 5 mm long and piece about 1 mm long. The 1 mm piece was too short to be of practical use. The 5 mm piece was polished and coated with the new coating. The 10 mm piece contained a defect generated when the crystal snapped in polishing which caused the crystal to fail when polished again.

The large piece (10 mm long) was fundamentally damaged when it snapped during the initial polishing process and, when repolished, the defect propagated throughout the crystal fragment causing it to fail entirely. The medium piece (5 mm long) was successfully polished and recoated. The repolished piece was found to have a transmission loss of ~15 % on a single pass, and so was discounted for practical use as this is more than the SDL devices could tolerate.

A new set of beamsplitter and mirror optics were also ordered from Twinstar Inc., alongside a GaAs witness piece to test the coatings for the OP-GaAs, to match the new operating wavelengths of the OPO. Modelled transmission and reflection curves are shown for the beamsplitter, mirror and witness piece in figures 5.2, 5.3 and 5.4. The components were received and their performance was tested. At first, they appeared to match our requirements, with transmission of 100 % (our instruments could at least discern no loss) in the pump for the beamsplitter while the mirror was 100 % reflecting. The GaAs witness piece was also shown to be 100 % transmitting at the pump wavelength.

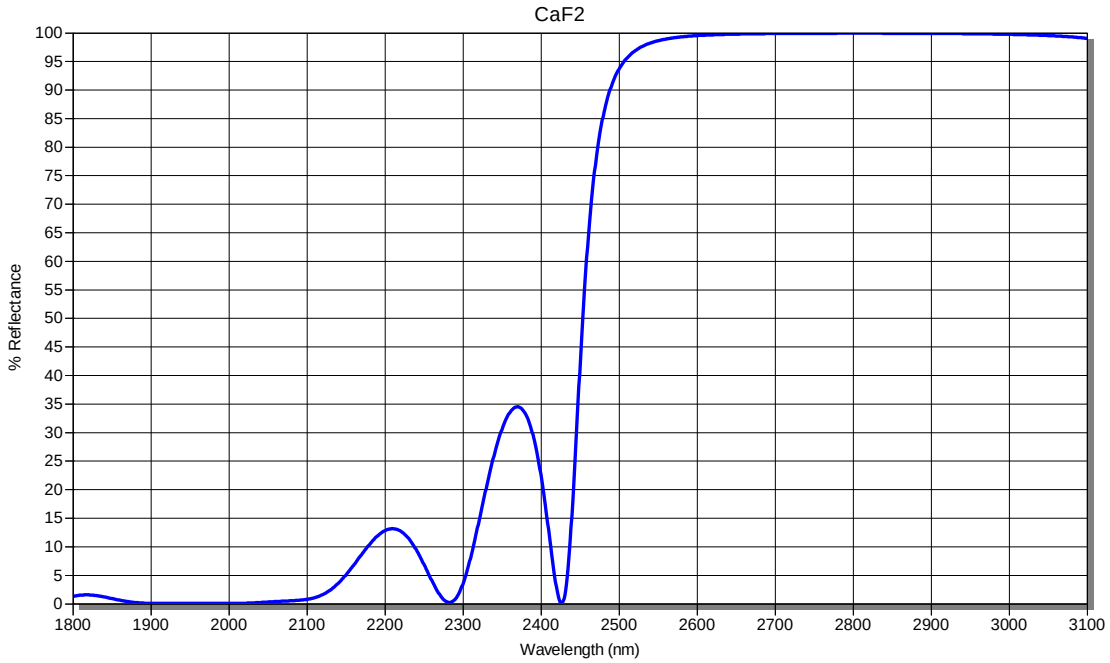

Figure 5.2 A modelled curve for the reflectance of the beamsplitter coating ordered from TWINSTAR INC. The coating was specified to be 100 % reflecting in the signal waveband and 100 % transmitting in the pump waveband.

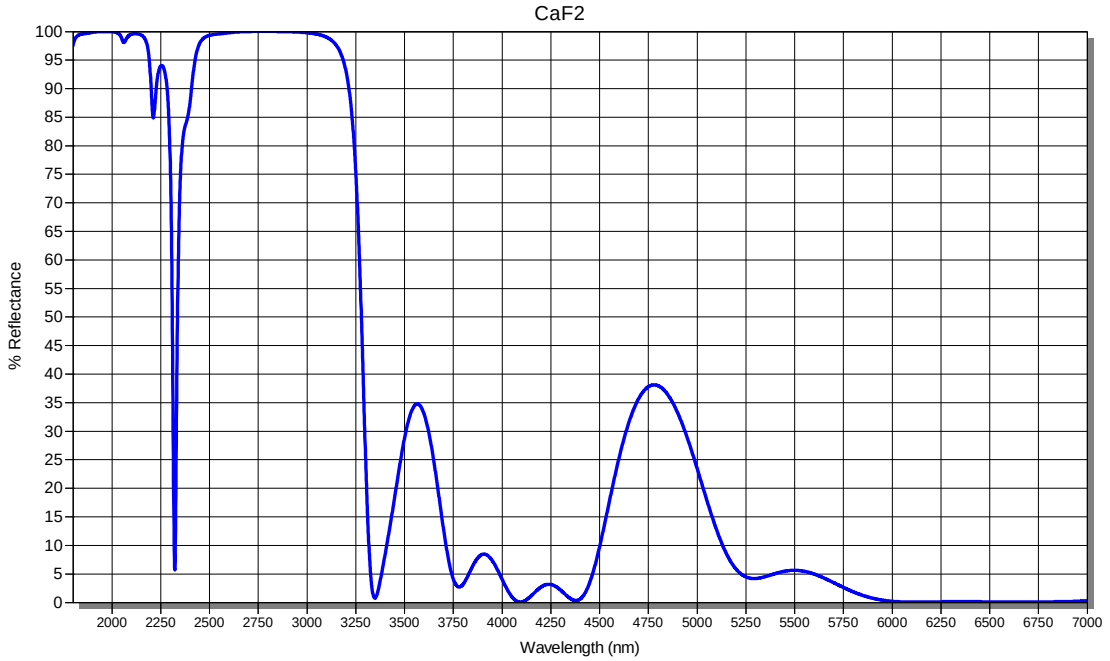

Figure 5.3 A modelled curve of the reflectance of the mirror coating ordered from TWINSTAR INC. The mirror was specified to be highly reflecting in the the pump and signal wavebands.

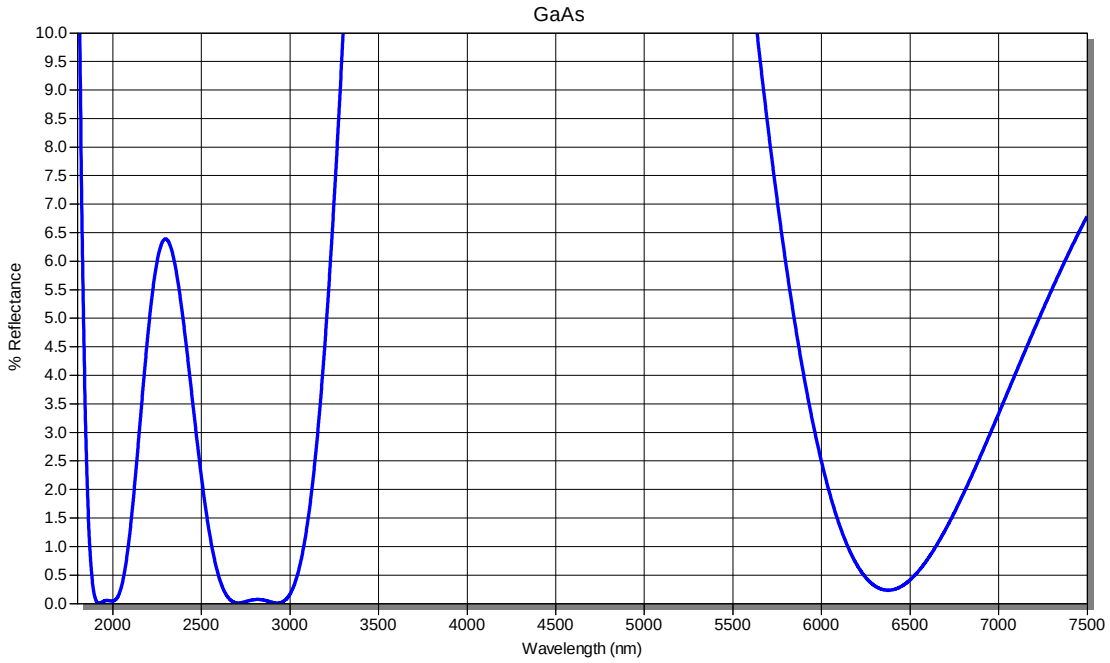

Figure 5.4 A modelled curve for the tri-band anti-reflection coating on the GaAs witness piece. The coating was specified to be highly reflecting in the pump and signal wave bands, but conditions were relaxed to being less than 5 % reflectance at the idler to allow for optimisation at the more vital signal waveband.

However, after leaving the optics for a day, the performance of the beamsplitter and the GaAs coating had degraded considerably. The GaAs transmission fell to ~93 % along with the beamsplitter transmission. It was suspected that the coatings may be hygroscopic in nature, and so an experiment was carried out to determine this. The GaAs witness piece and the beamsplitter were baked out at 60 degrees centigrade in a zero humidity atmosphere. Upon retesting the optics, the excellent performance was returned, however it once again degraded quickly over time leading to the conclusion that water was indeed seeping into the coatings. Twinstar inc. were contacted to determine a solution, and it was agreed that an extra 100 nm thick MgF_2 barrier would be placed over the current coatings to protect the layers underneath. This was undertaken and the resulting coatings showed consistent performance, further confirming that water absorption in the coatings was to blame for the drop in performance. Sadly, adding this extra barrier had shifted the operating wavelength bands of the coatings, rendering them no longer suitable for our application. There was no time or money left in the project to procure a new set of coatings and so it was resolved to use the old beamsplitter and mirror set (while the mirror showed no

degradation, confidence in the optics was not high after the previous travails) for the remaining work as they still had some overlap with our region of interest.

Three new crystals were sent by BAE systems as replacements for the now broken 25B as well as the previously retracted crystal 26K. These were samples 25E, 60E1 and 60F1 which had dimensions 25.7 mm x 8 mm x 1.2 mm for crystal 25E and 26 mm x 5 mm x 1.2 mm for crystals 60E1 and F1 and a grating period of 60.5 μm for all three crystals. The three crystals were sent to the same coating company and were successfully polished and recoated with a coating optimised for low loss at the signal range which phase matches for the gain bandwidth of the SDL, with an extra 100 nm of MgF_2 added after the lessons from the witness piece, beamsplitter and mirror optics. The theoreticals for the new coatings are shown in figures 5.5 and 5.6.

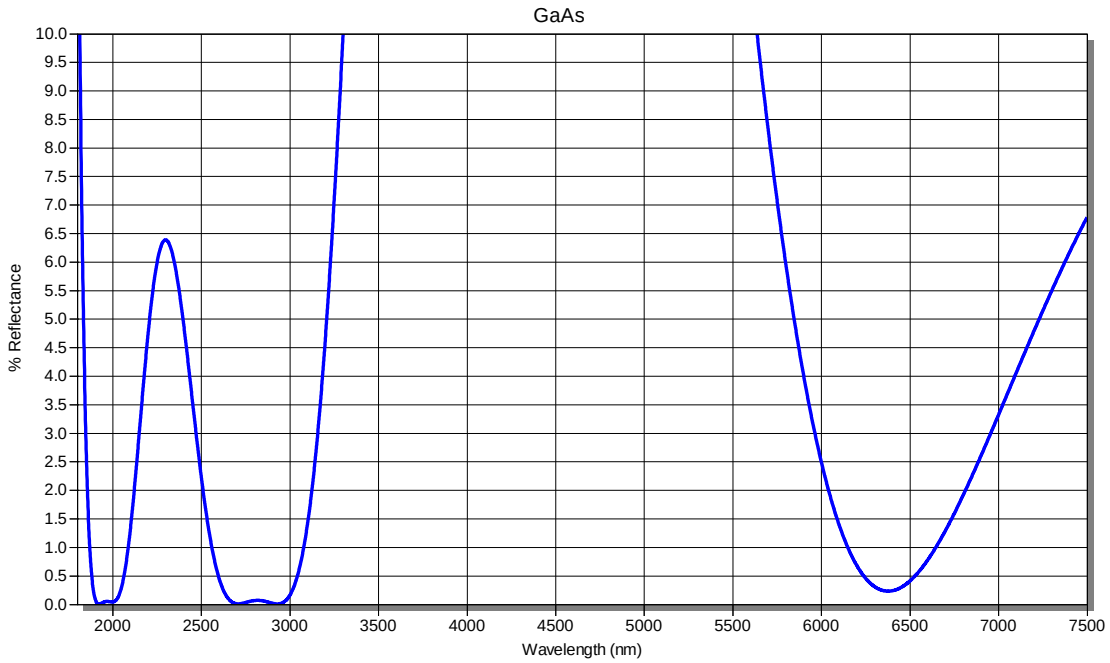

Figure 5.5 A modelled curve for the tri-band anti-reflection coating applied to crystals 25E, 60E1 and 60F1. The coating was specified to be anti-reflecting at the pump, signal and idler wavebands.

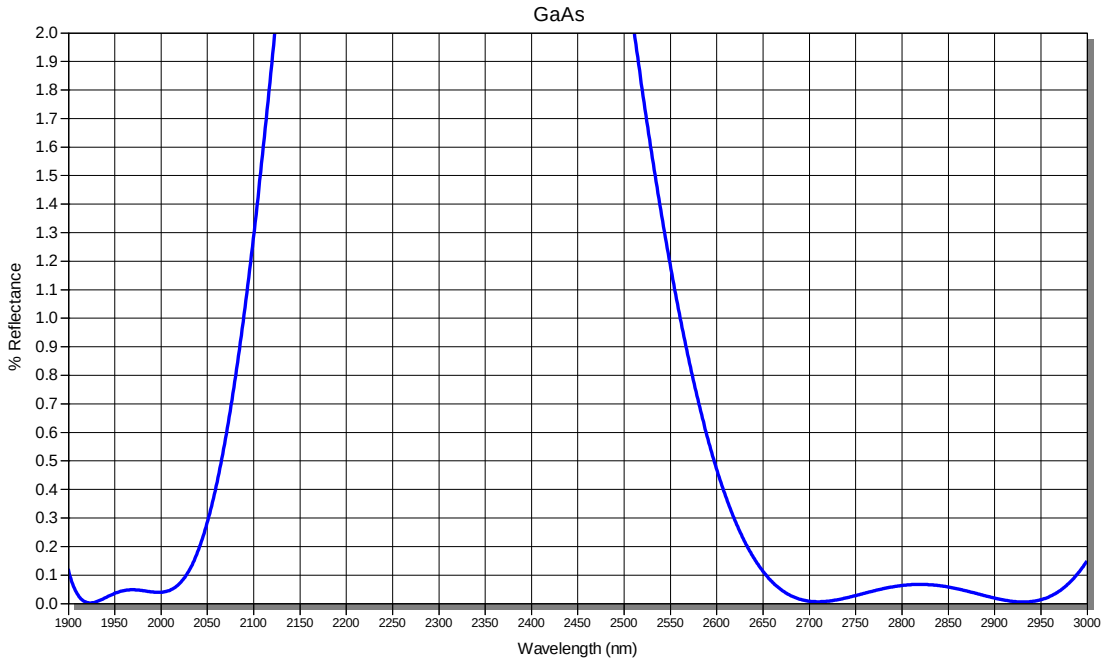

Figure 5.6 A modelled curve for the coating applied to crystals 25E, 60E1 and 60F1, which is zoomed in on the pump and signal region. It can be seen that the model predicted less than 0.1% reflection in the pump and signal region.

Before experimental work could begin, the SDL sample had been destroyed in a laboratory accident. A new SDL sample was cleaved from wafer II 3491 and given the label "G1" to catalogue which part of the wafer it had been taken from. This sample would have to be characterised before construction of the ICOPO began.

In this chapter the above samples will be characterised and their potential for use in an OP-GaAs based ICOPO shall be modelled and discussed. A design for an ICOPO based on this SDL device shall be put forward and the results and conclusions obtained from its construction shall be presented. The possible reasons for this device's failure to operate shall also be discussed.

5.2 SDL Performance Characterisation

The SDLs performance was characterised in the setup shown in figure 5.7.

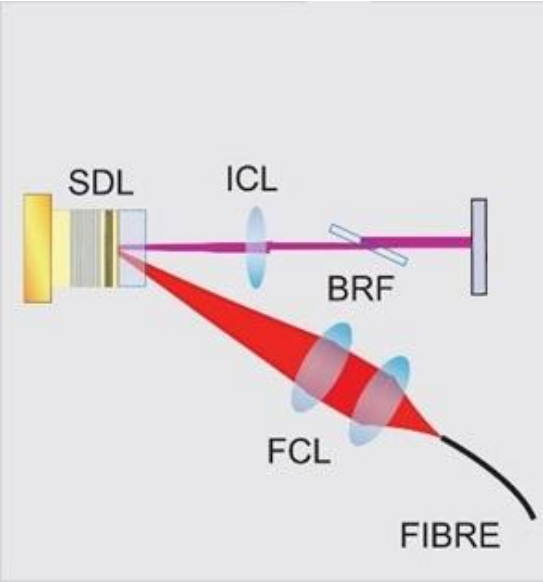

Figure 5.7 A diagram showing the setup used to characterise the GaSb SDL. The laser is pumped by a 980 nm diode laser with a 105 μm core-diameter fibre, whose tip is reimaged onto the SDL by a pair of lenses (FCL). An intracavity lens (ICL) with a focal length of 75 mm was inserted to stabilise the cavity. The cavity was terminated with a plane output coupler. A birefringent filter (BRF) was inserted when longitudinal mode selection was required.

The SDL was pumped by a DiLas fibre coupled diode laser emitting at 980 nm capable of outputting up to 40W. The fibre tip (105 μm in diameter) was reimaged onto the SDL gain chip by a pair of lenses (FCL). The spot size after the pair of lenses was determined by means of a series of knife edge measurements, with the results being shown in figure 5.8. The spot size upon reimaging the fibre was found to be 55 μm with a standard error of 9 μm. This gives a diameter of 110 μm with a standard error of 18 μm, which is in good agreement with the stated 105 μm diameter of the fibre. This information was then used to design a cavity with good mode matching between the pump and the cavity mode to achieve the best possible efficiency from the laser. After some initial experimentation, the final cavity design is depicted in figure 5.9 was settled upon, showing both the separation between components and the mode size throughout the cavity.

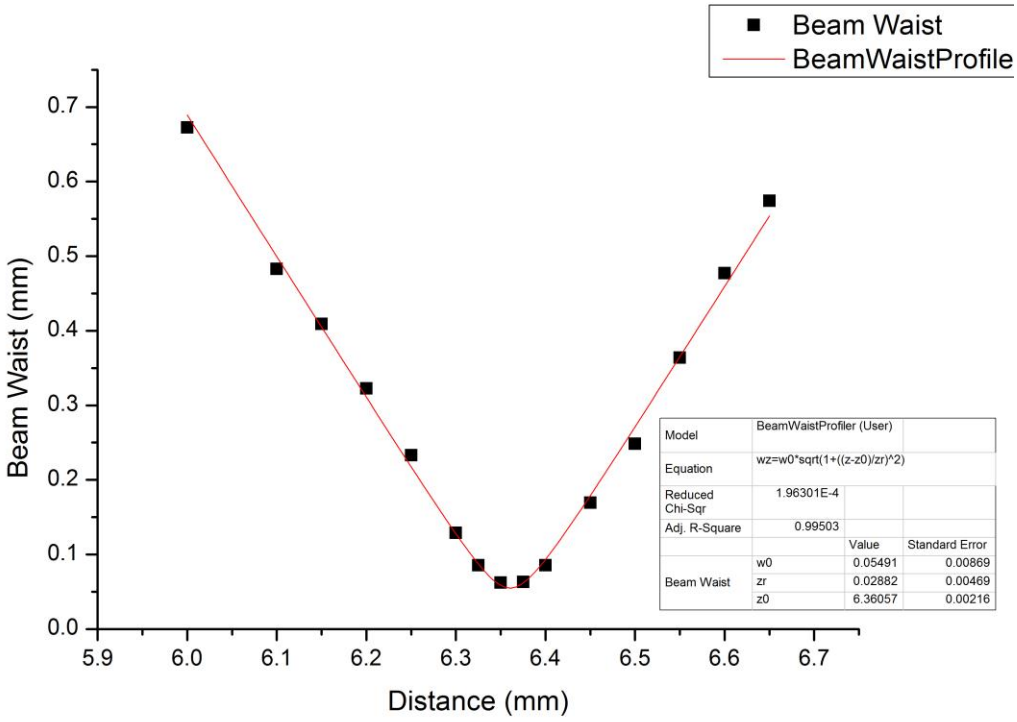

Figure 5.8 A plot of the data obtained by measuring the pump beam width close to the focus, with a Gaussian fit applied to the data to determine the spot size at the focus. The spot size was determined to be 55 µm with a standard error of 9 µm. This gives a diameter of 110 µm with a standard error of 18 µm, which is in good agreed with the stated 105 µm diameter of the fibre. Distances were measured from the flange at the output of the pump laser.

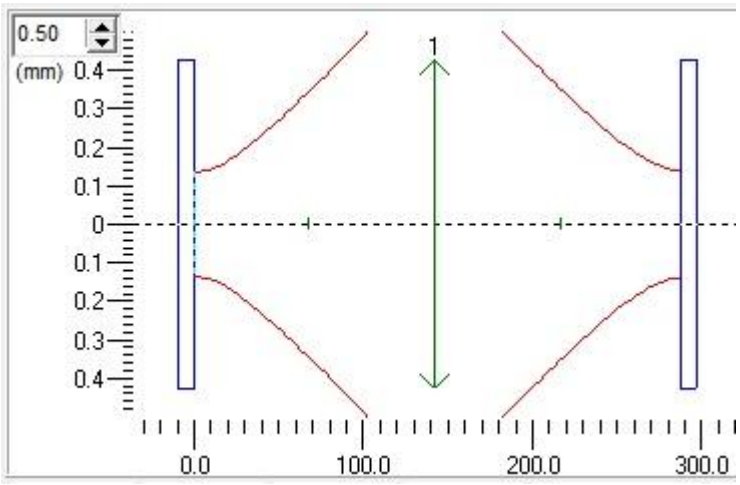

Figure 5.9 A schematic of the mode size and spacing throughout the cavity, generated through the Psst! program, which is distributed free through the university of St. Andrews website. The blue rectangles represent plane mirrors while the green double headed arrow represents a lens. All sizes are in mm.

The intracavity lens was separated from the SDL chip by a distance of 142 mm, with the end mirror being situated 288 mm away from the SDL chip, or 146 mm

from the intracavity lens. The laser mode spot radius on the chip was 136 μm. While this is not identically matched to the spot size of the pump laser, indeed it is approximately 2.5x larger, the highest performance is obtained here for a number of reasons. With the use of highly multi-mode pump lasers, the intensity distribution of the beam in space appears to be a tophat function at the focus. By moving away from the focus slightly, the intensity distribution becomes more gaussian, and is therefore better mode-matched to the cavity mode, improving power extraction. Another advantage is gained by choosing to place the focus closer to face of the chip where the heatspreader is, by pumping the laser closer to the heatspreader, better heat extraction can be achieved due to the heatspreader's superior thermal conductivity. This reduces the problems related to thermal issues such as thermal lensing in the gain medium. The birefringent filter shown in figure 5.7 was only inserted later on when longitudinal mode control was required.

Once a stable cavity had been constructed, a number of different output couplers were tried and power transfers obtained with the objective of ascertaining the optimal output coupling for the SDL. The data acquired is shown below in figure 5.10.

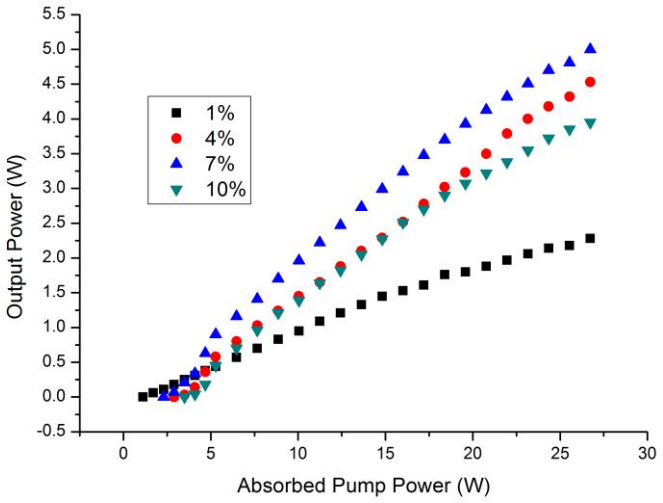

Figure 5.10 A power transfer characteristic for the SDL gain chip using a variety of output couplers (1 % (black squares), 4 %(red dots), 7 %(blue triangles) and 10 %(green inverted triangles)).

The peak output power achieved from the chip was 5 W with a 7 % output coupler when the cooling water was cooled to 15 degrees centigrade. From the data above it can be seen that the optimal output coupling from the laser was ~6 %. In the context of continuous wave intracavity nonlinear frequency conversion, the most important power characteristic to know is the intracavity power within the laser. The data from the above figure was converted into intracavity power and is displayed in figure 5.11.

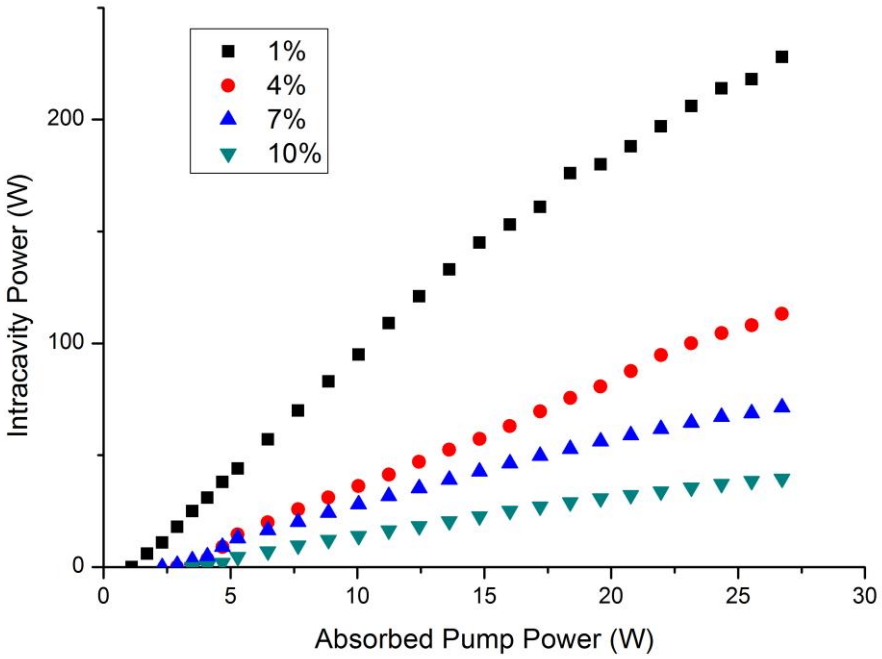

Figure 5.11 The intracavity power in the SDL cavity for a variety of output couplers. (1 % (black squares), 4 %(red dots), 7 %(blue triangles) and 10 %(green inverted triangles)).

From figure 5.11 it can be seen that intracavity powers of over 200 W were achievable from the SDL chip with a high finesse (1 % output coupling) cavity. This is a promisingly large intracavity field for intracavity nonlinear frequency conversion. Even after introducing a relatively large loss to the laser cavity (10 %), it was still possible to reach intracavity fields of up to 40 W, which is still suitably high enough for potential nonlinear frequency conversion. The threshold of operation for an ICOPO based on OP-GaAs shall be modelled and presented

later on in this chapter to give the reader a firmer idea of how these numbers relate to the potential for operation of an ICOPO device.

The next parameter of the pump laser which was characterised was the tuning range and maximum output power for each given wavelength. A 1 mm thick, quartz, birefringent filter was inserted into the cavity to achieve this. The birefringent filter, in combination with the etalon function of the 250 μm-thick diamond heatspreader placed on to the front of the SDL chip, produced smooth tunablity along with giving good longitudinal mode control, leading to narrow linewidth operation. The tuning curve of the laser is shown in figure 5.12.

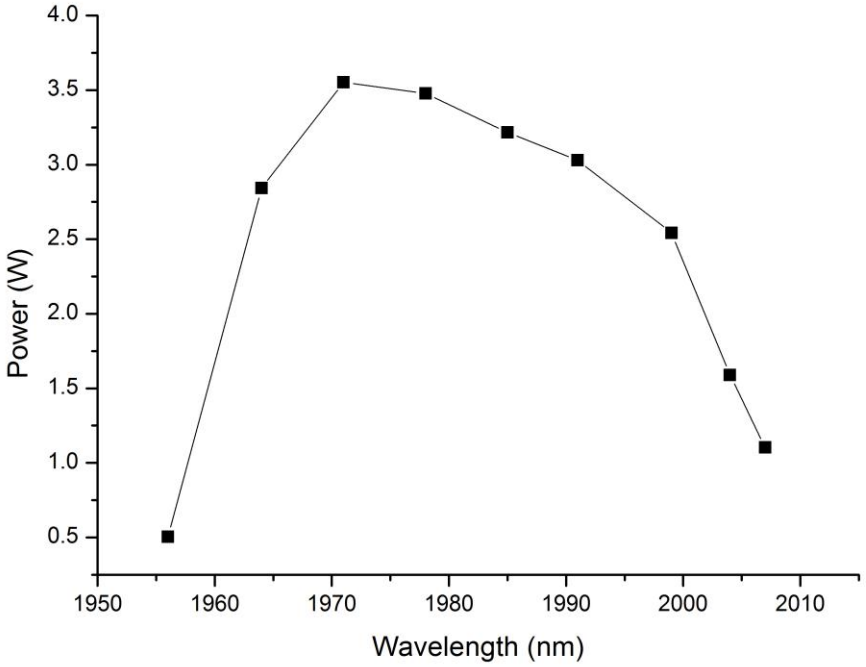

Figure 5.12 The tuning curve of the SDL with a 10% output coupler. The peak wavelength of operation is in the region of 1970nm, with the device tuning from approximately 1955nm to 2010nm.

The power spectrum of the SDL was obtained using a 10 % output coupler to simulate what was estimated to be the final losses in the OPO laser cavity with all of the necessary intracavity components added. The wavelength was measured using a Czerny-Turner style rotating grating spectrometer. From figure 5.12 it can be seen that the SDL chip tunes from about 1955 nm to 2010 nm when cooled

to a temperature of 15 degrees centigrade. The maximum output power of 3.5 W was obtained for a wavelength of operation in the region of 1970 nm.

With the phase matching bandwidth of OP-GaAs being known to be relatively narrow (~3 cm^{-1}) in comparison to more common OPO materials such as PPLN (see chapters 2 and 3) it was also important to know just how much intracavity power could be expected during single mode operation of the device and how narrow the linewidth of the laser in this condition is – would it be narrow enough to fit within the phase matching bandwidth of the OP-GaAs crystals samples?

A Fabry-Pérot interferometer (Thorlabs SA210-18B, 10 GHz FSR, 67 MHz resolution) was used to resolve the individual cavity modes and determine their linewidth. The resultant interferometer traces are shown in figures 5.13 and 5.14.

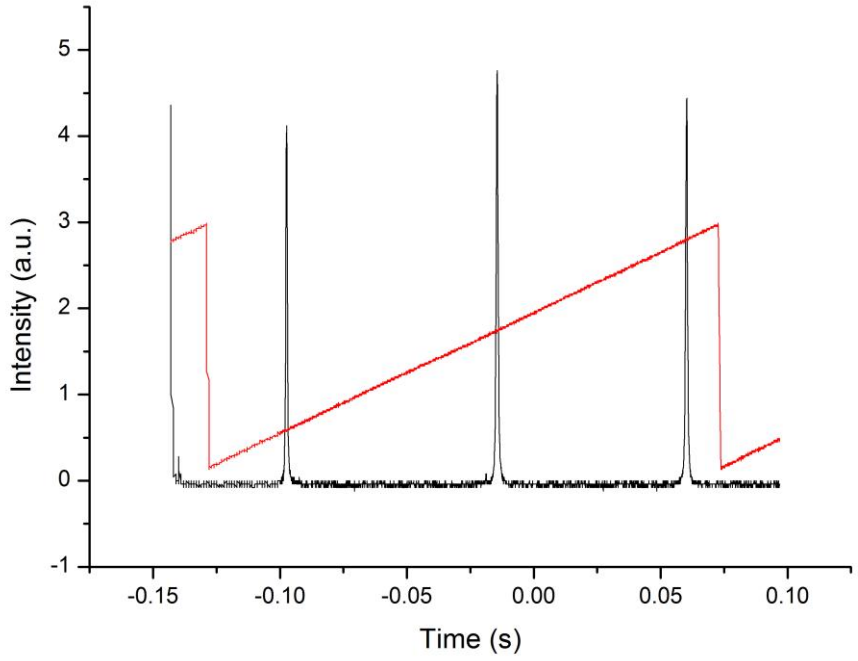

Figure 5.13 A trace showing multiple free spectral ranges of the interferometer (the black trace on the figure), indicating that the laser exhibits single frequency operation. The red trace on the figure represents the driving voltage applied to the piezo within the within the Fabry-Pérot interferometer.

Figure 5.13 shows multiple free spectral ranges of the interferometer. The interferometer had a FSR of 10 GHz, which translates into a separation in wavelength space of 0.13 nm. This was not enough to discriminate across the gain

bandwidth of the SDL if the laser output was truly single frequency. A spectrometer (APE Wavescan) was also implemented to the setup to eliminate the possibility of the laser running on two or more wavelengths. The spectrometer monitoring the laser output showed a single frequency emitted at a wavelength of 1971 nm. However, closer inspection of the interferometer output shown in figure 5.13 shows that, during some sweeps of the interferometer, a second peak was present on the shoulder on the trace, suggesting that the laser wasn't always running single frequency. However the magnitude of the parasitic laser frequency was much smaller than the dominant frequency, and thus the laser could be considered to be running approximately single frequency. A zoomed in image of a single peak form the interferometer trace is shown in figure 5.14.

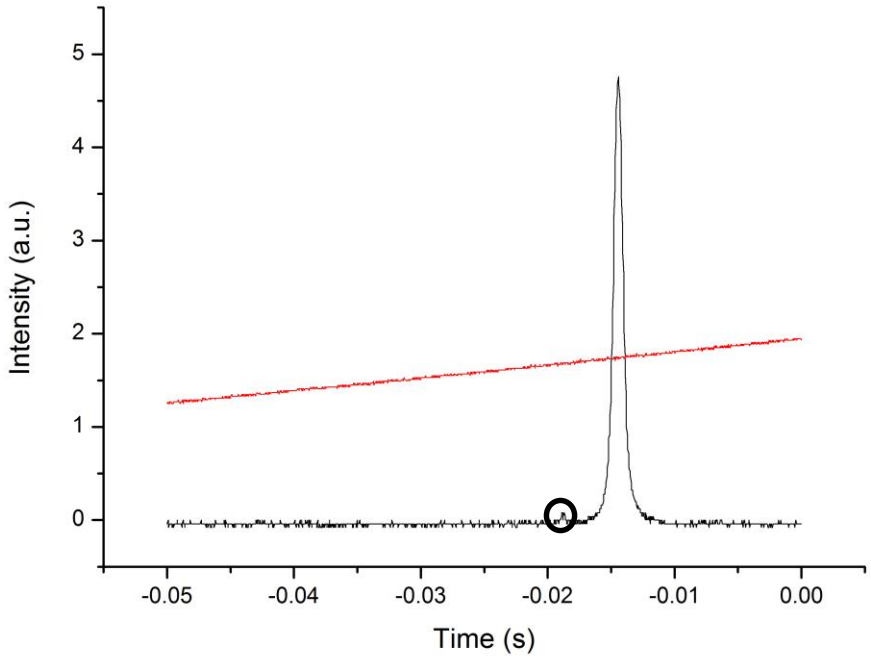

Figure 5.14 A zoomed in trace depicting a single peak from the above interferometer trace, with black and red traces again representing the interferometer signal and driving voltage applied to the piezo. The peak was found to have a linewidth of ~35 MHz, which is well within the phase matching bandwidth of all the crystals associated with this project. A small peak is also visible, encircled on the diagram, which indicates that there is still some parasitic lasing.

From the zoomed in trace from figure 5.14 the linewidth of the laser was found to be less than 67 MHz, which is the resolution limit of the instrument - this is well within the phase matching bandwidth of the OP-GaAs crystals associated with this project, which all have bandwidths on the order of ~3 cm^{-1}. The intracavity field was found to be 35 W under these conditions.

After characterising the SDL pump laser, we next modelled the threshold for the OP-GaAs crystals to assess the lasers suitability as a pump source for an ICOPO based on OP-GaAs. This is presented in the next section.

5.3 Threshold Modelling for New Crystals

Due to the destruction during polishing and recoating of sample 25B (see chapter 4 and Appendix A), three new OP-GaAs samples were delivered to us from BAE Systems, which had been AR coated at the pump wavelengths of the SDL and the consequent signal and idler wavelengths resulting from the phase matching of the crystals (Λ = 60.5 μm for all crystals). The new samples were labelled 25E, 60E1 and 60F1. Sample 25E was 26 mm long while samples 60E1 and 60F1 were 25.7 mm in length (for further details see appendix A).

For all of the modelling results presented a signal loss of 10 % is assumed to produce a conservative estimate. The pump wavelength was assumed to be 1971nm as this was the wavelength where optimal single mode performance was obtained from the SDL. With all of the crystals having a grating period of 60.5 μm, the signal and idler were assumed to be 2875 nm and 6275 nm from conservation of momentum. The temperature of the crystal, T, was assumed to be 22 degrees centigrade (room temperature).

Using the aforementioned parameters and assumptions, thresholds were modelled for crystals 60E1, 60F1 and 25E using equation 4.2 from the previous chapter. All mode radii within the cavity were confocal and thus were calculated according to equation 2.23. For quasi phase matched OP-GaAs crystals of length 25.30 mm (60E1 and 60F1) this leads to a threshold intracavity pump power of 28.9 W. For crystals of length 26 mm, the threshold intracavity pump power is

28.6 W. It should be noted that the primary pump power for the OPO pump laser has no bearing on these calculations.

With the pump laser (the host laser for the ICOPO) being capable of reaching up to 35 W of intracavity power with 10 % of the field being coupled out, the above estimates predict that it should be possible to bring all of these crystals to threshold within the SDL cavity. In the next section, the design of a suitable SDL based ICOPO cavity and its implementation shall be presented and discussed.

5.4 ICOPO Experimental Arrangement

Taking into consideration the characterisation performed earlier in this chapter the following cavity design shown in figure 5.15 was implemented. The SDL was once again pumped by a 980 nm diode, whose 105 μm core-diameter fibre coupled output was reimaged onto the GaSb SDL. An intracavity lens (ICL) of 75 mm, AR coated at 2 μm) was inserted into the cavity to produce a tight focus (144 μm) in the OP-GaAs crystal to improve the nonlinear conversion efficiency, while maintaining a suitably large confocal parameter to prevent clipping (66 mm, much longer than the crystal length). Only a single intracavity lens was used to reduce parasitic loss in the cavity. The pump arm of the cavity was terminated with a mirror (M1, ROC = 75 mm), which was both a high reflector for the pump and signal wavelengths. A birefringent filter was inserted into the cavity for longitudinal mode control of the pump laser. The signal cavity was formed by inserting a beamsplitter (BS) into the cavity which was anti-reflection coated for the pump on both sides while also being highly reflecting for the signal on one side. The signal arm was completed by a second high reflecting mirror for the pump and signal wavelengths with a radius of curvature of 75 mm to form a confocal cavity with mirror M1. A photograph of the cavity setup is shown in figure 5.16.

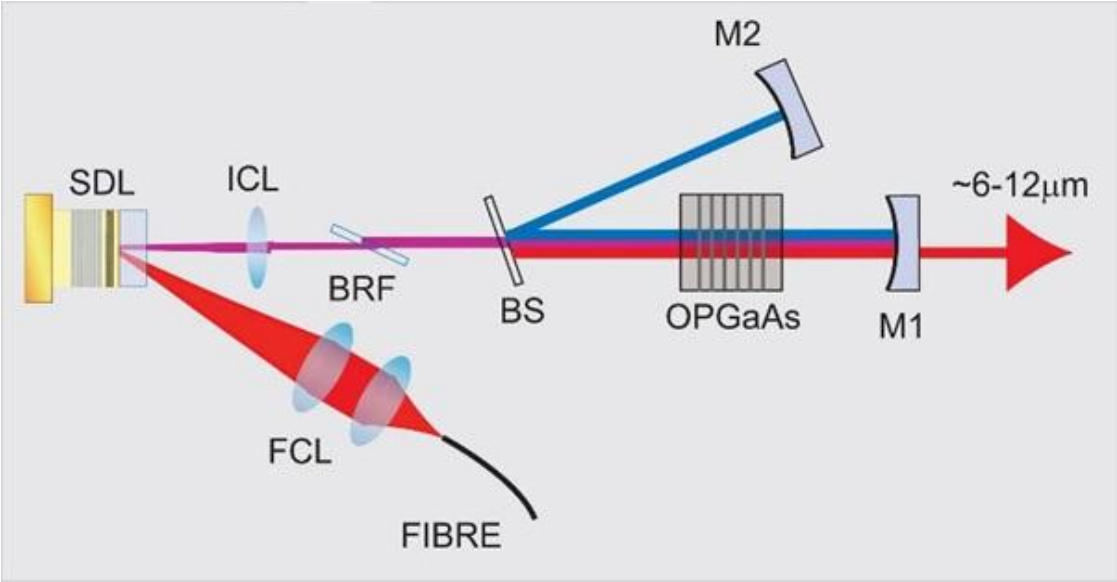

Figure 5.15. A diagram showing the setup designed to implement an SDL pumped ICOPO based on OP-GaAs. The laser is pumped by a 980 nm diode laser with a 105μm core-diameter fibre, whose tip is reimaged onto the SDL by a pair of lenses (FCL). An intracavity lens (ICL) with a focal length of 75 mm was inserted to produce a tight focus in the OP-GaAs to improve the nonlinear conversion efficiency. The pump cavity was terminated with a curved high reflecting mirror (M1) with a ROC of 75 mm. A birefringent filter (BRF) was inserted when longitudinal mode selection was required. The signal cavity was formed by the insertion of a beamsplitter (BS) and a second high reflector (M2) with a ROC of 75 mm.

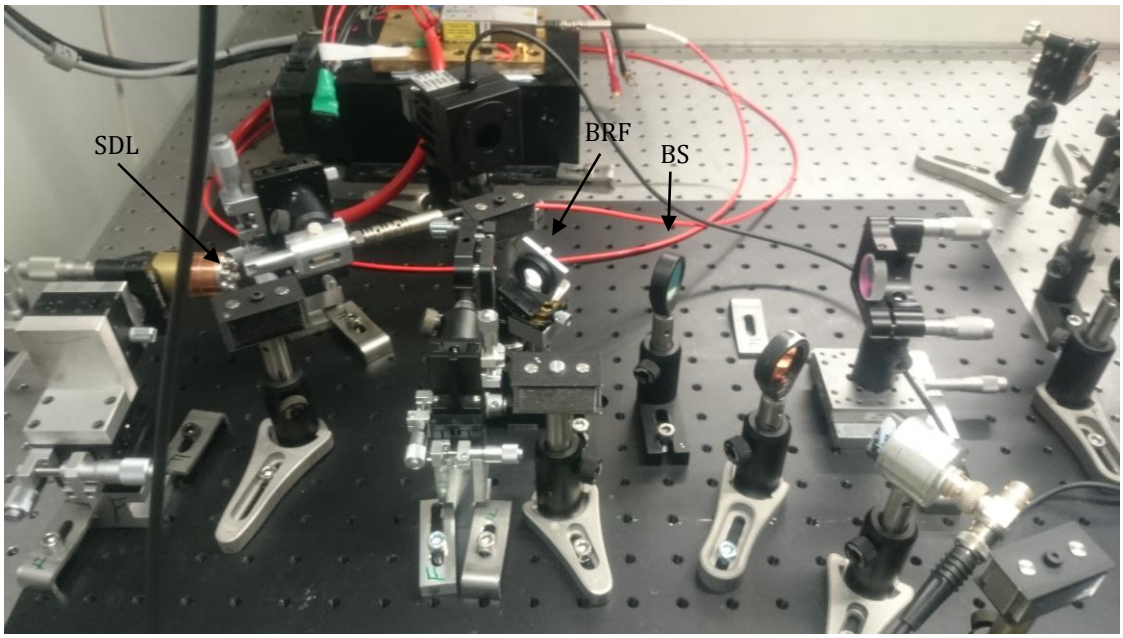

Figure 5.16 A photograph of the experimental setup. The SDL is housed in the brass water cooled mount on the far left, with the pump head for the diode laser being next to it. The intracavity lens and birefringent filter sit next each other in the cavity followed by the beamsplitter and the end mirror. The crystal and signal mirror are not shown in the above photograph.

A diagram of the separation between components and intracavity mode size is shown in figure 5.17.

The intracavity lens was placed 140 mm away from the SDL and the end mirror, ROC = 75 mm, was placed 356 mm away from the SDL. The centre of the nonlinear crystal was placed at the focus formed between the intracavity lens and the end mirror, which was situated 296 mm away from the SDL. The cavity mode radius at the pump spot was 136 μm and the mode waist was 144 μm in the OP-GaAs.

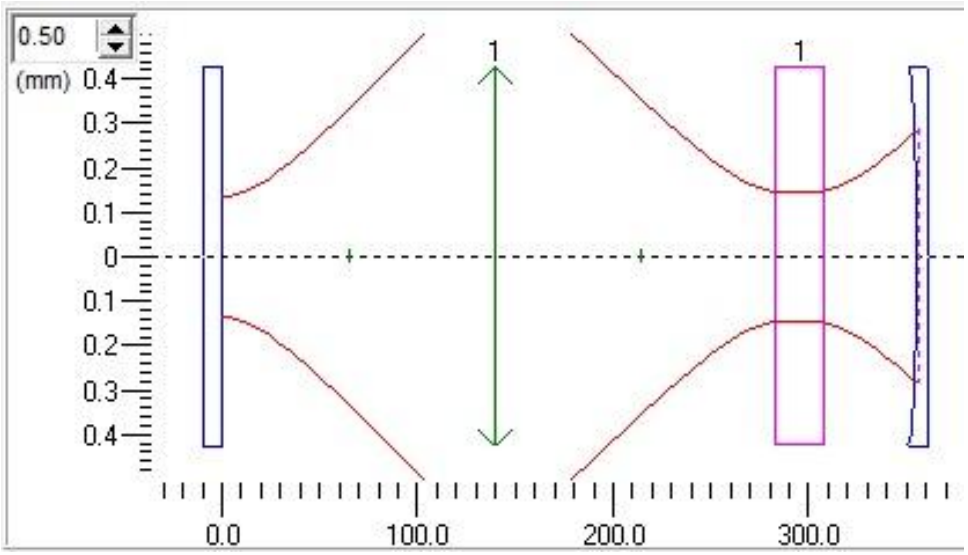

Figure 5.17 A schematic of the mode size and spacing throughout the SDL ICOPO cavity, generated through the Psst! program, which is distributed free through the university of St. Andrews website. The blue rectangle represents a plane mirror, the blue bowed rectangle a curved mirror, while the green double headed arrow represents a lens. The purple rectangle represents a block of nonlinear medium. All sizes are in mm.

The pump arm of the cavity was first constructed step by step, allowing for the intracavity field to be characterised as the device construction progressed. With the pump arm constructed, the maximum available intracavity field within the cavity before the OP-GaAs was inserted was 237 W. This result seemed promising for intracavity frequency conversion in the laser cavity. However, all attempts at achieving laser operation from the SDL with the OP-GaAs crystals in our possession in the cavity were unsuccessful. This leads to the conclusion that some particular property of the crystals in our possession was precluding laser operation of the pump laser by increasing the cavity loss beyond the limit of the gain of the GaSb SDL. In the next section, an investigation into the cause of the additional loss in the OP-GaAs crystals shall be presented. Properties such as

potential lensing effects, wedging between the faces of the crystals as well as scattering losses shall be quantified and discussed along with potential solutions to these problems.

5.5 Investigations into Crystal Properties

In the previous section, the construction of an SDL based ICOPO based on crystals 25E, 60E1 and 60F1 was attempted. However intracavity losses greater than the SDL could tolerate precluded laser, and therefore, OPO operation. In this section, potential sources of loss and barriers towards intracavity implementation of the crystal samples in our possession shall be investigated and reasons sought for their unacceptably high losses.

When specifying the coatings for an intracavity nonlinear crystal, priority is always given to minimising the losses of the signal band of the coating, as, along with the mode radius inside the crystal, this is the only parameter which affects the threshold of the OPO which is within the control of the experimentalist or device builder [1-4]. With the direct proportionality between the signal loss in the cavity and the threshold of the OPO, this is a rewarding path to follow. However, the loss within the cavity at the pump wavelength is also crucial to successfully realising an intracavity nonlinear frequency conversion device. If the gain of the medium used for the pump laser is not large enough to surmount the losses within the cavity, then the pump laser will never reach threshold [4, 5]. This renders any attempt to construct an intracavity OPO to be in vain. It is therefore crucial that the losses of the crystal in the ICOPO setup are as small as possible.

With the crystals in our possession being so lossy at the pump as to preclude operation of the laser, investigations where undertaken as to the source of the loss at the pump wavelength. With gallium arsenide being known to be transparent in the region of operation [6-10], it was assumed that the losses in the crystal were coming from elsewhere. There are many potential sources of losses in a nonlinear crystal. Significant sources of loss includes, but are not

limited to, absorption in the crystal, scattering from various sources, lensing due to bowing of the crystal faces, reflection from the coating due to not being 100 % AR and modification of the coating transmission by not passing through the face of the crystal at normal incidence due to wedging between the surfaces [2, 11-13].

The total transmission loss of the crystal was the investigated first, to see if this is what was precluding operation of the pump laser. To investigate the linear loss of the crystals, the SDL was pared back to the setup shown in figure 5.7, with a 1% output coupler being used to extract a suitable amount of field from the laser. A 150mm focal length lens was then placed a suitable distance after the SDL to produce a tightly focussed beam with a suitably large confocal parameter. The output power from the laser was then measured using a thermopile. The crystals were then placed in the beam path with the focus at the centre of the crystal and the maximum transmission through the crystals was then compared to output power from the laser to produce a single pass transmission loss measurement.

Crystal 25E was found to have a single pass transmission loss of 8.5 %, crystal 60E1 a single pass transmission loss of 8.7 % while crystal 60F1 had a single pass transmission loss of 7.4 %. This equates to round trip losses of 17 %, 17.4 % and 14.8 %. All of these losses would have precluded laser operation in the SDL cavity. The next practical step was to determine the sources of loss in the crystals, to see where improvements could be made in their processing which would lead to the production of a successful device. The first quantity to be measured was the reflectivity of the AR coatings, to see if they had been manufactured to specification.

To measure the reflectivity, a photometer was constructed as shown in figure 5.18.

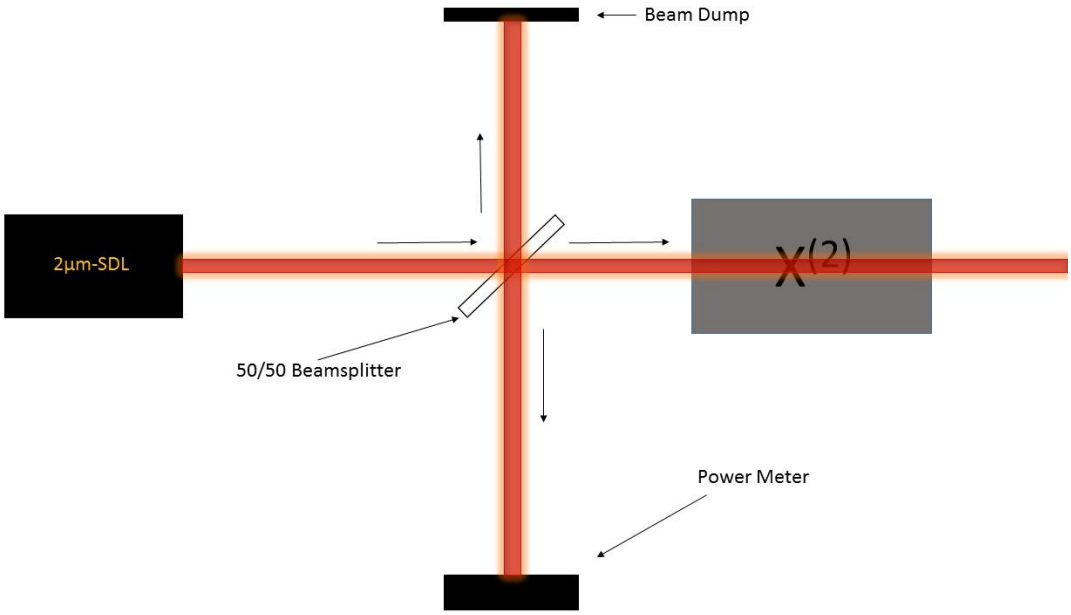

Figure 5.18 A schematic of the photometer used to measure the reflectivity of the coating on the OP-GaAs crystals. The SDL output was sent through a 50/50 beamsplitter with the reflection from the OP-GaAs picked off by the beamsplitter and 50 % of the reflected power being collected on the power meter.

The output from the 2 µm SDL was transmitted through a coated CaF_2 50/50 beamsplitter and the beam retroreflected from the coating on the OP-GaAs crystals. The beamsplitter then separated the reflection from the incident beam with the output being directed to a power meter to measure the back reflected power. The power transmitted through the beamsplitter and the power reflected back from a gold coated mirror (~100 % R) and off of the beamsplitter were measured to calibrate the beamsplitter's reflectivity. The reflectivity of the coatings from samples 25E, 60E1 and 60F1 was found to be 1.2 % ± 0.14 % at the OPO pump wavelength. A large aperture, AR-coated GaAs blank was used as a control piece to ensure that the results from the photometer were from a single facet of the OP-GaAs, which was the case, by comparing the percentage of light reflected against the percentage transmitted. A loss of 1.2 % per surface would equate to a 2.8 % loss on a single pass from the crystals which, while not as good as specified on the theoretical coating curves, does not account for the 7.4 % to 8.7 % single pass losses measured from the transmission measurements. This suggests that either absorption within the crystals or absorption at the surfaces due to defects from the polish are the cause of the high single pass loss within the

crystals and thus the SDL's failure to reach threshold. While the root cause of the SDL's inability to reach threshold has been established, academic rigour demands that the rest of the relevant laser engineering properties of the crystals are examined. The next property which was investigated was potential scattering losses within the crystals.

There are many potential sources of scattering losses within nonlinear crystals including, but not limited to, Rayleigh scattering, Brillouin scattering, scattering from defects in the crystal as well as surface scattering caused by a poor surface finish during polishing [11-13]. For those who wish to know more, the following texts provide an in depth discussion of scattering in its myriad forms [12, 13]. For our purposes, it is only required that we are aware that such things exist and must be taken into consideration as a finite source of intracavity loss.

An experiment was setup to attempt to quantify the scattering losses on a single pass from the crystal samples according to figure 5.19. A lens (f = 150 mm) was placed a suitable distance from the laser to produce a tightly focussed radius (~90 μm) with a suitably large confocal parameter (~26 mm, which is the length of the longest crystal) to prevent clipping of the beam while travelling through the crystal. An aperture was then placed in the beam path, far from the focus (500 mm), to clip out the outer diameter of the beam and the power transmitted was measured by the power meter. The crystals were then placed into the beam path at the focus and the transmitted power compared to the linear loss of the crystals to see if scattering losses could be detected. It should also be noted that, due to reduction in the divergence introduced by passing through such a long block of high refractive index ($n_{GaAs} \sim 3.4$ at 2 μm), one would expect to be able to squeeze more power through an aperture if there were no scattering losses at all.

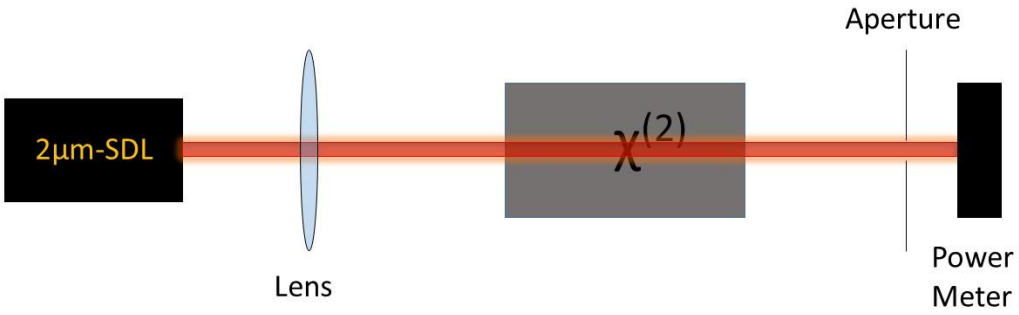

Figure 5.19 A schematic of the setup used to assess scattering losses from the OP-GaAs crystals. The output from the SDL was taken and focussed by a lens through an aperture on to a power meter, and the difference between the measured power, and the power measured when the crystal was placed in the way was used to give an indication as to whether light was being scattered significantly by the crystal or not.

Crystals 60E1 and 60F1, when placed in the setup, were able to force more power through the aperture than when there was no crystal in the beam path, suggesting that the scattering losses in these crystals were not large enough to be worthy of consideration. However, when crystal 25E was placed in the beam, a reduction in power of 13 % ± 2 % was detected on the power meter, which when compared to the transmission loss of 8.5 %, suggests that scattering losses within this sample were considerable.

From the above experiment one can see that, for crystal 25E, the additional scattering losses would have raised the threshold of the pump laser even further, making the picture for constructing an SDL ICOPO from that crystal even bleaker. Crystals 60E1 and F1 showed satisfactorily low levels of scattering loss, suggesting that scattering from these crystals did not influence the pump laser threshold.

The next property which was investigated was if there was any wedging between the crystal surfaces from the polishing process. To investigate this, the following experiment was setup. A He-Ne laser was setup on the table and the beam from

the He-Ne was retroreflected from the face of one of the crystals. The crystals were mounted in a fully gimballed mount, allowing for on-axis rotation of the crystal, as shown in figure 5.20. The crystal was rotated 180 degrees and the new position of the reflected He-Ne was noted and trigonometry was used to identify the angle of the wedge between the faces, if any was present.

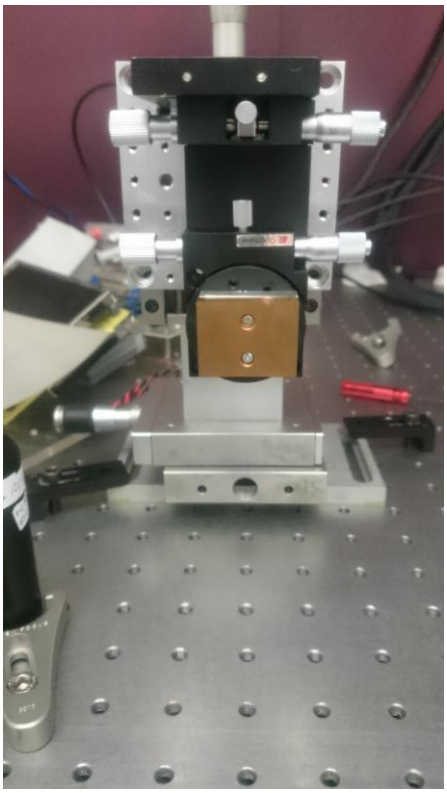

Figure 5.20 A photograph of the mount used for holding the OP-GaAs crystals. The mount has 3 linear degrees of freedom and 2 degrees of rotational freedom.

First crystal 25E was investigated. A wedge of ~ 0.4 degrees was found between the 2 short edges of the crystal face, while any wedging between the long edges of the crystal faces was found to be negligible. Crystal 60E1 was found to have a wedge of ~1 degree between the two long edges of the crystal face and no discernible wedging between the short edges of the crystal face. Lastly, crystal 60F1 was examined and a wedge of ~1.3 degrees was found between the short edges of the crystal face while no discernible wedging was detected between the long edges of the crystal face.

Finally, the surfaces of the crystal were examined to see if there was any bowing present, which would have led to lensing of the beam as it passed through the

crystal. To investigate this, a Twyman-Green interferometer, a well-established tool for investigating the quality of optical components [14, 15], was setup as shown in figure 5.21.

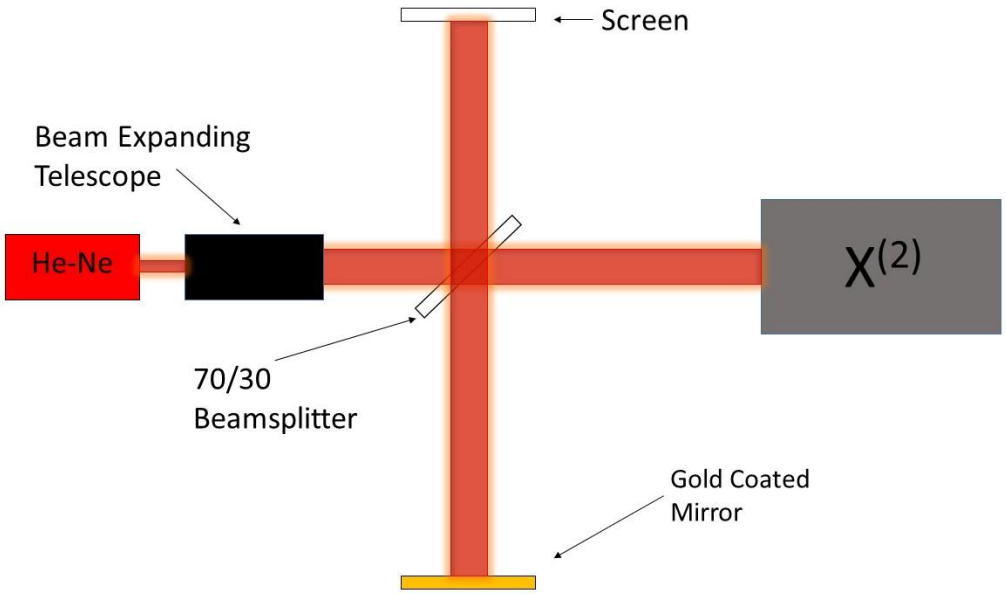

Figure 5.21 A schematic of the Twyman-Green interferometer which was set up to examine the surfaces of the OP-GaAs crystals. A He-Ne laser was taken and its output expanded to produce an approximately plane wavefront. This output was then split with a beamsplitter and sent along two different paths, before being recombined with the output being made visible on a screen.

A He-Ne laser was used due to the high reflectivity of the coatings on the crystals in the visible and the long coherence length of the emitted radiation due to their typically narrow linewidths. The two arms of the interferometer were roughly balanced at a distance of 135 mm from the beamsplitter, which was far shorter than the coherence length of the He-Ne (~300 mm), ensuring that high contrast interference patterns would be observed [14]. As the beams were both plane, parallel on-axis, wavesources, interference would present itself as bright and dark images on the screen, as opposed to fringes which would result from off-axis beams. This suggests that distortion of the plane wavefronts in anyway should result in the emergence of interference fringes. A beam expanding telescope was placed into the setup after the He-Ne to generate plane waves. The screen was mounted on a slowly rotating motor to eliminate speckle in the interferograms.

The three crystals were placed into the setup and the interferograms recorded are shown in figures 5.22, 5.23 and 5.24.

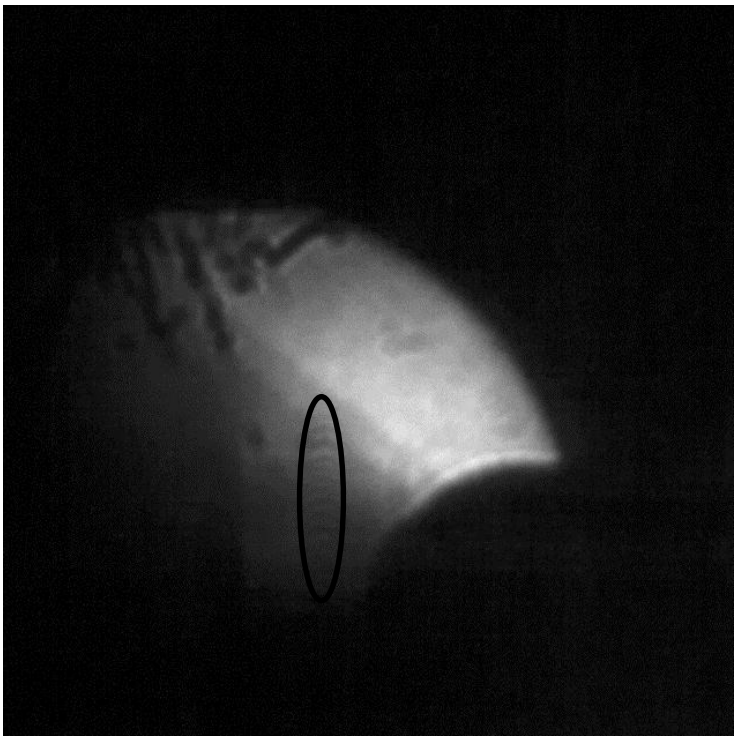

Figure 5.22 An Interferogram of the surface of crystal 25E. Interference fringes from the crystal can be observed in the area encircled by the black ring.

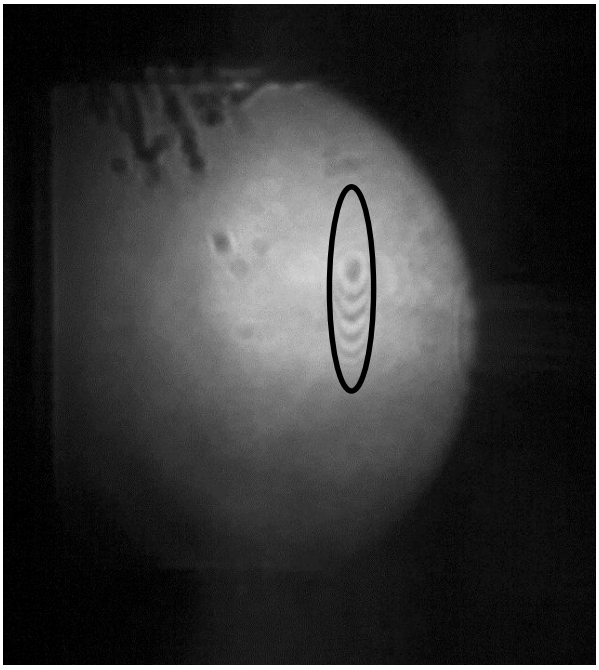

Figure 5.23 An Interferogram of the surface of crystal 60E. Similar fringes to those observed in the previous figure can also been seen in the area highlighted by the black ring.

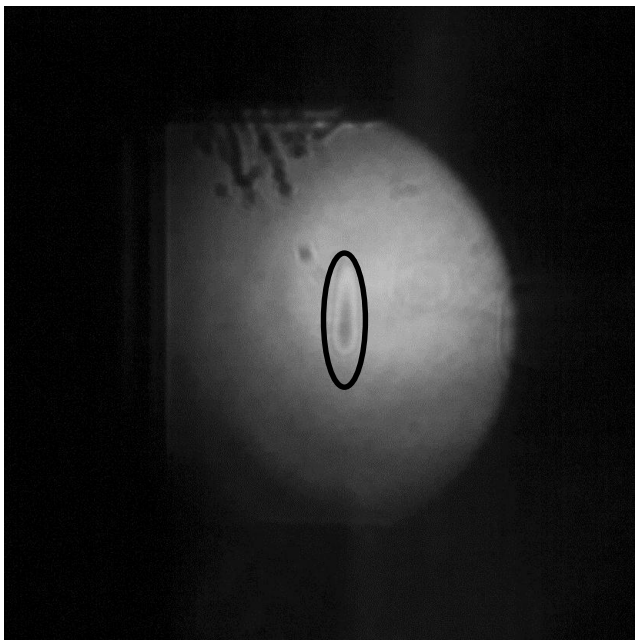

Figure 5.24 An Interferogram of the surface of crystal 60F. Again, an interference pattern can be observed within the region highlighted by the black ring, suggesting distortion of the wavefront by some means.

From the interferograms taken of the three crystals it is clear to see that the wavefronts being reflected from the crystal surfaces are being distorted in some way. However, it was not clear to see from the interferogram if this was being caused by the geometry of the faces of the crystal or if the beam was being diffracted from the mouth of the crystal mount. A set of analogous control experiments were setup to identify the cause of the wavefront distortions indicated by the interferograms in the above figures.

First an artificial slit of the same dimensions as the mouth of the crystal mount was constructed by laminating sheets of paper together to identify what the interference pattern generated by diffraction from a rectangular slit would look like. The slit was attached to the front of a gold mirror and the interferogram generated is shown in figure 5.25. The interferogram appears to be very similar to the interferograms shown in figures 5.22, 5.23 and 5.24, which suggests that diffraction from the input slit to the crystal mount is contributing to the distortion of the wavefront from those setups.

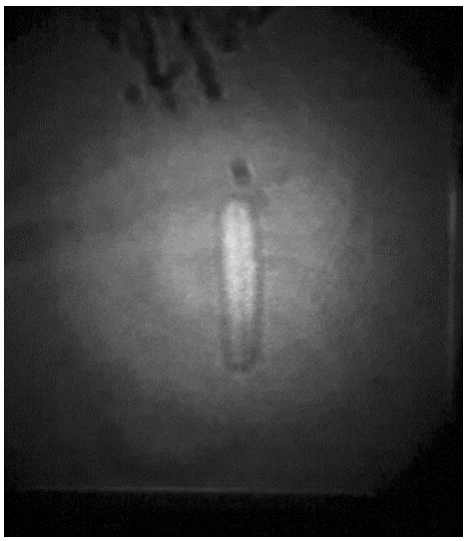

Figure 5.25 The interferogram generated by the wavefront reflected through a narrow aperture, such as a slit. There is no obvious interference fringes to be seen due to the lack of considerable distortion in the wavefront.

A lens with a large radius of curvature (200 mm focal length) was then examined in the interferometer, with the resulting interferogram shown in figure 5.26.

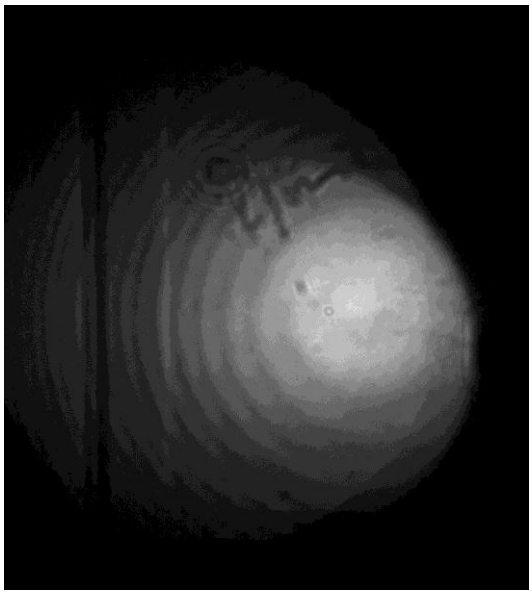

Figure 5.26 The interferogram generated by the surface of a lens. The ring shaped fringes generated are a clear indication of a plane wave interfering with a curved wavefront, such as that reflected by the curved surface of a lens.

It can be seen from figure 5.26 that the interference pattern produced by interfering a plane wave and a curved wavefront is different from that shown in the figures of the crystals, suggesting that there may have been no curvature of the wavefronts due to reflections from the crystals. To be sure that there was no

curvature at all, the artificial slit was placed on the front of the lens to see what effect diffraction through a slit would have after being reflected from a curved wavefront, the resulting interferogram is shown in figure 5.27.

Figure 5.27 The interferogram generated from the surface of a lens with a slit aperture placed over the top. The clear bulls-eye like structure seen in the centre of the slit aperture like interferogram is reminiscent of a scaled down analogue of the interference pattern generated directly from the curved surface of a lens.

The interferogram in figure 5.27 is similar to the interferogram in figure 5.26, which shows that the bowing of the wavefront due to the curvature of the lens dominates over the effect of diffraction from the slit. From this it can be concluded that there was no discernible bowing of the surfaces of the crystals generated during the polishing process, and thus lensing from the crystals would not have occurred.

To summarise the evaluation of the optical properties of the crystals 25E, 60E1 and 60F1, all three crystals exhibited high single pass transmissions losses, which would have precluded operation of the SDL. The reflectivity of the coatings applied to the crystals was 1.2 %, which indicates that linear loss, either from absorption in the crystals or from surface defects, is the reason for this. Crystal 25E also showed significant levels of scattering. All of the crystals were found to have been polished with a wedge between the two faces, which would have complicated the implementation of the crystals internal to the SDL cavity, but

would not have prevented laser operation in the device. Finally the flatness of the crystal surfaces was assessed and they were found to show no significant camber which could be detected.

5.6 Conclusions

With the destruction of both the SDL sample and the fragmenting of the previous OP-GaAs sample a new SDL sample was cleaved from the same wafer as the original and characterised. The SDL optimally output coupled at 6 % loss and was capable of reaching intracavity powers of 25 W within a linewidth of 35 MHz at 1971 nm and could be tuned from 1955 nm to 2010 nm with a loss of 10 % from the cavity. At lower cavity losses (~1 %) over 200 W of intracavity power could be obtained. This boded well for the potential of constructing an ICOPO from this laser system.

The crystal used in the previous chapter (25B) was broken during polishing when it had been sent to be recoated. Three new crystal samples were received from BAE systems to replace it – samples 25E, 60E1 and 60F1. The three crystals were tried within the SDL cavity which had been constructed, but the laser could not be brought to threshold with any of the crystals internal to the laser cavity. The three crystals were found to have high single pass losses (8.5 %, 8.7 % and 7.4 %), which equated to round trip losses of 17 %, 17.4 % and 14.8 % which would have precluded laser operation of the SDL had they been inserted into the cavity. The reflectivity of the coatings on the crystal was found to be ~1.2 % at the operating wavelength of the SDL, which would have only accounted for 2.4 % of the single pass loss, suggesting that parasitic absorption was the source. It is suspected that, based on the coating company's inexperience with polishing the material, surface defects produced by the polishing process may be to blame, although the ultimate source of the losses are unknown. Crystal 25E was also found to scatter light significantly as well, which would have placed laser operation further out of reach if it was placed internal to the cavity. The surfaces

of the crystals were also found to be wedged after polishing, which would have rendered their alignment within a laser cavity a nontrivial matter, but no curvature could be detected from them.

In the next chapter the work within this thesis shall be concluded and a discussion of future work which would lead to improvements or the realisation of the research contained herein, as well as possible new research directions, will be presented.

5.7 References

1. Ebrahimzadeh, M. and M.H. Dunn, *Optical Parametric Oscillators*, in *Handbook of Optics*. 2004, McGraw-Hill.
2. Stothard, D.J.M., *Practical Continuous Wave Optical Parametric Oscillators*, in *Advances in Optical and Photonic Devices*, K.Y. Kim, Editor. 2010, InTech.
3. Sutherland, R.L., *Handbook of Nonlinear Optics*. Second Edition ed. 2003: Marcel Dekker.
4. Hooker, S. and C. Webb, *Laser Physics*. Oxford Master Series in Atomic, Optical and Laser Physics. 2010, U.K.: Oxford University Press.
5. Svelto, O., *Principles of Lasers*. 2010: Springer.
6. Schunemann, P.G., et al. *Recent Advances in All-epitaxial Growth and Properties of Orientation-patterned Gallium Arsenide (OP-GaAs)*. in *Lasers and Electro-Optics, 2009 and 2009 Conference on Quantum electronics and Laser Science Conference. CLEO/QELS 2009. Conference on*. 2009.
7. Schunemann, P.G., et al. *2.05-μm-Laser-Pumped Orientation-Patterned Gallium Arsenide (OPGaAs) OPO*. in *Conference on Lasers and Electro-Optics/Quantum Electronics and Laser Science and Photonic Applications Systems Technologies*. 2005. Baltimore, Maryland: Optical Society of America.
8. Skauli, T., et al., *Improved Dispersion Relations for GaAs and Applications to Nonlinear Optics.* Journal of Applied Physics, 2003. **94**(10): p. 6447-6455.
9. Vodopyanov, K.L., et al., *Optical Parametric Oscillation in Quasi-phase-matched GaAs.* Optics Letters, 2004. **29**(16): p. 1912-1914.
10. Yu, X., et al., *Growth of GaAs with Orientation-patterned Structures for Nonlinear Optics.* Journal of Crystal Growth, 2007. **301–302**(0): p. 163-167.
11. Dmitriev, V.G., G.G. Gurzadyan, and D.N. Nikogosyan, *Handbook of Nonlinear Optical Crystals, Second, Revised and Updated Edition*. 1997: Springer.
12. Fox, M., *Optical Properties of Solids*. 2010: Oxford University Press.
13. Hayes, W. and R. Loudon, *Scattering of Light by Crystals*. 1978: John Wiley and Sons.
14. Malacara, D., *Twyman–Green Interferometer*, in *Optical Shop Testing*. 2006, John Wiley & Sons, Inc. p. 46-96.

15. Michelson, A.A., *On the Correction of Optical Surfaces.* Proceedings of the National Academy of Sciences of the United States of America, 1918. **4**(7): p. 210-212.

Chapter 6
Conclusions and Future Work

6.1 Introduction

In the previous chapters, the developmental prospects were explored and attempts to realise them were made for two different types of OPO system based on OP-GaAs - pulsed ICOPOs based on Tm^{3+}:YAP as well as cw-ICOPO devices based on GaSb SDLs. In the following chapter, the key points from these experiments will be summarised as well as potential improvements which could be made to the experimental arrangements and the associated devices. Finally, potential future work which could be readily derived from the contents of this thesis will be discussed and presented to the reader alongside the current state of the art in the field.

6.2 Tm^{3+}:YAP Pumped, Pulsed OPO Based on OP-GaAs

The operation of a Tm^{3+}:YAP pumped pulsed OPO based on orientation patterned gallium arsenide was demonstrated. For 15 W of incident diode pump power (10.5 W absorbed) up to 120 mW of useful idler (650 mW of total downconverted power) could be extracted from the device at a repetition rate of 200 kHz. Based on output coupling 1.08 W at 7 % (optimal) output coupling, this gives us a downconversion efficiency of 60 %. The OPO could be tuned over the range 2.9 μm to 3.5 μm (0.6 μm) in the signal and 4.6 μm to 5.8 μm (1.2 μm) in the idler for 54 nm of tuning in the pump for a 56 μm period crystal. For a crystal of QPM grating period of 60.5 μm the OPO could be tuned over the range 5.9 μm to 6.8 μm (0.9 μm) in idler & 2.7 μm to 3 μm (0.3 μm) in signal for 50 nm of tuning in the pump. While the device as a whole is inefficient in terms of diode pump to extracted idler optical to optical efficiency, the efficiency of the OPO is good. The Tm^{3+}:YAP pump laser was later shown to be inefficient, which shows good promise for the ICOPO itself. It must again be stated that this is, to the best of the

author's knowledge, the only cw-ICOPO based on OP-GaAs developed in the world.

The performance of the device which was constructed could be improved in a number of ways. The most significant, and also the easiest to ameliorate, are the factors related to the high threshold pump power of the Tm^{3+}:YAP laser. As the OPO itself was efficient, improvements here would produce the largest effect on the efficiency of the device. Replacing the relatively long (5 mm) crystal used in these investigations with a shorter crystal, such as a 2.5 mm long crystal (commercially available from Scientific Materials corporation) would lead to significantly reduced pump thresholds with regards to absorbed pump power. By replacing the coatings on one face of the crystal with one which is AR at the emission wavelength, but HR at the pump, the transmitted pump can be recycled. This would increase the amount of pump power absorbed from the diode laser for a given amount of electrical power. The fibre coupled diode laser which was used to pump the thulium laser also offers an easy path towards device optimisation. With a fibre core diameter of 600 μm, which was the state of the art when procured, this led to the requirement of a relatively large cavity mode diameter within the crystal. By switching to a brighter pump diode (200 μm fibre diode pump lasers are now commercially available), the threshold pump power of the laser could be reduced even further, increasing wall plug efficiency of the device. However, in this regime, care must be taken to control the thermal lensing within the crystal by using an approach such as more aggressive cooling or using top hat profile pump beams.

The downconversion efficiency within the OPO would be another area where improvements could be made. The signal coatings for the OP-GaAs crystals which were in our possession at this stage in the project (samples 25B and 26K) were non-optimal for the range of pump wavelengths available from the Tm^{3+}:YAP laser. It was later discovered that they were supplied coated for Ho:YAG wavelengths (~2.1 μm). However, due to the scarcity of high quality OP-GaAs material, the crystals had to be accepted with the coatings with which they were supplied by BAE systems and as such we had no control over the supplied

coatings. The OP-GaAs crystals both phase matched for the pump wavelength in areas of moderate to serious loss at the signal wavelength from the coatings on their end facets. The overlap between all of the signal coatings for sample 26K are shown in figure 6.1. The mirror and beamsplitter coatings, however, aligned reasonably well with Tm^{3+}:YAP's gain bandwidth.

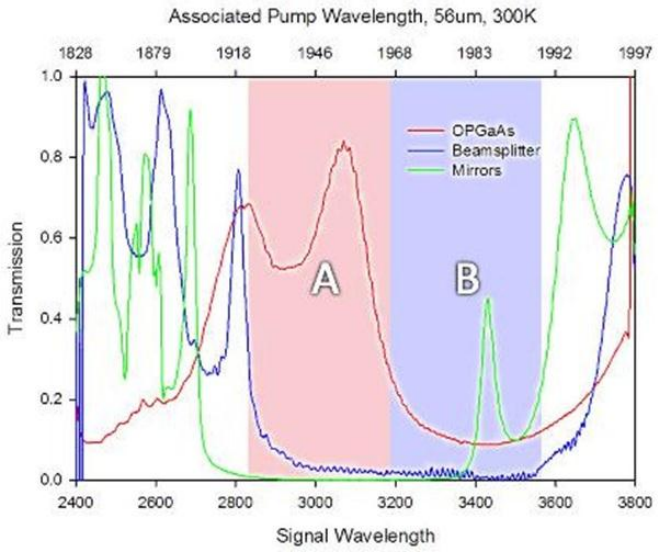

Figure 6.1 A diagram showing the overlap between the signal coatings on the mirror, beamsplitter and crystal for sample 26K. While section A offers up to ~85% transmission in the OP-GaAs crystal, in section B the coating actually offers up to 90% reflectivity, which inhibits operation in this range.

For sample 25B the signal coatings of the crystal not well matched to the signal generated due to phase-matching by the pump, to also further constrain things, the signal wavelengths generated by sample 25B were not well matched to the beamsplitter and mirror coatings either. The overlap between the various coatings are shown in figure 6.2

From figure 6.2 it is possible to see that the smallest round trip loss introduced by the signal coatings is at a point between 3200 nm and 3400 nm – which requires a pump wavelength of 2020-2030 nm. This lies outwith the gain bandwidth of a Tm^{3+}:YAP laser, making optimum operating parameters unreachable. Ultimately, the efficiency of the OPO section of this device was hamstrung by the unavailability of optimal coatings. However, the ability of

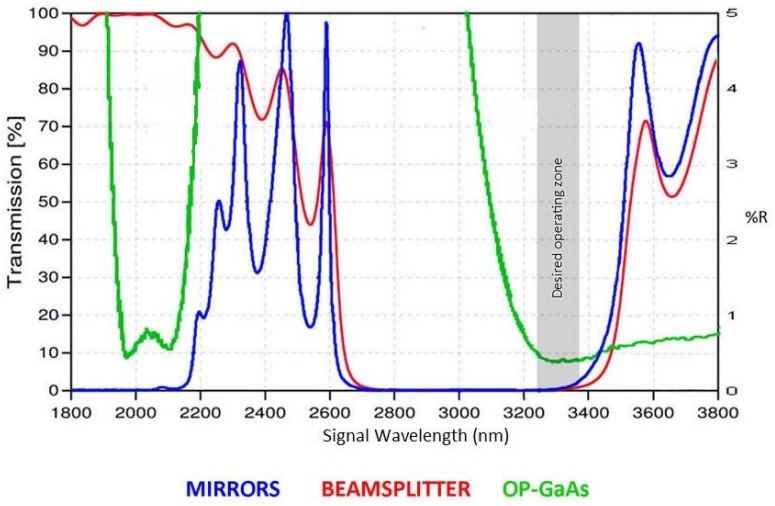

Figure 6.2 A plot displaying the overlap between the mirror, beamsplitter and OP-GaAs. The area highlighted in grey shows the region where the losses at the signal wavelength are minimized, unfortunately this required a pump wavelength of 2020-2030nm which is outwith the gain bandwidth of Thulium.

pulsed optical parametric oscillators to overcome high round trip losses at the signal wavelength to reach operating threshold (indeed the threshold of such devices are fairly insensitive to signal losses [1, 2], see equation 2.27 from chapter 2.) meant that while the conditions for operating this device were far from ideal, it was still possible to construct a device which functioned admirably and at output powers great enough to be used in practical applications.

For the further improvement of this device as it stands for commercialisation, along with the suggestions outlined above, the device footprint could be reduced by the implementation of custom optomechanical mounting components allowing for miniaturisation of the device, as the large scale of the cavity implemented (see figures 3.3 and 3.4 from chapter 3) was to accommodate the bulky optomechanical components used in the development process – these would no longer be necessary for a cavity based on the results derived from this research. A dramatic increase in electrical power efficiency could also be found by the use of more modern, efficient diodes as the diode used in the research in this thesis was not efficient by the standards of modern 795 nm diode bars – for ~90 W of electrical power only 15 W of laser power was emitted. Using more efficient diodes not only improves "wall-plug" efficiency by reducing the

electrical power required to achieve a certain laser power but also by reducing the amount of waste heat produced, and thus reducing the amount of power which must be expended on cooling.

6.3 GaSb Semiconductor Disk Laser Pumped CW-ICOPO Based on OP-GaAs

Two SDL chips were bonded to a 250 μm diamond heatspreader and their suitability as pump lasers for an OP-GaAs based cw-ICOPO were assessed. As a direct bandgap semiconductor, the GaSb quantum wells in the samples had upper state lifetimes on the order of nanoseconds, which eliminates the most prominent deficiency of cw-ICOPOs – the prolonged relaxation oscillations associated with introducing the OPO into the cavity. With intracavity fields of 58.2 W and 40 W being achieved using a 10 % output coupler with each sample, as well as over 200 W at high finesse, this demonstrated that both of the samples were capable of bringing an ICOPO cavity to threshold had the pump and signal round trip loss been small (with thresholds for very low loss systems being as little as ~10 W of intracavity field). However, it was not possible to bring either sample to threshold, due to elevated losses in either the pump or signal.

In the case of the first sample which was investigated in chapter 4, the act of bringing the ICOPO to threshold was ultimately precluded by the mismatch of the signal coating on the OP-GaAs crystal to the signal wavelengths generated by phase-matching within the gain bandwidth of the SDL material. A replacement coating was sought from the same company who had produced the coating on the crystal (Twinstar inc.), but this was not to be the solution of the problem. The crystal sample was snapped by the coating company during the polishing process to remove the coating. Three replacement crystals were acquired from BAE, and after some discussion between themselves and Twinstar about how to polish the crystals without damaging them, the crystals were then polished successfully, without damage occurring, and recoated by Twinstar. However, it was then found that these crystals had high linear losses at the pump wavelength - in the region of about 7.5 % to 8 % on a single pass. This was a higher loss than the SDL samples

could tolerate due to the low gain associated with semiconductor disk lasers. The coatings themselves were found to have reasonably low single pass losses, in the region of around 1.5 %, which suggests that surface defects due to the immature polishing process used by Twinstar may have been the cause of the high linear loss in the 2 μm region – the original crystal had been polished by BAE and was of excellently low loss and high quality. While ICOPOs based on SDL devices have been demonstrated (see [3]) these were based on mature technologies in the 1 μm region of the spectrum using well established OPO materials such as PPLN. It seems that, with the lack of maturity in tri-band coating technology with materials used at 2 μm as well as in commercial crystal processing techniques for OP-GaAs, there are still significant engineering challenges to be overcome in these fields before cw-ICOPO devices based on OP-GaAs can be developed and commercially exploited. It is with this in mind, that I would recommend suspending work on the cw-ICOPO based on an SDL until the aforementioned technologies mature to the point where such a device can be constructed, and would recommend concentrating on the pulsed ICOPO system.

6.4 Further Work

While the cw-ICOPO system shows promise, and the modelling suggests that it is feasable, several challenges must be overcome before it is ready to be fully developed and exploited – in this work it has been found that simply replicating the methods and successes of the 1 μm PPLN systems is not so simple due to both the crystal and coating technologies not being so well developed yet. Due to its insensitivity and tolerance of parasitic loss at both the signal and pump wavelengths, the pulsed ICOPO is in a strong position for further exploitation and development. It is here that I would focus ongoing efforts.

The basic device could be improved by improving its efficiency and miniaturising its footprint for commercial exploitation as a tunable, mid-IR laser system as explained earlier in this section, as well as in the conclusions section of chapter 3. However, there are other improvements to be made, which would open up a wider range of commercial and scientific applications for the device.

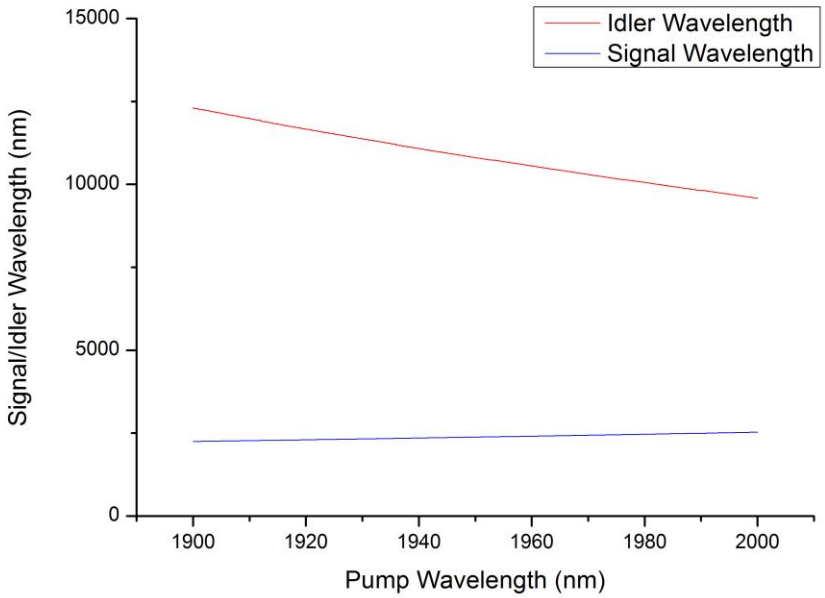

Figure 6.3 A phase matching diagram for OP-GaAs with a grating period of 75µm for a wavelength range covering the tuning range of the TmYAP crystal used in this work (1.9µm to 2.0µm).

One of the limitations for the current device which was built in the lab is that, compared to the mid-IR tuning range outlined in the introductory chapter, it does not cover the full range which was originally aimed for – the device only tunes to ~7 µm compared to the full 12 µm which OP-GaAs is theoretically capable of tuning to (having a transmission from 2 µm to 12 µm [4-7]). By implementing OP-GaAs crystals which can phase match with an ~2 µm pump while producing an idler wavelength in the 12 µm region (a grating period of 75 µm covers the full 10 µm to 12 µm region for the tuning range of TM^{3+}:YAP– see figure 6.3), or indeed a fanned grating design where part of the grating covers this region [8], the full range of molecular transitions shown in chapter 1 could be accessed by the OPO for spectroscopy applications. Attaching such a device to an imaging system (such as the galvanometric imaging system found in commercial lasers like M Squared Lasers Ltd firefly systems – see http://www.m2lasers.com for further details) the device could then be used to scan for gaseous substances in the field.

Molecules with transitions in the mid-IR region tend to be large, low resonant frequency compounds with relatively large absorption linewidths [9] and as such there is no immediate requirement to narrow the linewidth of the pulses output

from the pulsed ICOPO device. However, as the linewidth of the output pulses is currently undetermined due to the lack of suitable diagnostics available in the laboratory, methods by which this can be achieved should also be considered in case such things are later found to be necessary. The idler output from the OPO system could be narrowed in several ways – first an etalon can be inserted into the signal cavity to narrow the signal spectrum. As the linewidth of the idler output is determined by the signal and pump linewidths (see equation 2.16 from chapter 2), narrowing the signal linewidth, alongside the already narrow pump linewidth, should narrow the resultant idler spectrum. A second way by which this can be achieved is by lengthening the nonlinear crystal in the OPO, as this narrows the phase matching bandwidth for the idler and thus also narrows the idler linewidth. This method also has the added benefit of increasing the available parametric gain.

Another potential path for cw-ICOPO development would be to use Tm^{3+}:YAP as the host laser system for the ICOPO. While the high upper state lifetime does not make it as ideal a candidate as an SDL to host an ICOPO, due to the erratic and prolonged effects that this would have on the relaxation oscillations (see chapter 2), the larger available gain in Tm^{3+}:YAP would loosen the requirements on the performance of the tri-band coatings on the OP-GaAs as higher losses at the pump could be more readily overcome. There are also ways in which the relaxation oscillations of the pump within the cavity could be further damped, which would ameliorate the effect which these would then have on the signal, and consequently, the idler fields. By inserting an additional, non-linear loss into the pump laser cavity such as a second harmonic generation crystal, like in the previous work of Stothard and Dunn with neodymium [10], large spikes in the circulating field can be damped. This process works by converting them into non-oscillating radiation in the cavity, in a process is which is proportional to the amplitude of the oscillations, which has no further influence upon any of the fields in the cavity or the upper state population. This could provide a promising avenue of development for an OP-GaAs based cw-ICOPO platform based on established research.

Overall, it has been shown that the pulsed ICOPO has proven itself ready for full exploitative development as a tunable mid-IR laser system. It has also been shown that GaSb SDL devices would make a suitable host laser system for an OP-GaAs based ICOPO, but that the coating and crystal manufacturing technology is not yet mature enough for device demonstration and development.

6.5 The Current State of the Art

Thus far in this thesis, only the results pertaining to the author's work in the field of OP-GaAs OPO's have been presented along with a brief introduction to other, competing technologies. To fully elucidate the reader on the current state of the art with OP-GaAs OPOs, a brief summary of the research being undertaken and some noteworthy results from other research groups shall be presented here.

At BAE systems in Nashua in the United States of America, Pete Schunemann's group have been growing and implementing OP-GaAs crystals in a variety of ways and systems. One particularly noteworthy result in the field of OPO development has been the development of a high power OPO system producing 4 W of idler radiation at 4.7 μm from 25 W of pump from a Ho:YAG laser [11]. This group has also recently grown fanned grating period crystals which could have very good implications for producing highly tunable OPO devices as mentioned earlier in this chapter [12].

Collaborations between Pete Schunemann's group and Konstatin Vodopyanov (formerly of Stanford, but now at Creole university) have also produced some important results in this field. They have published data on the most broadly tunable OP-GaAs OPO which has yet been demonstrated, This OPO system was pumped by the output of a PPLN OPO and tuning was achieved by means of adjusting both the PPLN OPO output wavelength as well as adjusting a diffraction grating placed in the signal cavity of the OP-GaAs OPO in the system. This OPO could be tuned in the range of 4 μm to 14 μm. Further details can be found on this work here [13]. This collaboration has also brought about the realisation of the world's first fs-OPO based on OP-GaAs [14]. This would expand the temporal

range of the OP-GaAs OPO further as well as enable to creation of mid-IR frequency combs [15].

Another promising area of theoretical research is being undertaken in Ankara at the tübitak bilgem iltaren by Fiken et al looking at using aperiodic gratings to improve the efficiency of longer wavelength OPO's based on OP-GaAs. By using an aperiodic grating, it is possible to generate both the idler which one wishes from one's pump wavelength, but also to then recycle the signal wavelength and produce further idler as well as the difference frequency between the signal and the idler. This method shows promise for enhancing the efficiency of such long-wavelength OPO devices but has yet to be practically pursued [16, 17].

The most similar analogues the technology which was investigated in this thesis are the NESCOPO (nested cavity OPO) devices produced by a collaboration between ONERA and Thales in France by Godard et al [18]. These devices, which are pumped by a Tm^{3+}YAP microlaser, consist of an OP-GaAs crystal which is placed in two nested cavities. One cavity is resonant for the signal wavelength, while the other is resonant for the idler wavelength. Such a doubly resonant OPO device has the advantage of having both a narrower linewidth and much lower threshold (6-10 μJ [18, 19]) than singly resonant devices. However, with the resonance conditions of two cavities having to be satisfied, this makes smooth, mode-hop free running much more difficult to implement. By temperature tuning this device, emission between 10.3 μm and 10.9 μm has been demonstrated, as well as stand-off detection of ammonia vapour [18].

6.6 References

1. Brosnan, S. and R.L. Byer, *Optical Parametric Oscillator Threshold and Linewidth Studies.* IEEE Journal of Quantum Electronics, 1979. **15**(6): p. 415-431.
2. Ebrahimzadeh, M. and M.H. Dunn, *Optical Parametric Oscillators*, in *Handbook of Optics*. 2004, McGraw-Hill.
3. Stothard, D.J.M., et al., *Stable, Continuous-wave, Intracavity, Optical Parametric Oscillator Pumped by a Semiconductor Disk Laser (VECSEL).* Optics Express, 2009. **17**(13): p. 10648-10658.

4. Kieleck, C., et al., *High-efficiency 20–50 kHz Mid-infrared Orientation-patterned GaAs Optical Parametric Oscillator Pumped by a 2 μm Holmium Laser.* Optics Letters, 2009. **34**(3): p. 262-264.
5. Schunemann, P.G., et al. *2.05-μm-Laser-Pumped Orientation-Patterned Gallium Arsenide (OPGaAs) OPO*. in *Conference on Lasers and Electro-Optics/Quantum Electronics and Laser Science and Photonic Applications Systems Technologies*. 2005. Baltimore, Maryland: Optical Society of America.
6. Vodopyanov, K.L., et al., *Optical Parametric Oscillation in Quasi-phase-matched GaAs.* Optics Letters, 2004. **29**(16): p. 1912-1914.
7. Schunemann, P.G., et al. *Recent Advances in All-Epitaxial Growth and Properties of Orientation-Patterned Gallium Arsenide (OP-GaAs)*. in *Conference on Lasers and Electro-Optics/International Quantum Electronics Conference*. 2009. Baltimore, Maryland: Optical Society of America.
8. Stothard, D.J.M., C.F. Rae, and M.H. Dunn, *An Intracavity Optical Parametric Oscillator With Very High Repetition Rate and Broad Tunability Based Upon Room Temperature Periodically Poled MgO:LiNbO$_3$ With Fanned Grating Design.* IEEE Journal of Quantum Electronics, 2009. **45**(3): p. 256-263.
9. D.J.M., S., *Personal Communication*, D. Kane, Editor. 2016.
10. Stothard, D.J.M. and M.H. Dunn, *Relaxation Oscillation Suppression in Continuous-wave Intracavity Optical Parametric Oscillators.* Optics Express, 2010. **18**(2): p. 1336-1348.
11. Schunemann, P.G., et al. *CW mid-IR OPO Based on OP-GaAs*. in *Lasers and Electro-Optics Europe (CLEO EUROPE/IQEC), 2013 Conference on and International Quantum Electronics Conference*. 2013.
12. Guha, S., et al. *Tunable Continuous-wave Midwave Infrared Generation using an Orientation Patterned GaAs Crystal with a Fan-out Grating Design*. 2015.
13. Vodopyanov, K.L., I. Makasyuk, and P.G. Schunemann, *Grating Tunable 4 - 14 μm GaAs Optical Parametric Oscillator Pumped at 3 μm.* Optics Express, 2014. **22**(4): p. 4131-4136.
14. Ru, Q., et al. *Femtosecond OPO Based on Orientation-Patterned Gallium Phosphide (OP-GaP)*. in *Conference on Lasers and Electro-Optics*. 2016. San Jose, California: Optical Society of America.
15. Smolski, V.O., et al. *Octave-wide Frequency Comb Centered at 4 μm Based on a Subharmonic OPO with Hz-level Relative Comb Linewidth*. 2016.
16. Figen, Z.G. *Aperiodic Grating Design Methods Employed for Idler-efficiency Enhanced Beam Generation in Orientation-Patterned GaAs*. 2016.
17. Gürkan Figen, Z., O. Aytür, and O. Arıkan, *Idler-efficiency-enhanced Long-wave Infrared Beam Generation using Aperiodic Orientation-patterned GaAs Gratings.* Applied Optics, 2016. **55**(9): p. 2404-2412.
18. Clément, Q., et al., *Longwave Infrared, Single-frequency, Tunable, Pulsed Optical Parametric Oscillator Based on Orientation-patterned GaAs for Gas Sensing.* Optics Letters, 2015. **40**(12): p. 2676-2679.
19. Clément, Q., et al. *Pulsed, Tunable, Single-frequency OP-GaAs OPO for the Standoff Detection of Hazardous Chemicals in the Longwave Infrared*. 2015.

Appendix A
Table of OP-GaAs Crystals Implemented in This Work and Their Properties

Crystal	25B	25D	26K	25E	60E1	60F1
Grating Period (μm)	60.5	60.5	56	60.5	60.5	60.5
hxbxl (mm)	1.4 x 6 x 16.4	1.2 x 8 x 25.7	1 x 4 x 21	1.2 x 5 x 25.7	1.2 x 5 x 26	1.2 x 5 x 26
Width of grating (μm)	600±50	600±50	600±50	600±50	600±50	600±50
Single pass loss (%)	<1%	20%	<1%	8.5	8.7	7.4
Wedge angle on crystal facet (degrees)	0	Unknown	Unknown, considered negligible	0.4 between the long edges	1 between the long edges	1.3 between the short edges
Scattering losses	Low	Unknown	Unknown, assumed low	High	Low	Low
Additional Notes	#Split into 3 pieces after polishing, none of which were suitable for implementation	#Due to high single pass losses, further investigations with this crystal were deemed unprofitable	Crystal was returned to supplier at their request			

Appendix B
List of Author's Conference Proceedings

Kane, D. J., Hopkins, J., Dunn, M. H., Schunemann, P., G., and Stothard, D.J.M., "Tm:YAP Pumped Intracavity Pulsed OPO Based on Orientation-Patterned Gallium Arsenide (OP-GaAs)," in Advanced Solid State Lasers, OSA Technical Digest (online) (Optical Society of America, 2015), paper ATh2A.20.

Stothard, D.J.M., Kane, D. J., Schunemann, P.G., Dunn, M.H., "Intracavity OPOs based upon OPGaAs: towards a flexible deep-infrared active hyperspectral imaging system," in SPIE Defense and Security Baltimore 2015 (Invited talk), Baltimore

Kane, D. J., Hopkins, J. M., Dunn, M. H., Schunemann, P.G., Stothard, D. J. M., "Tm:YAP Pumped Intracavity Pulsed OPO Based on Orientation-Patterned Gallium Arsenide (OP-GaAs)" in 6th EPS Europhoton Conference, 2014, Neuchatel

Stothard, D.J.M, Kane, D. J., Hopkins, J. M., Schunemann, P.G., Dunn, M.H., "Intracavity Optical Parametric Oscillators Based upon OPGaAs," in NATO SET 210 meeting on Lasers and Photonics in defence 2014, Salisbury

Stothard, D.J.M, Kane, D. J., Dunn, M.H., "Intracavity Optical Parametric Oscillators Based upon OPGaAs," in SPIE Photonics West 2014 (Invited talk), SPIE, San Francisco

McKnight, L.J., Bennett, T.E., Kane, D.J., Hamilton, C.J., Malcolm, G.P.A., Stothard, D.J.M., Hopkins, J.M., Dawson, M.D. , "Current Challenges for High-Power Semiconductor Disk Lasers," in Proceedings Of The 2013 High Power Diode Lasers And Systems Conference, IEEE, Coventry